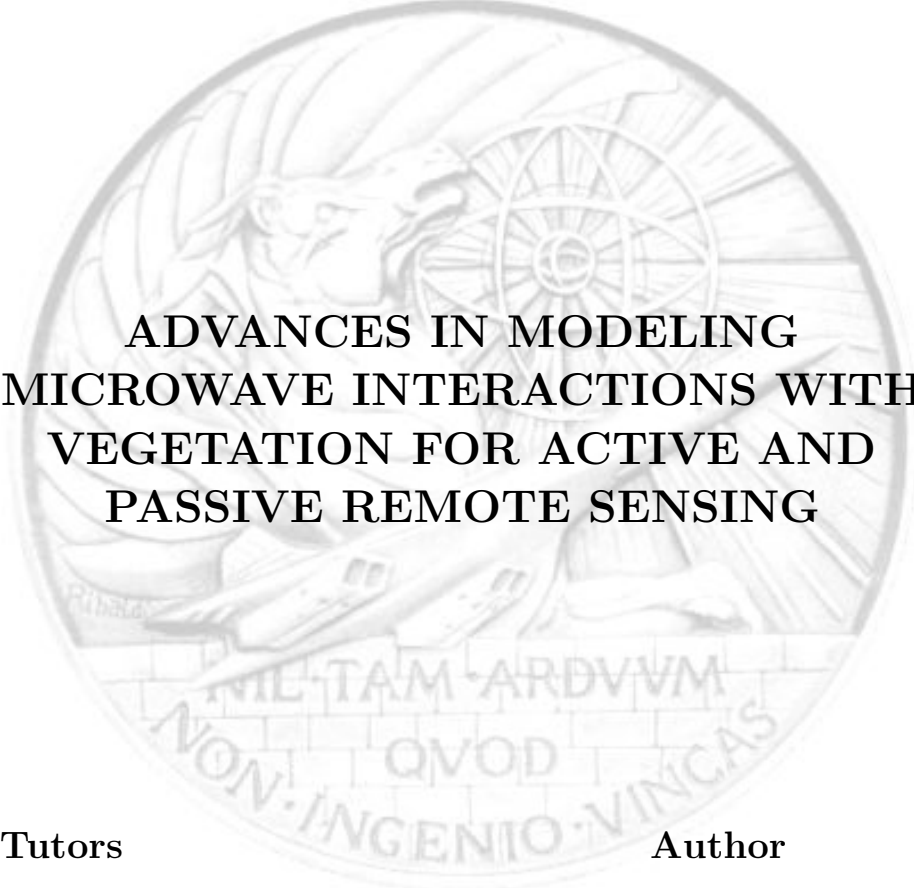


TOR VERGATA UNIVERSITY

Computer Science Department

GeoInformation PhD Thesis

The seal of Tor Vergata University is a circular emblem. It features a central figure, likely a scholar or saint, with a halo, holding a book. The figure is surrounded by a sunburst or starburst pattern. Below the figure, there is a banner with the Latin motto "NIL TAM ARDVUM NON INGENIO VINCAS".

ADVANCES IN MODELING MICROWAVE INTERACTIONS WITH VEGETATION FOR ACTIVE AND PASSIVE REMOTE SENSING

Tutors

Prof. Paolo Ferrazzoli

Prof. Leila Guerriero

Author

Andrea Della Vecchia

December 2006

*To my wife Elisabetta and my family
for their support and encouragement*

Acknowledgements

A special thanks are due to Paolo Ferrazzoli and Leila Guerriero for the availability and support always provided during the whole course of this PhD work, and to the colleagues of GeoInformation laboratory of Tor Vergata University. I also wish to thank all the people I met in these last three years. Jean-Pierre Wigneron, who kindly hosted me in EPHYSE laboratory in INRA (Bordeaux-France), Kauzar Saleh Contell and Jennifer Grant. I would also like to thank Massimo Guglielmetti and Mike Schwank. Tomas Jackson for his availability during the period I have been in HYDROLOGY laboratory in USDA (Beltsville-USA), Rajat Bindlish for his fundamental logist support and all the people I had the pleasure to met there.

Contents

Abstract	1
1 Introduction	3
1.1 Introduction	3
1.2 Microwave Modeling General Aspects	4
1.3 Model Review for Vegetation Covered Soils	6
1.3.1 Semiempirical Models	6
1.3.2 Continuous Layer Models	7
1.3.3 Discrete Models	7
1.4 Thesis Objectives and Outline	10
2 The Tor Vergata Model	13
2.1 Introduction	13
2.2 Model Description	15
2.2.1 Single Scatterer Characterization	15
2.2.2 Sublayer Characterization	16
2.2.3 Matrix Doubling Algorithm	19
2.3 Backscattering Coefficient Computation	20
2.4 Emissivity Computation	20
2.5 Conclusions	21
3 Single Scatterer Model Improvement	23
3.1 Basic Definitions	23
3.2 Curved Sheet Approximation	28
3.2.1 Theory	29
3.2.2 Results	32
3.3 Hollow Stem Approximation	37
3.3.1 Theory	38
3.3.2 Results	40

3.4	Conclusions	48
4	Application to Agricultural Fields	49
4.1	Experimental data set	49
4.1.1	Central Plain Data Set	51
4.1.2	Matera Data Set	53
4.1.3	Loamy Data Set	57
4.2	Simulations and comparisons	60
4.2.1	Corn fields	60
4.2.2	Wheat fields	60
4.2.3	Accuracy Assessment and Conclusions	68
5	Forests	69
5.1	Introduction	69
5.2	Specific Aspects for Forest Radiometry Modeling	70
5.3	Litter representation	72
5.4	Forest Structure Algorithm	75
5.4.1	Single tree description	77
5.4.2	Using ECOCLIMAP LAI information	79
5.4.3	Geometrical and moisture variables	82
5.5	Parametric Analysis	86
5.5.1	Softwood	87
5.5.2	Hardwood	91
6	Forests Model Validation	99
6.1	EuroSTARRS	99
6.2	Bray	103
6.3	Jülich	106
6.4	STAAARTE	111
	Bibliography	122
	Curriculum Vitae	123
	List of Publications	125
	List of Tables	131
	List of Figures	136

Abstract

In the last decades, in parallel with the collection of experimental radar data, several efforts have been made to develop and refine microwave scattering models of crops. Two main motivations have stimulated these efforts. The first motivation is scientific: the availability of a large amount of experimental radar data, collected over several kinds of fields, has represented a unique opportunity to advance the understanding of the interaction processes between microwaves and natural media, in particular soil and vegetation. A second motivation is related to applications. It has been recognized that σ^o is sensitive to some key variables useful for applications (e.g. soil moisture and vegetation biomass) but this sensitivity is heavily affected by the influence of several other variables. All these dependencies must be understood in order to develop reliable algorithms. Moreover, in a natural environment, soil and vegetation variables evolve simultaneously and follow rules which cannot be modified by the experimenter. Therefore, models are a unique way to single out the sensitivity of σ^o to variations of specific parameters.

In the first part of the thesis recent advances for single scatterer modeling are proposed. In particular long leaves are represented as dielectric curved sheets and mature wheat's stems are represented as hollow dielectric cylinders. For both kinds of scatterers, suitable models have been developed and implemented. Both the theoretical approximations are tested and validated by means of scatterometer, airborne and satellite data collected over several corn and wheat sites, where also detailed ground truth are available.

In the second part of the thesis efforts have been done in order to improve the electromagnetic modeling of forest emissivity. Important space projects, such as SMOS, are under development, with the purpose of monitoring soil moisture and land properties by means of spaceborne L band radiometers. It is planned to use the model for exploiting the potential of spaceborne L band radiometers to monitor the moisture of forest covered soils. To this aim, it is necessary to consider that the resolution is of the order of some kilometres. Within this scale, there is a wide variability of tree ages

and dimensions. Moreover, available a-priori information may cover only forest category and some general variables, such as Leaf Area Index (LAI). Therefore, a procedure must be developed to estimate the detailed input data set required by the model starting from general variables and using suitable allometric equations. The objective of this paper is twofold. First of all, it describes recent refinements applied to the model in order to consider also litter effects and generate the input data set as a function of LAI for given forest species. To this aim, suitable routines have been introduced. Moreover, the results of a new test are presented. Model outputs have been compared against experimental brightness temperatures collected by L-band radiometers over coniferous and deciduous forests.

Chapter 1

Introduction

This chapter introduces the role of microwave modeling in remote sensing applications. In particular, the case of vegetated soils will be considered. The reader will find a short overview of the electromagnetic model theories available in the literature, and some their main applications. An outline and a summary of the PhD study will conclude the chapter.

1.1 Introduction

The microwave portion of the spectrum is particularly important in remote sensing applications. The capability to penetrate the atmosphere with a very low interaction in almost all weather conditions, and the possibility to operate independently from the sun illumination, make it a very useful frequency band in such a field of applications.

In the last years, many efforts have been focused to improve the performances of microwave instruments and significant results have been obtained for both active and passive sensors. Simultaneously, an increasing number of applications have found, in the microwave band, the best trade-off in terms of spatial and temporal resolution. Agricultural, forestry and hydrology are just some of the applications, for which theoretical studies gave an important contribution.

However, further work is needed in order to implement fully operational algorithms. To this aim, the importance of developing realistic and reliable models is well recognized. In many cases, simulated values are compared against experimental data and some results show a fairly good agreement. Anyway, available experimental signatures are still sparse, comparisons are often limited to single data sets, and ground data are not as complete as

the electromagnetic models would require. Further experiments are planned using new spaceborne SAR's (such as ENVISAT, RADARSAT-2, etc.) and new advanced radiometers (such as SMOS); in the meantime, efforts aimed at making the models more realistic are in progress. Two main motivations have stimulated these efforts: the first one is the availability of a large amount of experimental data, collected over several kinds of areas. They represent a unique opportunity to advance the understanding of the interaction processes between microwaves and natural media, in particular soil and vegetation. A second motivation is related to the applications. It has been recognized that backscattering coefficient and emissivity are sensitive to some key variables, useful for applications (e.g. soil moisture and vegetation biomass), but this sensitivity is heavily affected by the influence of several other parameters. All these dependencies must be understood in order to develop reliable algorithms. Moreover, in a natural environment, soil and vegetation variables evolve simultaneously, and follow rules which cannot be modified by the experimenter. Therefore, models are an unique way to single out the sensitivity of microwave signal to variations of specific parameters.

1.2 Microwave Modeling General Aspects

A model may be defined as a relationship linking the radar output or the emissivity to the observation parameters (i.e., frequency, look angle, polarization) and to N surface variables. The backscattering coefficient

$$\sigma^o = F(f, \theta, \psi_r, \chi_r, \psi_t, \chi_t, a_1, a_2, \dots, a_N) \quad (1.1)$$

and the emissivity

$$e = G(f, \theta, \psi_r, \chi_r, a_1, a_2, \dots, a_N) \quad (1.2)$$

are defined in several texts [Ulaby et al. \(1986\)](#), f is the radar frequency, θ is the observation angle, ψ_r and χ_r are the rotation and ellipticity angle of the received electromagnetic field, ψ_t and χ_t , which are present only for the backscattering coefficient, are the rotation and ellipticity angle of the transmitted field [Ulaby and Elachi \(1990\)](#). The N variables (a_1 , a_2 and a_N) represent soil and vegetation properties. Variables influencing microwave measurements may be classified according to the scheme indicated below. Most of them may be used as inputs for models:

- Bare soils

- Variable related to dielectric properties: permittivity $\epsilon_s = \epsilon_s' + j\epsilon_s''$, depending on soil moisture content (SMC), soil texture, bulk density, temperature and salinity.
- Variables related to surface roughness: in a single-scale description, surface roughness is characterized by its autocorrelation function (ACF) and by two variables, such as height standard deviation and correlation length. A multi-scale roughness description requires a different set of variables.
- Vegetation covered soils
 - The same soil variables defined above
 - Variables related to the amount of vegetation matter per unit area. The most commonly used are fresh biomass, plant water content (PWC) and plant density. For a correct description of electromagnetic effects, it is important to single out the fraction of vegetation components, such as stems, ears, leaves, pods, petioles for agricultural fields or trunks and branches for forests. For leaves, also the leaf area index (LAI) is often adopted.
 - Variable related to permittivity of vegetation elements: $\epsilon_v = \epsilon_v' + j\epsilon_v''$, related to gravimetric moisture, dry matter density, temperature and salinity.
 - Variables related to vegetation geometry: height and diameter for stems and trunks, length, width and thickness for leaves, and corresponding distributions of orientations are required. For some crops, also twigs and/or petioles may have a significant influence and some models may require also local position of elements and leaf curvature parameters.

The aim of applicative algorithms is to retrieve key parameters such as soil moisture, for hydrology applications, or vegetation biomass, for agricultural applications. These algorithms are composed by a first step, called direct modeling and a following step of retrieval (or inverse modeling). It is clear that an advanced knowledge about the interaction of the electromagnetic waves with the observed land is required, in order to proceed to the retrieval with the least uncertainty. On the other hand, aspects such as the speed and inversion complexity of the electromagnetic direct model, are key parameters for an application algorithm. Also for this reason, different kinds of models have been developed during the last decades. An overview about the state of the art of direct modeling is presented in the next section. The case

of vegetation covered soils, which are the subject of this Thesis, will be considered.

1.3 Model Review for Vegetation Covered Soils

Many theoretical models have been developed in the last years, in order to describe the scattering and emissivity effects over vegetated soils. Due to the complexity of the interactions, an exact solution of the problem is not possible, and several approximations have been assumed to solve it. A list of main active and passive model approximations is here proposed.

1.3.1 Semiempirical Models

A semiempirical model, called “Water cloud”, was proposed by [Attema and Ulaby \(1978\)](#). It was aimed at reproducing the soil and vegetation scattering, by a simplified parametric function. By fitting the collected measured data, it is possible to assess the four function coefficients. More complete the data set is, more reliable is the coefficient fitting. Multi-frequency, multi-angle and multi-polarization radar data have been used in the original work. In the last years several improvements of this model have been proposed. Particular attention has been directed toward the empirical relationship between σ^o and vegetation parameters like PWC and LAI. A relationship with SMC was proposed by [Prévoit et al. \(1993\)](#), over wheat fields at C- and X-band, VV and HH polarizations, for an angle range of 15° – 45° . A more advanced version of “Water cloud” model was proposed by [De Roo et al. \(2001\)](#). The main improvement was the introduction of the crosspolarized backscatter coefficient. Furthermore, the relationships between the backscattering coefficients and soil moisture, PWC and crop height, were analyzed.

A semiempirical model used to estimate the emissivity was proposed by [Kirdyashev et al. \(1979\)](#); [Mo et al. \(1982\)](#). It is a zero order solution of the radiative transfer theory. The physical approximation is characterized by the knowledge of the albedo and optical depth, and empirical coefficients are needed to correlate these two parameters with the properties of the vegetation and radiometric configurations, [Jackson et al. \(1982\)](#); [Wigneron et al. \(1995\)](#).

Because of their simplicity, the semiempirical models present some advantage in terms of reduced number of input parameters, computation time and implementation difficulty. On the other hand, the general validity of related fitting coefficients is questionable. Because the model simply depends on PWC or vegetation biomass, it is not able to consider effects of density

and geometrical properties. For example, a dense field at early stage may have the same biomass or PWC of a sparser field in a developed stage, but the backscattering (or emissivity) values may be completely different. A possible way to solve this limit and keep the analytic simplicity, is using a physical model to get the fitted coefficients needed by the semiempirical one, as proposed by [Wigneron et al. \(1999\)](#); [Ferrazzoli et al. \(2002\)](#).

1.3.2 Continuous Layer Models

A theoretical approach was proposed by [Fung and Ulaby \(1978\)](#); [Fung \(1979\)](#); [Tsang and Kong \(1981\)](#) reusing the random media theory [Tatarskii \(1964\)](#); [Stogryn \(1974\)](#). Both vegetation and soil are represented like two dielectric slabs. The permittivity of the first one is composed by an average and a fluctuant component, which is a random function of coordinates. The fluctuating part of the permittivity is correlated with the dielectric inhomogeneity, in particular due to leaves. Instead, the soil permittivity values are just characterized by a constant complex value. Mainly, the limits of this approach are two. The first one is a missing direct relationship between the fluctuation of the permittivity and the real properties of the dielectric bodies. The second limit is the representation of the boundaries between air-vegetation and vegetation-soil, by completely flat interfaces.

1.3.3 Discrete Models

A more sophisticated theory allows to take into account the quasi-real geometry of the vegetation components. This kind of approach is named “discrete approach”. Vegetation elements are described by means of dielectric bodies, whose simplified shapes permit a more suitable electromagnetic characterization.

This theory permits to highlight the scattering and emissivity properties of each vegetation component. Differently from the models quoted in sections §1.3.1 and §1.3.2, it permits to investigate the electromagnetic interactions among all the vegetation components. This is possible because the input structural variables are measured directly from the fields. In available discrete models, four main steps may be identified.

Geometrical description

The first step is a subdivision of the canopy into elementary components, and related selection of suitable geometrical shapes. The soil is represented as a dielectric half-space with rough interface. Each vegetation component

(stems, leaves, petioles, trunks and branches) is represented by using a simplified geometry. Cylinder structures may represent stems, trunks and branches. Discs, elliptical or curved sheets may represent leaves.

Permittivity modeling

For both soil and vegetation, the permittivity must be computed. Several works have been carried out for the soil. Most of them are based on the semiempirical formula of [Dobson et al. \(1985\)](#), later refined by [Ulaby et al. \(1986\)](#), or the empirical formulation derived by [Hallikainen et al. \(1985\)](#). This empirical or semiempirical formulation depends mainly on soil moisture content and soil texture. The main limit is the hypothesis of a homogeneous soil situation, which in many fields is not completely verified, because of a stratified soil moisture content.

Empirical approaches were followed by [Ulaby and El-Rayes \(1987\)](#); [Mätzler \(1994\)](#), to develop a polynomial function for the vegetation permittivity. Both works are based on empirical data: for the first one corn leaves and stems have been considered, whereas for the development of the second model different kinds of leaves have been used. A study about the anisotropy of the permittivity function, for two kinds of coniferous trees, has been proposed by [Franchois et al. \(1998\)](#). The results show an appreciable variation for both the real and imaginary components of the permittivity, as a function of the radial distance.

Electromagnetic single scatterer characterization

Soil scattering, as well as scattering and extinction of vegetation elements must be estimated. For soil characterization it is possible to compute the scattering in the upward direction, by using two asymptotic approximations, Small Perturbation and Geometrical Optics [Ulaby et al. \(1986\)](#), respectively for low and high frequencies. A more advanced electromagnetic model, the Integral Equation Model (IEM), was made available by [Fung \(1994\)](#) and an improvement was presented by [Alvarez-Perez \(2001\)](#).

The vegetation is represented by simplified dielectric bodies, whose electromagnetic properties depend on the ratio between wavelength and physical variables. Typical approximations adopted for stems, petioles, trunks, branches and any bodies, whose geometry is reducible to a cylindrical structure, are proposed by [Karam et al. \(1988\)](#); [Stiles and Sarabandi \(2000\)](#); [Della Vecchia et al. \(2006c\)](#). Instead, leaves are usually characterized discs and elliptical dielectric bodies [Eom and Fung \(1984\)](#), or by means of flat or

curved dielectric sheets [Sarabandi et al. \(1988\)](#); [Della Vecchia et al. \(2004\)](#).

Backscattering and emissivity computation

The computation of the overall backscattering coefficient and of emissivity value, are the conclusive tasks of the modeling procedure. Further aspects that may differentiate the models are the order of scattering interactions among the scatterers and the electromagnetic wave approach adopted, incoherent (Radiative Transfer Theory) or coherent (partial or full wave approach).

A well known discrete model is the MIMICS [Ulaby et al. \(1990\)](#), initially developed for forest applications. It is based on the first order solution of the Radiative Transfer Theory (RTT). It computes attenuation, backscattering and specular scattering coefficients. In order to extend the model to agricultural fields (wheat and canola), a modified version was proposed by [Touré et al. \(1994\)](#). A similar work was issued by [Macelloni et al. \(2001b\)](#) with the purpose to investigate the backscattering behaviour of narrow leaf crops (wheat) and broad leaf crops (sunflower).

A main limit of this first order approach is the underestimation of the cross-polarized backscattering coefficient, and the co-polarized ones at the higher frequencies. An improvement of the single scattering model, is the solution of the RTT equations proposed by [Karam et al. \(1992\)](#). They extended the scattering order, among the independent scatterers, up to the second order. A similar approach was used by [Cookmartin et al. \(2000\)](#), to compare simulated data with experimental signatures, collected over rape, barley and wheat fields. [Eom and Fung \(1984\)](#) proposed a more advanced approach, for agricultural applications. It was based on [Twomey et al. \(1966\)](#) theory, who found out a valid solution of RTT equations (Matrix Doubling Algorithm), in order to consider the multiple scattering of all orders, for atmospheric applications. Further models are based on the Matrix Doubling Algorithm, for agricultural applications [Bracaglia et al. \(1995\)](#) and forest ones [Ferrazzoli and Guerriero \(1995\)](#).

A more sophisticated coherent theory was proposed in the last years. Differently from RTT, information about wave phase is computed, and electromagnetic field is considered, in place of electromagnetic power. The approach may be partially coherent or fully coherent. In the first case a coherent approach is used to combine the scattering contributions of vegetation elements [Stiles and Sarabandi \(2000\)](#); [Chiu and Sarabandi \(2000\)](#); [Marliani et al. \(2002\)](#), but the attenuation is computed by using the well known incoherent Foldy's theory [Tsang et al. \(1985\)](#). The fully coherent ap-

proximation proposed by [Tsang et al. \(1995\)](#), considers the vegetation like an ensemble of clusters, composed by elementary dielectric scatterers, whose interaction is completely considered in terms of electromagnetic wave propagation. Recently another fully coherent approach has been proposed by [Oh et al. \(2002\)](#). Because of the great complexity and the relative youth of the theory, further investigation and theoretical studies are required to use this approach in operative algorithms. Main limits of a partially coherent approach is the lower order of scattering interaction, whereas the main limit of the a fully coherent approximation is the simplicity of the geometrical representation of the vegetation. A further limit is the difficulty to get a such detailed information from ground measurements, particularly critical is the knowledge about the absolute position of all scatterers which compose the monitored field.

The RTT is conventionally used to develop emissivity models too. The most common approach used to estimate the emissivity is based on the knowledge of the total scattered power. In this way, by means of the energy conservation law, the emissivity is computed as the complement to one of the reflectivity. An example is proposed in [Ferrazzoli and Guerriero \(1996\)](#), where the overall scattering is computed by means of the matrix doubling algorithm, in order to take into account multiple scattering. Another theory adopted to assess the emissivity, based on the RTT, is proposed by [Karam \(1997\)](#). It is based on a first order solution of the radiative transfer equation. The model can consider temperature gradient inside the canopy and computes directly the emissivity without estimating the overall bistatic scattering coefficient.

1.4 Thesis Objectives and Outline

General aims

The Thesis illustrates the following main points:

- Refining of single scatterer modeling, in order to extend and improve the reliability of the Tor Vergata model. In particular, an alternative electromagnetic representation will be proposed in order to reproduce the curved leaves of agricultural fields such as corn and wheat. A single scatter model will be proposed in order to represent the wheat stem's hollowness.
- An exhaustive verification and validation phase will be proposed by means radar signatures collected within ESA-ESTEC project under

contract n.17011/03/NL/JA.

- A new theoretical approach will be proposed in order to reproduce the understory-litter sublayer component. Furthermore, in the framework of ESA-ESTEC project under contract n.18823/04/NL/FF, in view of SMOS mission, a growth algorithm has been developed in order to adopt model at large scale applications.
- Finally the model will be verified and validated by means ground and airborne campaign.

Outline

Chapter 2 introduces and discusses the basic properties of Tor Vergata electromagnetic model

Chapter 3 describes the the single scatterer modeling improvements, introduced into the model

Chapter 4 shows the model validations through several experimental campaigns for agricultural applications

Chapter 5 proposes a new geometric description algorithm, in order to consider several species of forests. Also a new model including litter effects is proposed. The forest model is validated mainly by two detailed ground based radiometric experiments and two airborne experiments.

Chapter 6 concludes the work, with some discussions about the previous chapter

Chapters 3, 4, 5 and 6 are based on published and/or submitted papers.

Chapter 2

The Tor Vergata Model

The previous chapter has introduced an overview of the electromagnetic modeling approaches used to simulate the backscattering and emissivity of vegetated soils. The present Chapter aims at introducing the electromagnetic model developed at Tor Vergata University, which basic theory has been introduced into §1.3.3. The reader will find the description of the theoretical approach used to model vegetation signatures collected by active and passive systems.

2.1 Introduction

The model developed at the University of Rome “Tor Vergata” uses the radiative transfer theory to describe the interaction between the incoming electromagnetic wave and the vegetation [Bracaglia et al. \(1995\)](#). It can compute both the backscattering coefficient [Ferrazzoli and Guerriero \(1995\)](#) and the emissivity [Ferrazzoli and Guerriero \(1996\)](#) by using the energy conservation law. To represent the vegetation architecture a discrete approach is adopted, and dielectric bodies with suitable shapes are used to describe the geometric properties. Figure 2.1(a)–(b) depict both the scheme adopted to represent a generic agricultural field and a generic forestry one.

Different assumptions about dimensions, orientations and dielectric properties of the scatterers can be done to distinguish different kinds of canopies. The model is currently used to compute backscattering and emissivity for agricultural fields [Della Vecchia et al. \(2006b\)](#) and forests [Della Vecchia et al. \(2006d\)](#). Once a geometric representation is chosen, the bistatic scattering and extinction coefficients for each scatterer are computed. Finally, all contributions are combined by means the “Matrix Doubling Algorithm”. It

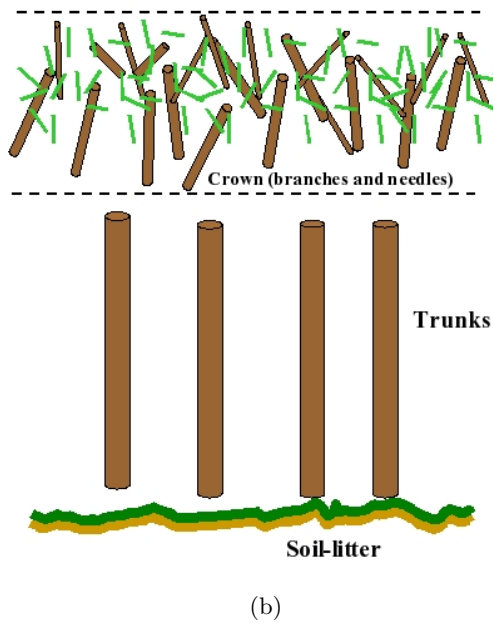
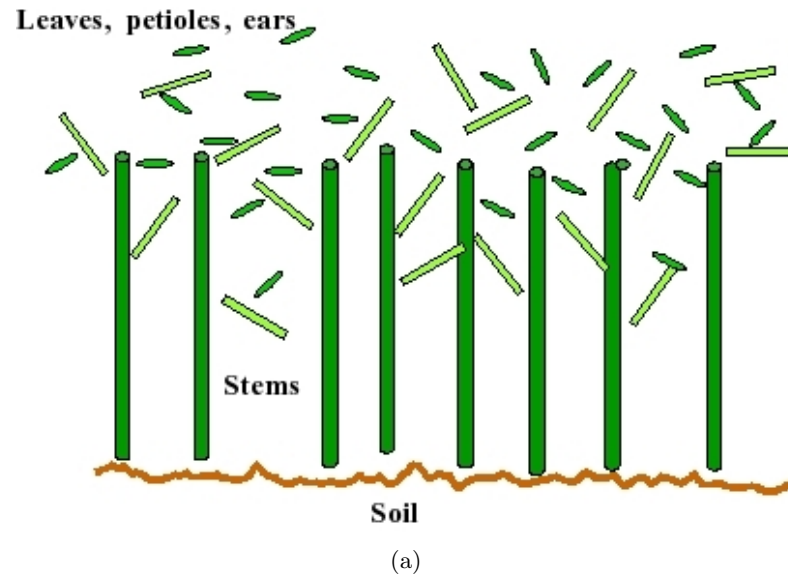


Figure 2.1: Example of geometric structure adopted for a generic vegetated soil. (a) Agricultural sketch; (b) Forest sketch.

allows us to estimate the multiple interactions among the different dielectric bodies which compose the vegetation. The matrix doubling is used again when the whole vegetation and the soil interactions have to be combined. The last step consists is the assessment of the overall backscattering coefficient, for the active version of the model, or the emissivity for the passive one.

2.2 Model Description

This section provides further details about the model, in order to get a complete and exhaustive description of the theoretical formulation.

2.2.1 Single Scatterer Characterization

Similarly to other discrete models, the first step required by Tor Vergata Model (TVM) is a detailed analysis of the geometric properties of the vegetation. After its decomposition into elementary components (leaves, petioles, stems for agricultural fields, or trunks, branches and leaves for forests) a detailed knowledge of the following variables is required:

- Geometric variables such as shape, dimension and orientation of stems, leaves, ears, branches and trunks
- Permittivity values, which are related to moisture and dry matter density for vegetation, moisture and texture for soil
- Number of elements per unit area and moisture content
- Soil variables as moisture, surface height standard deviation and correlation length

First of all, the single elements are characterized. Because of the complex geometry, it is necessary to assume some simplifications. The collection of suitable shapes adopted for the dielectric scatterers is a critical step and research is currently in progress. Furthermore, the choice of a reliable electromagnetic approximation is strictly correlated to the ratio between wavelength and scatterer dimensions. Mostly used single scatterer approximations are here reported

- Leaves are represented as discs and ellipses. It is possible to use the Rayleigh-Gans [Eom and Fung \(1984\)](#) approximation, when at least one dimension of the scatterer is negligible with respect to the wavelength.

For higher ratios between physical dimensions and wavelength, the physical optics approximation [Le Vine et al. \(1983\)](#) is more reliable. Also the resistive approximation may be used. In [Senior et al. \(1987\)](#), rectangular and square plates are analyzed, whereas curved dielectric plates are introduced in [Sarabandi et al. \(1988\)](#).

- Cylinders may represent the stems, petioles, ears, trunks, branches and needles. The Rayleigh-Gans approximation can be used with the same previous assumptions, and the infinite length approximation [Seker and Schneider \(1988\)](#) can be adopted when the length of the cylinder is much higher than the wavelength.
- The soil is represented through a dielectric rough half-space, and the integral equation model may be used to compute the bistatic scattering coefficient using the formulation of [Fung \(1994\)](#). For particularly smooth soils with respect to the wavelength, the small perturbation approximation is used, while the geometrical optics approximation is adopted for very rough surfaces.

2.2.2 Sublayer Characterization

To combine the interactions among the different dielectric scatterers which compose the vegetation, the numerical algorithm “Matrix Doubling” is used. This approach allows to take into account the multiple scattering effects inside a volume filled with dielectric bodies. The idea is to divide the canopy layer into several sub-layers and then compute the multiple reflections among them. To characterize the scattering in the upper and lower half-space associated to the generic sublayer, as depicted in [Figure 2.2](#), the electromagnetic behaviour of the dielectric bodies, which compose the sublayer, must first be characterized. To this aim, the scattering cross section matrix

$$\boldsymbol{\sigma} = 4\pi \begin{bmatrix} \langle |f_{vv}|^2 \rangle & \langle |f_{hv}|^2 \rangle \\ \langle |f_{vh}|^2 \rangle & \langle |f_{hh}|^2 \rangle \end{bmatrix} \quad (2.1)$$

and the extinction cross section matrix are computed

$$\boldsymbol{\sigma}_e = \frac{4\pi}{k} \begin{bmatrix} \langle \Im\{f_{vv}^F\} \rangle & 0 \\ 0 & \langle \Im\{f_{hh}^F\} \rangle \end{bmatrix} \quad (2.2)$$

k (m^{-1}) is the electromagnetic wave number, f_{vv} , f_{hv} , f_{vh} , f_{hh} are the scattering amplitude functions, averaged by considering the possible geometrical orientations of the single scatterer, described by the Eulerian angles α , γ and

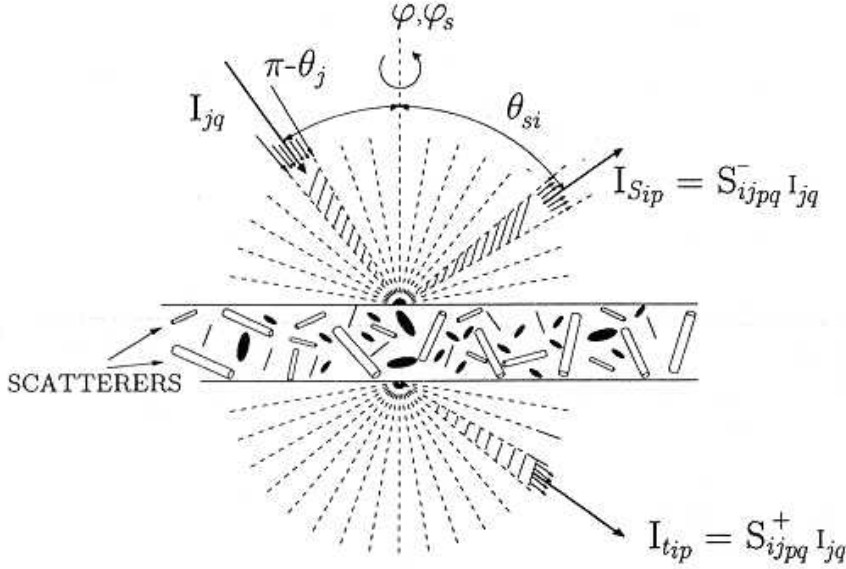


Figure 2.2: Scatter mechanism in the matrix doubling algorithm

β . The forward scattering theorem is adopted to compute the extinction cross section, and the amplitude scattering function in the forward direction is used.

The scattering functions are continuous functions of the incident and scattering angles, but due to the enhanced computational complexity, it is not possible to keep this property. A reasonable discretization of the space is mandatory in order to get an acceptable computing time. The discretization of the functions is obtained in the elevation plane, by subdividing the $\pi/2$ elevation range into N_θ intervals of width $\Delta\theta$, and the 2π azimuth range into N_ϕ intervals of width $\Delta\phi$. In this way the incoming and scattered fields are belonging respectively to the j^{th} and i^{th} elevation interval ($1 \leq (i, j) \leq N_\theta$), with azimuth angle $\phi_s - \phi$, where it represents the difference between scattering and incident azimuth angles, with $(0 \leq (\phi_s - \phi) \leq 2\pi)$.

Once the electromagnetic behaviour of all the elements, composing the sublayer, is known, it is possible to proceed to the second step, the sublayer electromagnetic characterization. To describe the scattering properties the S^- and S^+ matrices are adopted. The first one represents the upward scattering specific intensity $I_{ip}(\phi_s - \phi)$ ($\text{W}/\text{m}^2 \text{sr}$), in the i^{th} elevation angular

interval and ϕ_s azimuthal angle, at p ($p = v, h$) polarization, due to an incident power, uniformly distributed within a cone of width $\Delta\theta \sin\theta \, d\phi$ of intensity $I_{jq}(\phi)$ ($\text{W}/\text{m}^2 \text{ st}$), coming from the angular interval j^{th} with polarization q ($q = v, h$).

$$S_{ijpqm}^- = \frac{n\Delta z \Delta\theta \sin\theta_j}{4\pi \cos\theta_{si}} \cdot a_m \mathcal{F}_m \left\{ \sigma_{ijpq}^-(\phi_s - \phi) \right\} \quad (2.3)$$

$$S_{ijpqm}^+ = \frac{n\Delta z \Delta\theta \sin\theta_j}{4\pi(-\cos\theta_{si})} \cdot a_m \mathcal{F}_m \left\{ \sigma_{ijpq}^+(\phi_s - \phi) \right\} \quad (2.4)$$

A further hypothesis of independency, among the scatterers belonging to the same volume of thickness Δz , make of the elements of Stokes matrix directly proportional to the scatterers density n (m^{-3}). The $\mathcal{F}_m\{ \}$ indicates the m^{th} term of Fourier series, adopted to express the dependence on $\phi_s - \phi$, and a_m represents the Fourier coefficient, which is equal to 2π for the zero-th order term and π for the higher ones. By means of a readjustment of the previous matrices, a further form is proposed for both of them in equation (2.5).

$$\mathbf{S}_m^\pm = \begin{bmatrix} \mathbf{S}_{vvm}^\pm & \mathbf{S}_{vhm}^\pm \\ \mathbf{S}_{hvm}^\pm & \mathbf{S}_{hhm}^\pm \end{bmatrix} \quad (2.5)$$

where \mathbf{S}_{pqm}^\pm , whose dimension is $2N_\theta \times 2N_\theta$, contain the S_{ij}^\pm coefficients. In order to consider the overall electromagnetic interaction, it is needed to estimate the electromagnetic field which propagates through the vegetation. Thus, the transmission matrix is represented in equation (2.6).

$$\mathbf{T}^+ = \mathbf{1} - \begin{bmatrix} \mathbf{k}_{evv} & 0 \\ 0 & \mathbf{k}_{ehh} \end{bmatrix} \quad (2.6)$$

The elements of the transmission matrix, of dimension $2N_\theta \times 2N_\theta$, are obtained directly from the extinction matrix, equation (2.2), and they are expressed as

$$\mathbf{k}_{ejpq} = \frac{n\Delta z}{\cos\theta_j} \sigma_{ejpq} \quad (2.7)$$

Once the sublayer downward scattering matrix \mathbf{S}_m^+ is substituted by the transmission matrix expressed as $\mathbf{T}_m = \mathbf{S}_m^+ + \mathbf{T}^+$, and the matrix scattering in the upward direction is known, the single sublayer characterization is completed.

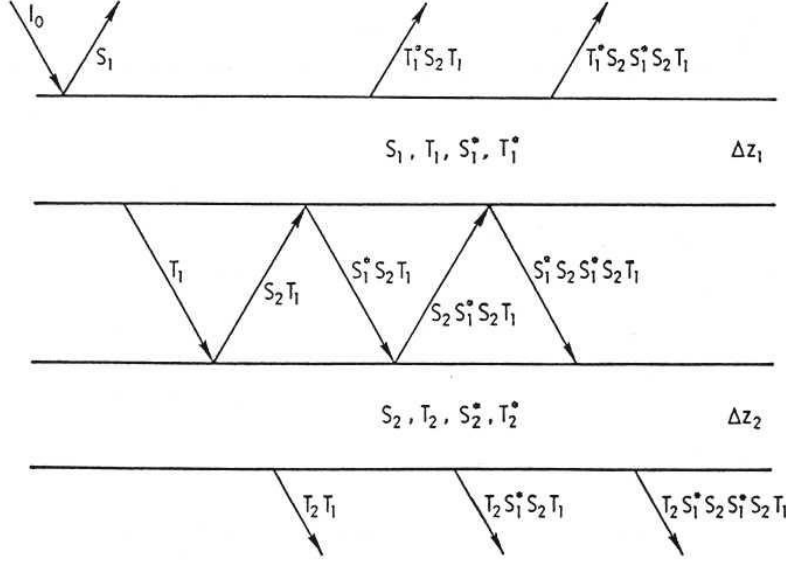


Figure 2.3: Multiple reflections among sublayers

2.2.3 Matrix Doubling Algorithm

In order to take into account the multiple interactions among several sublayers, the approach proposed in [Eom and Fung \(1984\)](#) is adopted. In [Figure \(2.3\)](#) all possible paths that the energy fluxes can follow, are depicted. The total upward scattering of two sublayers is expressed as:

$$\begin{aligned} \mathbf{S}_m &= \mathbf{S}_{1m} + \mathbf{T}_{1m}^* \mathbf{S}_{2m} \mathbf{T}_{1m} + \mathbf{T}_{1m}^* \mathbf{S}_{2m} \mathbf{S}_{1m}^* \mathbf{S}_{2m} \mathbf{T}_{1m} + \dots = \\ &\quad \mathbf{S}_{1m} + \mathbf{T}_{1m}^* \mathbf{S}_{2m} (\mathbf{I} - \mathbf{S}_{1m}^* \mathbf{S}_{2m})^{-1} \mathbf{T}_{1m} \quad (2.8) \end{aligned}$$

whereas the total downward scattering and transmission matrices are obtained by means the following expression

$$\begin{aligned} \mathbf{T}_m &= \mathbf{T}_{2m} \left[\mathbf{I} + \mathbf{S}_{1m}^* \mathbf{S}_{2m} + (\mathbf{S}_{1m}^* \mathbf{S}_{2m})^2 + \dots \right] \mathbf{T}_{1m} = \\ &\quad \mathbf{T}_{2m} (\mathbf{I} - \mathbf{S}_{1m}^* \mathbf{S}_{2m})^{-1} \mathbf{T}_{1m} \quad (2.9) \end{aligned}$$

In the evaluation of the matrices it is assumed that the impinging field comes from the upper half-space, whereas, for starred matrices an impinging field

coming from the lower half-space is assumed. If each sublayer is symmetric, $\mathbf{S}^* = \mathbf{S}$ and $\mathbf{T}^* = \mathbf{T}$. The whole canopy scattering matrix \mathbf{S}_{vm} and transmissivity matrix \mathbf{T}_{vm} are computed for all the Fourier terms, by reiteration of the procedure.

2.3 Backscattering Coefficient Computation

Once the scattering and absorption proprieties are known, and represented as shown in §2.2.2, it is possible to proceed with the last step, i.e. the estimation of the overall backscattering coefficient. To compute it the matrix doubling algorithm is used again, but now between the vegetation layer and the soil, which shows only one upward scattering matrix. So, the following procedure is observed

$$\mathbf{S}_{vgm} = \mathbf{S}_{vm} + \mathbf{T}_{vm}^* \mathbf{S}_{gm} (\mathbf{I} - \mathbf{S}_{vm}^* \mathbf{S}_{gm})^{-1} \mathbf{T}_{vm} \quad (2.10)$$

where \mathbf{S}_{vm} and \mathbf{T}_{vm} represent the upward and downward scattering matrices of the whole vegetation layer, whereas \mathbf{S}_{gm} represents the bistatic scattering of the soil. Since all the matrices are in the Fourier domain, an inverse transformation is needed, which allows to come back in the original system. The equation (2.11) shows the procedure

$$\sigma_{jjpq}^o = \frac{4\pi}{\Delta\theta} \cot \theta_j \sum_{m=0}^{N_\phi/2+1} \frac{1}{a_m} \mathbf{S}_{vgjjpqm} \cos(m(\phi_s - \phi)) \quad (2.11)$$

where $\phi_s - \phi$ is the generic azimuthal scattering angle, and in the particular case of backscattering it is equal to π .

2.4 Emissivity Computation

As previously mentioned, the model may be used to estimate the scattering, in whatever direction. In the previous section, the backscattering computation has been shown, but similar expressions can be obtained for bistatic scattering, which is needed to compute the emissivity. Mainly there are two different ways to estimate the emissivity, of a vegetated soil. The first one is to consider directly the energy fluxes emitted, and subsequently scattered, by the elements which compose the canopy. The second one is based on the energy conservation approach. This last method is adopted in the present model. The main steps are two: the first one is the computation of the bistatic scattering of the whole medium, as described in the previous

pararagraphs, and the second one is the application of the energy conservation law. Since the emissivity is complementary to the reflectivity, it can be expressed by the integral in equation (2.12)

$$e_q(\theta) = 1 - \frac{1}{4\pi} \int_0^{2\pi} \int_0^{\frac{\pi}{2}} \sum_{p=1}^2 \frac{\sigma_{pq}^o(\theta, \theta_s, \phi_s)}{\cos \theta} \sin \theta_s d\theta_s d\phi_s \quad (2.12)$$

Since in the model the space is discretized into angular intervals, the integral is transformed into a summation

$$e_{jq} = 1 - \sum_{i=1}^{N_\theta} \sum_{p=1}^2 \frac{\cos \theta_{si} \sin \theta_{si}}{\cos \theta_j \sin \theta_j} S_{ijpq0} \quad (2.13)$$

In the equation (2.13), only the zeroth order term of the Fourier series is required, differently from the computation of the backscattering shown in equation (2.11).

2.5 Conclusions

The description of the Tor Vergata Model, provided in the present chapter, has had the aim to introduce the used theoretical approach. In the following chapters, specific refinements to same aspects of the model will be described.

Chapter 3

Single Scatterer Model Improvement

The present chapter aims at introducing the electromagnetic refinements of Tor Vergata Model developed during the PhD work. The *curved sheet approximation* and the *hollow stem approximation*, adopted respectively to represent the long curved leaves of corn and the hollow stem of wheat during the ripe period, are here described and tested.

3.1 Basic Definitions

As introduced in Chapter 2, the model, with its modular configuration, allows to consider every kind of scatterer whose bistatic scattering and extinction functions are known. In order to get the required functions, the electromagnetic scattering problem must be solved. The approach is usually based on the integral formulation of the electromagnetic fields. This representation is adopted to represent either the field inside the scatterer and the far scattered field. The problem is depicted in Figure 3.1, where the volume indicated by V may be occupied by dielectric or metallic material. In both cases the solution of the problem is found by means of boundary value considerations.

The properties of the electromagnetic field are completely represented by means of the Maxwell's equations. They define the relationships among the electric field $\mathbf{E}(\mathbf{r})$, magnetic field $\mathbf{H}(\mathbf{r})$, electric displacement field $\mathbf{D}(\mathbf{r})$ and the magnetic induction field $\mathbf{B}(\mathbf{r})$. Hereafter a complex notation, an implicit dependency on spatial position \mathbf{r} and an implicit time variant factor

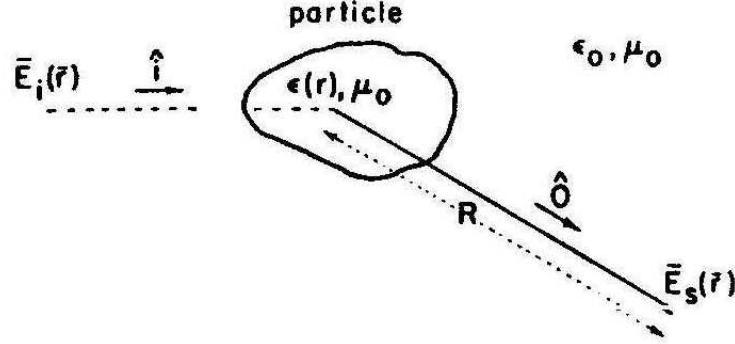


Figure 3.1: Scatterer body and involved fields

$e^{-j\omega t}$ are assumed. The Maxwell's equations are expressed as:

$$\begin{aligned}
 (I) \quad \nabla \times \mathbf{E} - j\omega \mathbf{B} &= \mathbf{J}_m & (III) \quad \nabla \cdot \mathbf{B} &= \rho_m \\
 (II) \quad \nabla \times \mathbf{H} + j\omega \mathbf{D} &= \mathbf{J}_e & (IV) \quad \nabla \cdot \mathbf{D} &= \rho_e
 \end{aligned} \tag{3.1}$$

where

$$\mathbf{D} = \epsilon \mathbf{E} \tag{3.2}$$

$$\mathbf{B} = \mu \mathbf{H} \tag{3.3}$$

where μ and ϵ represent the magnetic and dielectric permittivities. The equations make explicit the relationship among the electromagnetic fields and their sources. Although in nature only electric current distributions are present, magnetic current are taken into account for mathematical convenience.

If a sample of matter is present in the space, where a generic electromagnetic field \mathbf{E}^i is propagating, as depicted in Figure 3.1, a scattered field \mathbf{E}^s arises from the interaction between the body and the incident field. By the addition of the two fields, a total field \mathbf{E} is derived, and its behaviour may be described by means the equations (3.1). This phenomenon is generally called *electromagnetic scattering*.

In literature several approaches are developed to find a suitable expression for the scattered field. One of them is the Stratton-Chu integral equation [Stratton \(1941\)](#), which is entirely based on the Maxwell's equations and scalar-vector Green's theorem. An alternative approach is proposed by Franz [Franz \(1948\)](#), based on the diadic Green's function. A further and probably more common method, utilizes the scalar and vector potential functions [Stratton \(1941\)](#). Because the latter method is used in the present work, further detailed considerations about it are given.

By using the potential theory a couple of vectorial functions are defined, respectively the electric and magnetic Hertz's vector functions

$$\mathbf{\Pi}_e(\mathbf{r}) = \frac{jZ_0}{4\pi k_0} \int_V \mathbf{J}_e(\mathbf{r}') \cdot G(|\mathbf{r} - \mathbf{r}'|) d\tau \quad (3.4)$$

$$\mathbf{\Pi}_m(\mathbf{r}) = \frac{jY_0}{4\pi k_0} \int_V \mathbf{J}_m(\mathbf{r}') \cdot G(|\mathbf{r} - \mathbf{r}'|) d\tau \quad (3.5)$$

where $Z_0 = \sqrt{\mu_0/\varepsilon_0}$ is the free space impedance, k_0 is the free-space propagation constant, \mathbf{J}_e and \mathbf{J}_m are the equivalent electric and magnetic currents. The scalar Green function is expressed as

$$G(|\mathbf{r} - \mathbf{r}'|) = \frac{e^{jk_0|\mathbf{r}-\mathbf{r}'|}}{|\mathbf{r} - \mathbf{r}'|} \quad (3.6)$$

Finally, the relationship among the Hertz's functions and the scattered fields is given by the equations [\(3.7\)](#) and [\(3.8\)](#)

$$\mathbf{E}^s(\mathbf{r}) = \nabla \times \nabla \times \mathbf{\Pi}_e(\mathbf{r}) + jk_0 Z_0 \nabla \times \mathbf{\Pi}_m(\mathbf{r}) \quad (3.7)$$

$$\mathbf{H}^s(\mathbf{r}) = \nabla \times \nabla \times \mathbf{\Pi}_m(\mathbf{r}) - jk_0 Y_0 \nabla \times \mathbf{\Pi}_e(\mathbf{r}) \quad (3.8)$$

The forthcoming step to single out a solution of the problem, is an opportune formulation for electric and magnetic current distributions. In order to do that, the boundary conditions are considered. An example is given by the solution proposed by [Schelkunoff \(1936\)](#).

$$\mathbf{J}_e = \hat{\mathbf{n}} \times \mathbf{H} \quad (3.9)$$

$$\mathbf{J}_m = -\hat{\mathbf{n}} \times \mathbf{E} \quad (3.10)$$

where the Love's equivalent theorem allows to obtain an expression for the currents in [\(3.4\)](#) and [\(3.5\)](#), considering the surface fields.

An alternative solution to the problem is given by considering a further version of the equivalence theorem. To describe the electromagnetic field, inside a generic body, two further fields are defined:

$$\mathbf{P} = \mathbf{D} - \varepsilon_0 \mathbf{E} \quad (3.11)$$

$$\mathbf{M} = \frac{1}{\mu_0} \mathbf{B} - \mathbf{H} \quad (3.12)$$

\mathbf{P} and \mathbf{M} describe the dielectric and magnetic polarization intensities of the matter, respectively. By introducing (3.11) and (3.12) into the Maxwell's equations it is possible to demonstrate that both fields become sources of the scattered field. For dielectric scatterers, the equivalent currents to be used for the Hert'z vectors are expressed as

$$\mathbf{J}_e = -j\omega \mathbf{P} = -j\omega \varepsilon_r (\varepsilon_0 - 1) \mathbf{E}^{int} \quad (3.13)$$

$$\mathbf{J}_m = 0. \quad (3.14)$$

where ε_r is the dielectric relative permittivity and \mathbf{E}^{int} is the field inside the scatterer.

The mathematical approach, previously showed, proposes a rigorous solution of the problem. Due to the complexity of the involved functions, further simplifications need to be done. A first simplification regards the distance between scatterer and observation point. It is assumed:

$$r > \frac{2D^2}{\lambda_0} \quad (3.15)$$

r is the distance between receiving antenna and the scatterer, D is the biggest scatterer dimension and λ_0 is the wavelength. If the relation is fully satisfied, it is supposed that the observation point is far enough from the scatterer, which appears like a waves source located in the origin. Then, it is possible to assume the simplifications of the equations (3.16) and (3.17).

$$|\mathbf{r} - \hat{\mathbf{r}}| = r - \hat{\mathbf{r}} \cdot \hat{\mathbf{r}} + O(r^2) \quad (3.16)$$

$$\nabla \times \approx jk \times \quad (3.17)$$

Hence, the electric and magnetic scattered fields can be expressed as in (3.18)

and (3.19).

$$\begin{aligned} \mathbf{E}^s(\mathbf{r}) = -jk_0 \frac{e^{jk_0 r}}{4\pi r} \left\{ \hat{\mathbf{r}} \times \hat{\mathbf{r}} \times Z_0 \int_V \mathbf{J}_e(\hat{\mathbf{r}}) e^{-jk_0 \hat{\mathbf{r}} \cdot \hat{\mathbf{r}}} d\hat{\mathbf{r}} + \right. \\ \left. + \hat{\mathbf{r}} \times \int_V \mathbf{J}_m(\hat{\mathbf{r}}) e^{-jk_0 \hat{\mathbf{r}} \cdot \hat{\mathbf{r}}} d\hat{\mathbf{r}} \right\} \quad (3.18) \end{aligned}$$

$$\begin{aligned} \mathbf{H}^s(\mathbf{r}) = -jk_0 \frac{e^{jk_0 r}}{4\pi r} \left\{ \hat{\mathbf{r}} \times \hat{\mathbf{r}} \times Y_0 \int_V \mathbf{J}_m(\hat{\mathbf{r}}) e^{-jk_0 \hat{\mathbf{r}} \cdot \hat{\mathbf{r}}} d\hat{\mathbf{r}} + \right. \\ \left. - \hat{\mathbf{r}} \times \int_V \mathbf{J}_e(\hat{\mathbf{r}}) e^{-jk_0 \hat{\mathbf{r}} \cdot \hat{\mathbf{r}}} d\hat{\mathbf{r}} \right\} \quad (3.19) \end{aligned}$$

where the \mathbf{J}_e and \mathbf{J}_m are expressed by means the equation (3.9) and (3.10). It is possible to describe the scattered field like a spherical wave of complex amplitude. It is more evident if the equation (3.18) is expressed as composition of two factors:

$$\mathbf{E}^s(\mathbf{r}) = \frac{e^{jk_0 r}}{r} \mathbf{f}(\hat{\boldsymbol{\theta}}, \hat{\boldsymbol{\iota}}) \quad (3.20)$$

The complex vector $\mathbf{f}(\hat{\boldsymbol{\theta}}, \hat{\boldsymbol{\iota}})$ is called *scattering amplitude function*, and it contains information about amplitude, phase and polarization of the far scattered field in a generic direction $\hat{\boldsymbol{\theta}}$, when an incident electromagnetic wave has propagation direction $\hat{\boldsymbol{\iota}}$.

Once the scattering amplitude function is defined, further functions may be defined to describe the electromagnetic properties of the scatterer. Particular attention is focused towards the scattering and absorption properties. Their mathematical characterization is committed to the *bistatic scattering cross-section*

$$\sigma(\hat{\boldsymbol{\theta}}, \hat{\boldsymbol{\iota}}) = \lim_{r \rightarrow \infty} 4\pi r^2 \frac{|\mathbf{E}^s(\mathbf{r})|}{|\mathbf{E}^i(\mathbf{r})|} = 4\pi |\mathbf{f}(\hat{\boldsymbol{\theta}}, \hat{\boldsymbol{\iota}})|^2 \quad (3.21)$$

in the particular case of $\hat{\boldsymbol{\theta}} = -\hat{\boldsymbol{\iota}}$ the function is called *backscattering cross-section*. Both functions give the scattering capacity, the first one for a generic scattering direction, while the second one in backward direction. The backscattering cross-section assumes importance in view of the very large number of monostatic radar systems. When the overall electromagnetic power is considered, then the function is called *total scattering cross-section*

$$\sigma_t(\hat{\boldsymbol{\iota}}) = \frac{1}{4\pi} \int_{4\pi} \sigma(\hat{\boldsymbol{\theta}}, \hat{\boldsymbol{\iota}}) d\Omega = \frac{W_s}{P_i} \quad (3.22)$$

where W_s is the total scattered power in presence of an incident field whose surface density power is P_i . This function summarizes the reirradiation properties of the scatterer.

It is very important to note that natural elements are dissipative. This means that a further variable is required to characterize the absorption properties. In order to do that, the *absorption cross-section* is used

$$\sigma_a(\hat{\boldsymbol{\iota}}) = \frac{\omega\epsilon_0}{2P_i} \int_V |\Im\{\epsilon_r\}| |\mathbf{E}(\boldsymbol{r})|^2 d\boldsymbol{r} = \frac{W_a}{P_i} \quad (3.23)$$

where W_a represent the overall absorbed energy and $\mathbf{E}(\boldsymbol{r})$ is the field inside the scatterer.

Once either the scattering and absorption properties are characterized, the *extinction cross-section* may be defined as:

$$\sigma_e(\hat{\boldsymbol{\iota}}) = \sigma_t(\hat{\boldsymbol{\iota}}) + \sigma_a(\hat{\boldsymbol{\iota}}) \quad (3.24)$$

This last variable describes the overall interaction between the electromagnetic field, of surface density power P_i , and the observed scatterer of volume V , with permittivity values (ϵ, μ) .

In order to compute $\sigma_e(\hat{\boldsymbol{\iota}})$ we can assess $\sigma_a(\hat{\boldsymbol{\iota}})$ and $\sigma_s(\hat{\boldsymbol{\iota}})$, or more simply use the forward scattering theorem [Van de Hulst \(1957\)](#), which provides the extinction cross section formulation by the knowledge of the imaginary part of the forward scattering function.

$$\sigma_e(\hat{\boldsymbol{\iota}}) = \frac{4\pi}{k_0} \Im\{\mathbf{f}(\hat{\boldsymbol{\iota}}, \hat{\boldsymbol{\iota}})\} \quad (3.25)$$

3.2 Curved Sheet Approximation

In models available at present, long curved leaves are often subdivided into several circular discs, thus losing the continuity of the dielectric object [Bracaglia et al. \(1995\)](#); [Fung \(1994\)](#) and introduced in §2.2.1. An alternative approach, which saves continuity, represents each long leaf as a unique sheet. The theory was developed by [Sarabandi et al. \(1988\)](#) and it aimed at computing the scattering of dielectric curved sheets, but serious limits do not allow to use it inside operative model. It only compute the backscattering coefficient for one fixed position of the scatterer.

In this section, the theoretical formulation of curved sheet backscattering developed in [Sarabandi et al. \(1988\)](#) is generalized, in order to consider any possible scattering direction and any possible azimuth orientation of the sheet. A formulation for the scattering amplitude function is developed so

that the forward scattering theorem can also be applied in order to compute the leaf extinction cross section.

Typical corn leaf shapes are depicted in Figure 3.2, where it is visible the enhanced curvature which characterizes its geometry.



Figure 3.2: Generic corn leaves shape

3.2.1 Theory

The dielectric curved sheet representation was proposed in [Sarabandi et al. \(1988\)](#), where the backscattering cross section of the leaf was computed for the case of normal incidence of the electromagnetic field. Since the method used in Tor Vergata Model needs the bistatic scattering and extinction cross

sections of all the elements that make up the vegetation canopy, a general expression for $\sigma(\hat{\boldsymbol{o}}, \hat{\boldsymbol{l}})$ of the dielectric sheet was developed, in order to consider any possible direction of incidence and scattering, as well as any possible orientation of the sheet. The leaf geometric shape is depicted in Figure 3.3; the leaf is a curved section of width a and length $b = \beta\rho$ on the surface of a sphere with radius ρ .

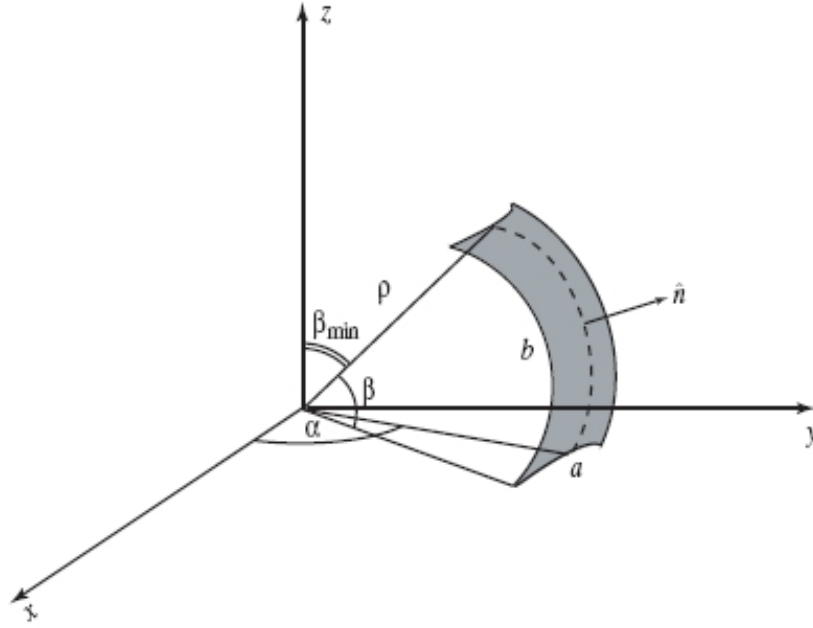


Figure 3.3: Geometrical and angular dimensions of the curved sheet

Once the reference system is set, all the electromagnetic variables must be referred to it. The first known variables are the incident electric field \mathbf{E}^i and the related magnetic field $\mathbf{H}^i = Y_0 \hat{\boldsymbol{l}} \times \mathbf{E}^i$.

In order to get the induced current on the curved sheet, the hypothesis of a perfect conductor is made at first, and the induced current on the surface of the sheet in the physical optics approximation, J_e^{PC} , is obtained as

$$\mathbf{J}_e^{PC} = \hat{\boldsymbol{n}} \times (\mathbf{H}^i + \mathbf{H}^s) \approx 2\hat{\boldsymbol{n}} \times \mathbf{H}^i \quad (3.26)$$

$$\mathbf{J}_m^{PC} = \hat{\boldsymbol{n}} \times (\mathbf{E}^i + \mathbf{E}^s) = 0 \quad (3.27)$$

where the electric current is expressed in the $(\hat{\boldsymbol{x}}, \hat{\boldsymbol{y}}, \hat{\boldsymbol{z}})$ system. The following step is to reformulate \mathbf{J}_e^{PC} by using a local coordinate system $(\hat{\boldsymbol{\xi}}, \hat{\boldsymbol{\eta}}, \hat{\boldsymbol{\zeta}})$,

where $\hat{\boldsymbol{\eta}}$ and $\hat{\boldsymbol{\zeta}}$ describe the local tangent plane at the curved sheet. They are parallel and perpendicular to the incident plane described by the unit vectors $\hat{\boldsymbol{n}}$ and $\hat{\boldsymbol{t}}$, respectively.

$$\mathbf{J}_e^{PC} = \left(A\hat{\boldsymbol{\eta}} + B\hat{\boldsymbol{\zeta}} \right) e^{-jk_0\rho(\sin\theta\cos\phi\sin\theta_i + \cos\theta\cos\theta_i)} \quad (3.28)$$

where coefficient A and B are available in [Della Vecchia et al. \(2004\)](#).

Once the local coordinate system is adopted, the amplitude of the electric current is reformulated within the new coordinate system. This new formulation allows an easy transition from metallic to dielectric matter, by means of the introduction of suitable reflection coefficients, respectively for TE and TH polarized fields.

$$\mathbf{J}_e = \left(A\Gamma_H(\psi)\hat{\boldsymbol{\eta}} + B\Gamma_E(\psi)\hat{\boldsymbol{\zeta}} \right) e^{-jk_0\rho(\sin\theta\cos\phi\sin\theta_i + \cos\theta\cos\theta_i)} \quad (3.29)$$

with

$$\Gamma_E(\psi) = \left(1 + \frac{2R}{Z_0} \sec\psi \right)^{-1} \quad (3.30)$$

$$\Gamma_H(\psi) = \left(1 + \frac{2R}{Z_0} \cos\psi \right)^{-1} \quad (3.31)$$

$$\cos\psi = -\hat{\boldsymbol{t}} \cdot \hat{\boldsymbol{n}} \quad (3.32)$$

$$R = \frac{jZ_0}{k_0\tau(\varepsilon - 1)} \quad (3.33)$$

where τ is the sheet thickness, ε the dielectric permittivity, Z_0 and k_0 the free space propagation impedance and the free propagation constant. From the induced current, the Hertz's vector can be found and, afterwards, the scattered electric field in the far field approximation.

$$\mathbf{E}^s(\mathbf{r}) \approx \frac{e^{jk_0r}}{k_0r} \frac{jZ_0\rho^2}{4\pi} \int_{sheet} -k_0^2(\mathbf{r} \times \mathbf{r} \times \mathbf{J}_e) e^{-jk_0\hat{\mathbf{r}} \cdot \hat{\mathbf{r}}} \sin\theta \, d\theta \, d\phi \quad (3.34)$$

As proposed for all the models (e.g. [Eom and Fung \(1984\)](#); [Le Vine et al. \(1983\)](#)), where an exact solution of the problem is not available, the individuation of the applicability limits is a very important step. Regarding to the curved sheet theory, besides the conventional simplifications implicitly assumed into the equation (3.18) (plane incident wave and far scattered field), three further main approximations have been assumed and are analyzed in

Ulaby and Elachi (1990, Chapter 3). The first one regards the validity of the equation (3.26). It assumes that local scattering, on the curved surface, follow the same reflection rules, which involve a perfect plane structure, hence it is valid when the sphere radius is large with respect to the wavelength: $\rho/\lambda_0 \rightarrow \infty$. The second point raises with the the subdivision of the scatterer into two zones, one directly illuminated by the incident field, and a second one not illuminated by the field, called shadow zone, which is not considered in the scattering phenomena. A third and last point regards the resistive sheet approximation, and more directly the thickness of the dielectric body. In order to apply the approximation, with a good degree of reliability, it is strictly required a very thin sheet thickness: $\tau/\lambda_0 \rightarrow 0$. In this way, the dielectric body, can be fully replaced by an electric current distribution expressed by the equation (3.33).

3.2.2 Results

Some comparisons between the theoretical results obtained with the disc and the sheet geometry are here shown. The plots in Figure 3.4–3.6(b) report the simulated backscattering coefficient vs the incidence angle at L-, C- and X-band. Computations have been carried out applying the method described in §3.2.1. Theoretical canopies composed only of leaves have been considered, and multiple scattering between different leaves has been included. Two cases for the disc and sheet models are considered, which correspond to typical geometrical leaf parameters of wheat and corn crops at their full growth stage:

- Wheat
 - Discs with radius $a_d = 0.65$ cm, and thickness $\tau = 0.2$ mm, Leaf Area Index (LAI) = 5
 - Sheets of length $b_s = 27$ cm and width $a_s = 1.3$ cm, $\tau = 0.2$ mm, LAI = 5
- Corn
 - Discs with radius $a_d = 4.2$ cm, $\tau = 0.3$ mm, LAI = 3.6
 - Sheets with length $b_s = 50.64$ cm, width $a_s = 8.4$ cm, $\tau = 0.3$ mm and LAI = 3.6

In this case, the presence of ribs, as reported by ground truth measurements on corn crops, has also been introduced: they have been subdivided into thin

cylinders with radius $a_c = 0.15$ cm, and length equal to the disc diameter $l_c = 8.4$ cm.

In our simulations, the case of azimuthal symmetry has been considered ($0 \leq \alpha \leq 360^\circ$) both for discs and sheets. The elevation angle of discs (i.e. the angle between the normal to the single disc and the z axis of Figure 3.3) has been considered uniformly distributed between 0° and 90° .

When comparing the two model results, it must be borne in mind that in the sheet model an extra parameter is introduced to describe the leaf geometry, that is its radius of curvature. In the following examples, the angle β , visible in Figure 3.3, has been fixed equal to 90° , so that the radius of curvature is $\rho = 17.2$ cm for wheat, and $\rho = 32.2$ cm for corn.

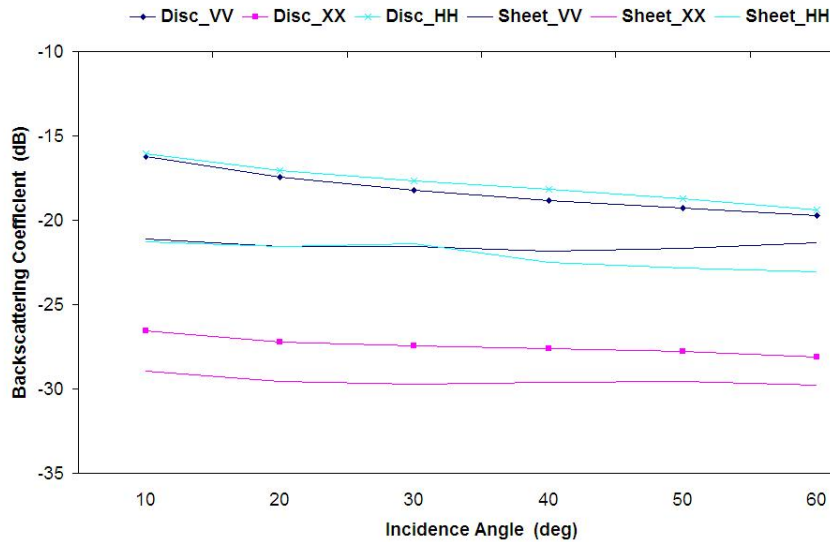
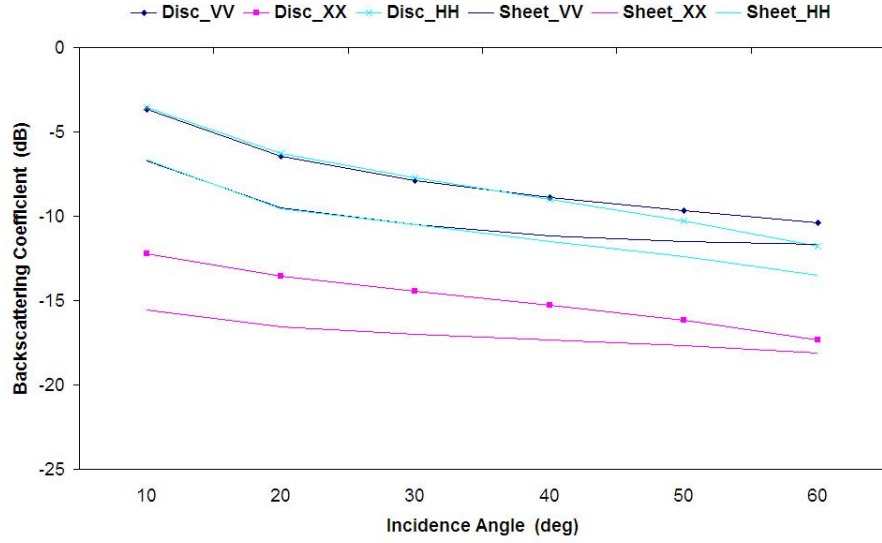


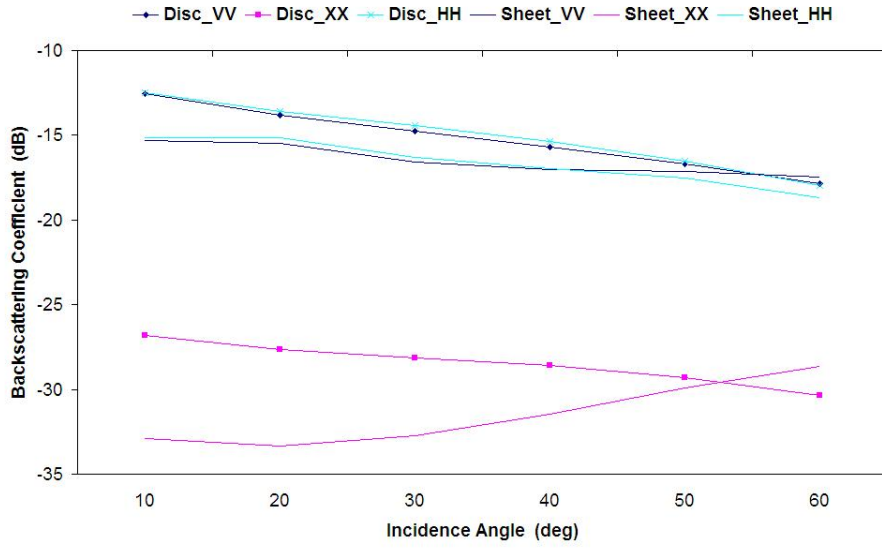
Figure 3.4: Backscattering coefficient of a canopy of corn leaves at L-band

At L-band, the Rayleigh-Gans approximation has been applied to discs, while at higher frequencies, the Physical Optics has been used.

At L-band the results for the wheat canopy are not reported because the modeled backscattering coefficient is below -35 dB, due to the small dimension of the scatterers and because suitability of the approximations are not fully satisfied. Looking at Figure 3.4–3.6(b), the following considerations can be drawn. For a given set of frequencies, angles and polarizations, the backscattering coefficient of wheat leaves is lower than the one of corn leaves. Both for corn and wheat leaves, the backscattering coefficient increases with

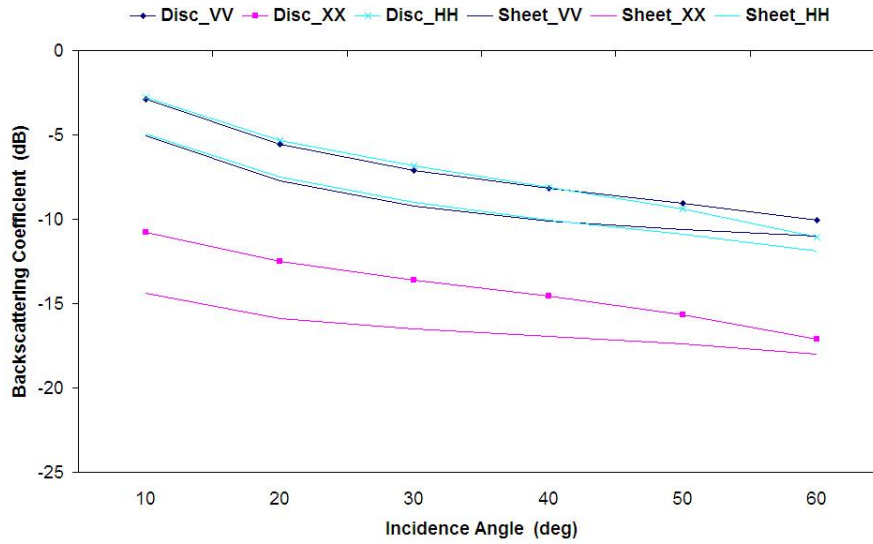


(a)

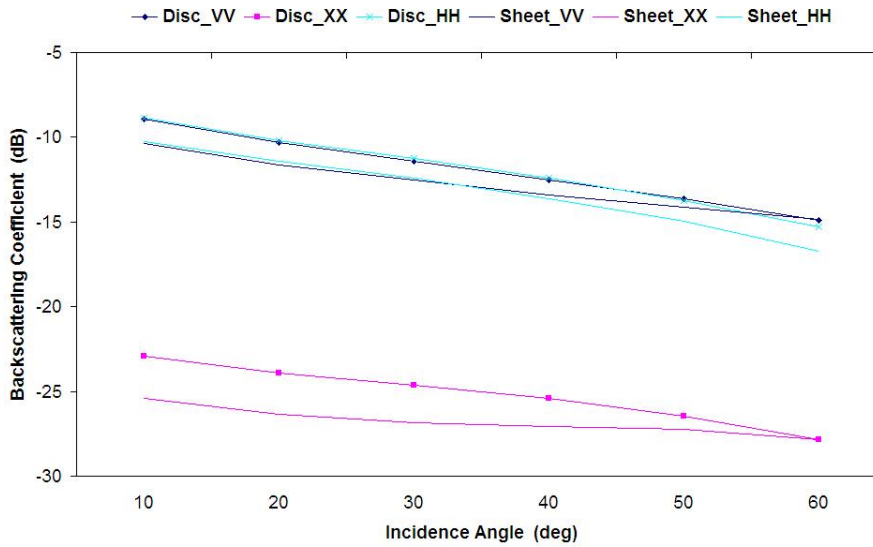


(b)

Figure 3.5: Backscattering coefficient for a canopy at C-band for of: (a) corn leaves; (b) wheat leaves.

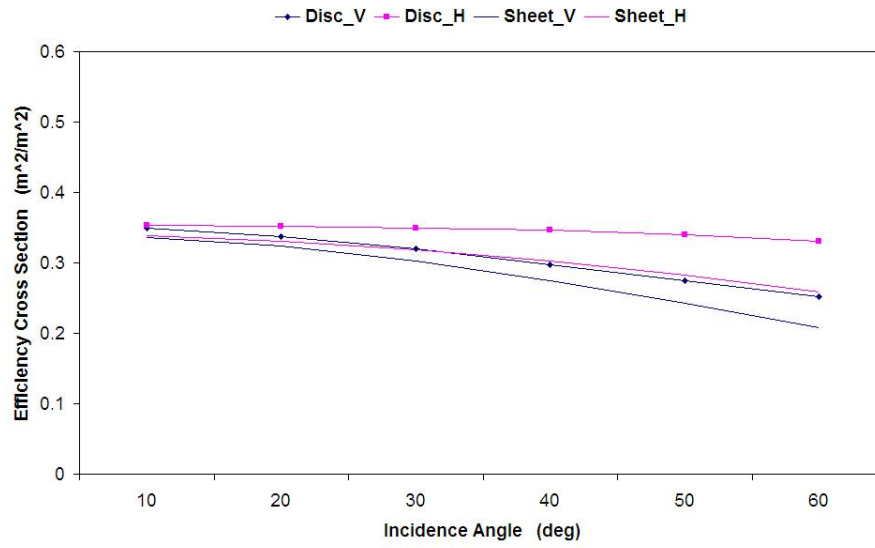


(a)

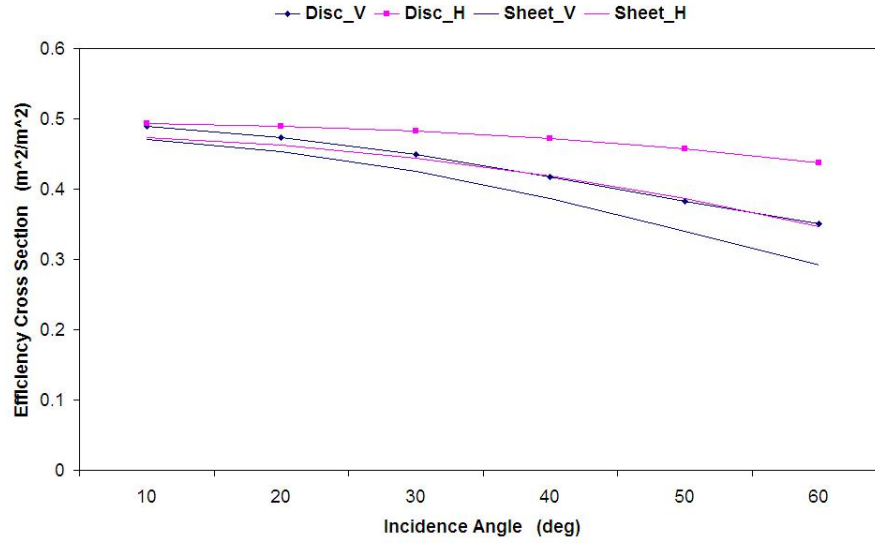


(b)

Figure 3.6: Backscattering coefficient for a canopy at X-band for of: (a) corn leaves; (b) wheat leaves.



(a)



(b)

Figure 3.7: Extinction efficiency of corn leaves: (a) C-band; (b) X-band.

frequency. The trend versus the incidence angle is generally decreasing, showing a slope which is higher with the disc model than with the sheet model. Especially at larger angles, the sheet model shows a reduced sensitivity to the incidence angle. Some anomalous behaviours are observed at C-band, HV polarization, and are associated to very low backscattering values. In general, backscattering values of discs are higher than those of sheets, especially at low angles. Many effects could contribute to this result; one of them could be the fact that, in a disc canopy with azimuthal symmetry, some discs have a nearly horizontal orientation which enhances backscattering, while the sheets, because of their curvature, smooth this effects. In Figure 3.7(a)–(b), the extinction efficiency (i.e. the extinction cross section normalized to the area) of discs and sheets used in the corn representation has been reported for C- and X-band. The sheet extinction efficiency tends to be lower than the disc one; also the difference between the two polarizations of the sheet extinction efficiency tends to decrease with respect to the disc case.

In summary, the introduction of a geometric representation that maintains the curvature of the single leaf yields a backscattering which may be quite different from that of disc shaped leaves. However, when the whole crop canopy is to be considered, the differences between the overall backscattering coefficients obtained by the two approaches may be weaker because of the introduction of soil and stem contributions.

3.3 Hollow Stem Approximation

Dielectric homogeneous cylinders are usually chosen to model tree trunks and crop stems [Ulaby et al. \(1990\)](#), and their extinction and scattering cross sections are simulated assuming that the internal field within the finite-length cylinder is the same as the one induced within an infinite-length cylinder [Karam and Fung \(1988\)](#); [Seker and Schneider \(1988\)](#) having the same permittivity of the vegetation component. The problem of scattering from tree trunks is examined in [Kolawole \(1992\)](#); [Lin and Sarabandi \(1995\)](#), where the radial variation of dielectric constant from the bark to the core is taken into account. They consider a stratified cylinder, with radially layered permittivity, and with radius larger than the wavelength. Besides, in their formulations, they consider cylinders terminated over the ground surface.

In this section, following the theory developed in [Kolawole \(1992\)](#), the field on the surface of a hollow infinite cylinder is found at first. Then, applying the equivalence theorem [Lin and Sarabandi \(1995\)](#), the scattered field

from a hollow lossy cylinder of finite length and any radius is obtained, and it is applied to the typical dimensions and permittivities of wheat stems, for arbitrary values of the incidence and scattering angles of the electromagnetic field.

3.3.1 Theory

The present section briefly introduces the theory adopted to represent the hollow cylinder electromagnetic scattering [Della Vecchia et al. \(2006c\)](#). To solve the problem of scattering from a hollow cylinder, three regions have been identified which are delimited by two coaxial cylinders with radii a_{int} and a_{ext} . Figure 3.8 shows the section of the hollow cylinder: the inner region is the cavity, numbered as 1, and has a circular section with radius a_{int} and with dielectric constant ε_0 . Region 2 has a circular ring section limited by circles of radii a_{int} and a_{ext} and dielectric constant ε_r equal to the one of vegetation. The outer region 3 is the free space, outside the external cylinder, with dielectric constant ε_0 .

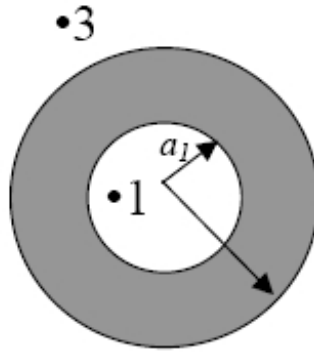


Figure 3.8: Cross section of a hollow cylinder with inner radius a_{int} and outer radius a_{ext}

A cylindrical coordinate system (ρ, ϕ, z) is used, with the z -axis parallel to the cylinder axis. An electromagnetic field impinging from region 3, on the cylinder in the direction making an angle $\pi - \theta_i$ with the z -axis, is

considered.

$$E_z^i = -E_0 \sin \theta_i e^{jk_0 \rho \sin \theta_i \cos \phi} e^{jk_0 z \cos \theta_i} \quad (3.35)$$

Using the addition theorem for the Bessel functions, the field in equation (3.35) can be expressed by the following series of Hankel functions of the first and second kind

$$E_z^i = \sum_n \left(a_n^i \mathcal{H}_n^{(1)}(k_\rho r) + b_n^i \mathcal{H}_n^{(2)}(k_\rho r) \right) F_n(\phi, z) \quad (3.36)$$

$$H_z^i = \sum_n \left(c_n^i \mathcal{H}_n^{(1)}(k_\rho r) + d_n^i \mathcal{H}_n^{(2)}(k_\rho r) \right) F_n(\phi, z) \quad (3.37)$$

with

$$F_n(\phi, z) = e^{j(n\phi + k_z z)} \quad (3.38)$$

$$k_\rho = k_0 \sin \theta_i \quad (3.39)$$

$$k_z = k_0 \cos \theta_i \quad (3.40)$$

The same expression is adopted for the z component of the scattered field where, in accordance with the outgoing direction of the field, only the Henkel functions of the first kind are adopted.

Once the field component, belonging to the incident plane is computed, the perpedicular one must be evaluated. It is possible to retrieve the expression, directly from the (I) and (II) Maxwell's equations (3.1), which allows to express the ϕ component of the field as a function of the z component. In such a way it is possible to express the field in the generic region (R) of the space with the following expression:

$$\begin{bmatrix} E_z^R \\ H_z^R \\ E_\phi^R \\ H_\phi^R \end{bmatrix} = \sum_n \chi_n^R(\rho) \begin{bmatrix} a_n^R \\ b_n^R \\ c_n^R \\ d_n^R \end{bmatrix} F_n(\phi, z) \quad (3.41)$$

where

$$\chi_n^R(\rho) = \begin{bmatrix} \mathcal{H}_n^{(1)} & \mathcal{H}_n^{(2)} & 0 & 0 \\ 0 & 0 & \mathcal{H}_n^{(1)} & \mathcal{H}_n^{(2)} \\ -\frac{nk_z^R}{\rho(k_\rho^R)^2} \mathcal{H}_n^{(1)} & -\frac{nk_z^R}{\rho(k_\rho^R)^2} \mathcal{H}_n^{(2)} & -\frac{j\omega\mu}{k_\rho^R} \mathcal{H}_n^{(1)} & -\frac{j\omega\mu}{k_\rho^R} \mathcal{H}_n^{(2)} \\ \frac{j\omega\varepsilon_R}{k_\rho^R} \mathcal{H}_n^{(1)} & \frac{j\omega\varepsilon_R}{k_\rho^R} \mathcal{H}_n^{(2)} & -\frac{nk_z^R}{\rho(k_\rho^R)^2} \mathcal{H}_n^{(1)} & -\frac{nk_z^R}{\rho(k_\rho^R)^2} \mathcal{H}_n^{(2)} \end{bmatrix} \quad (3.42)$$

Note that the argument $k_\rho^R \rho$ of the Hankel functions is understood.

It is possible to connect the coefficients of the fields in region 3 to the coefficients of the fields in region 1, by iteratively applying the boundary conditions on the discontinuity surfaces within the hollow cylinder. Following Kolawole (1992), the continuity of the tangential components at the surfaces with $\rho = a_{int}$ and $\rho = a_{ext}$ is enforced. The final result of the iterative procedure is a system of 4 equations and 4 unknown, represented below:

$$\begin{bmatrix} a_n^s \\ a_n^1 \\ c_n^1 \\ c_n^s \end{bmatrix} = -j^n \frac{\sin \theta_j}{2} \begin{bmatrix} -1 & \alpha_1 & \alpha_2 & 0 \\ 0 & \alpha_3 & \alpha_4 & 0 \\ 0 & \alpha_5 & \alpha_6 & -1 \\ 0 & \alpha_7 & \alpha_8 & 0 \end{bmatrix}^{-1} \begin{bmatrix} a_n^s \\ a_n^1 \\ c_n^1 \\ c_n^s \end{bmatrix} \quad (3.43)$$

by the solution of the equation (3.43), it is possible to obtain the coefficients necessary to describe the scattered field, described with the equation (3.41), in the outside region ($R = 3$).

In order to calculate the scattered field of a finite length cylinder, the surface current equivalent theorem, introduced in §3.1 and represented by the equations (3.9) and (3.10) are adopted. Hence, by following the expressions proposed in Lin and Sarabandi (1995), a valid expression for a finite dielectric hollow cylinder is obtained.

3.3.2 Results

The theory introduced in the previous section, is now adopted in order to investigate the impact of the stem hollowness. Hollow cylinder variable have been selected in such a way as to correspond to real wheat canopies, because the internal radius is not measurable, it is necessary to adopt a method based on the weight and external dimensions. The required information, which allow to assess the internal radius are the height H , fresh and dry weight W_f and W_d , and the dry matter density. Once all these data are collected, the following formulas can be used at first to estimate the stem volume V_h

$$V_h = \frac{W_f - W_d}{\rho_w} + \frac{W_d}{\rho_d} \quad (3.44)$$

and finally the internal radius a_{int}

$$a_{int} = \sqrt{a_{ext}^2 - \frac{V_h}{\pi H}} \quad (3.45)$$

Information collected at Avignon site in 1993 Ferrazzoli et al. (2000), sampled with a repetition time of 3 days, have been used in order to reproduce the whole wheat growth cycle. Figure 3.9 shows the trends of internal and external radii. The stem is full until about the day of year 130 ($a_{int} = 0$). Then the internal radius increases rapidly and reaches values higher than 0.15 cm in the ripening period.

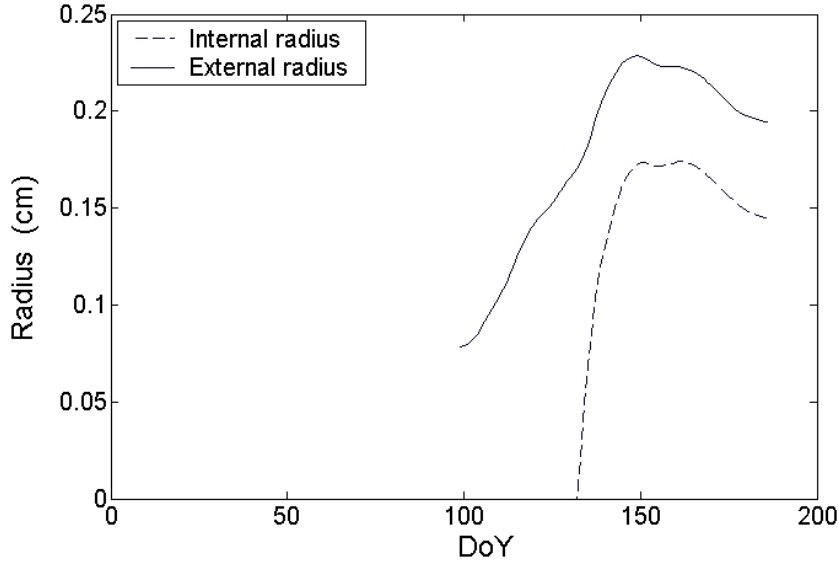
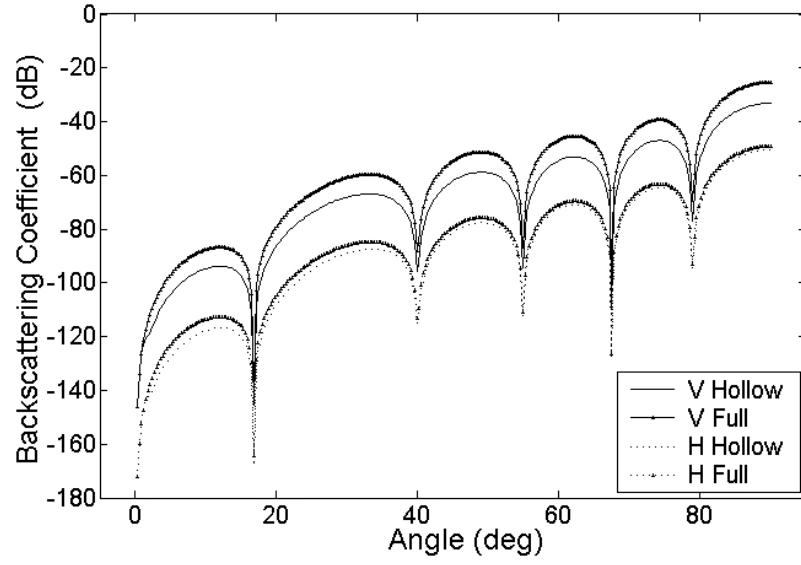


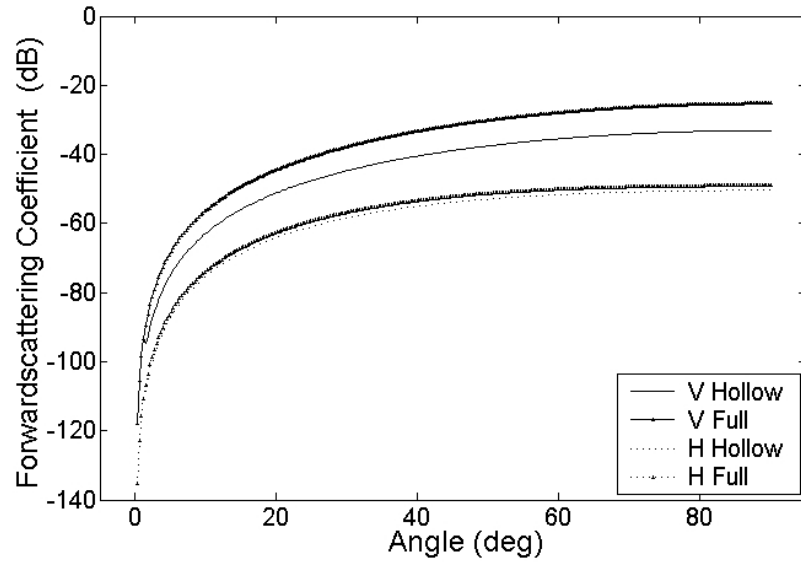
Figure 3.9: Trend of internal and external radii for a whole wheat growth cycle

First, some backscattering and forward scattering trends are given for a hollow stem of radii a_{int} and a_{ext} , and a full stem of radius a_{ext} , in correspondence of day of year 145, when the differences between external and internal radius reach the maximum value. Figure 3.10(a)-(b) shows respectively the back- and forward scattering cross section coefficients at L-band (1.2 GHz). Similarly it is proposed at C-band (5 GHz) in Figure 3.11(a)-(b) and X-band (10 GHz) in Figure 3.12(a)-(b).

In the following, the attenuation produced from a hollow stem of radii a_{int} and a_{ext} , and a full stem of radius a_{ext} are compared. Figures 3.13(a)-(b) propose the attenuation at L-band (1.2 GHz), respectively for incident angles of 25° and 45° . Similar trend are given at C-band (5 GHz) in Figures 3.14(a)-(b) and at X-band (10 GHz) in Figure 3.15(a)-(b). The attenuation is computed by taking into account also the stem density N (m^{-2})

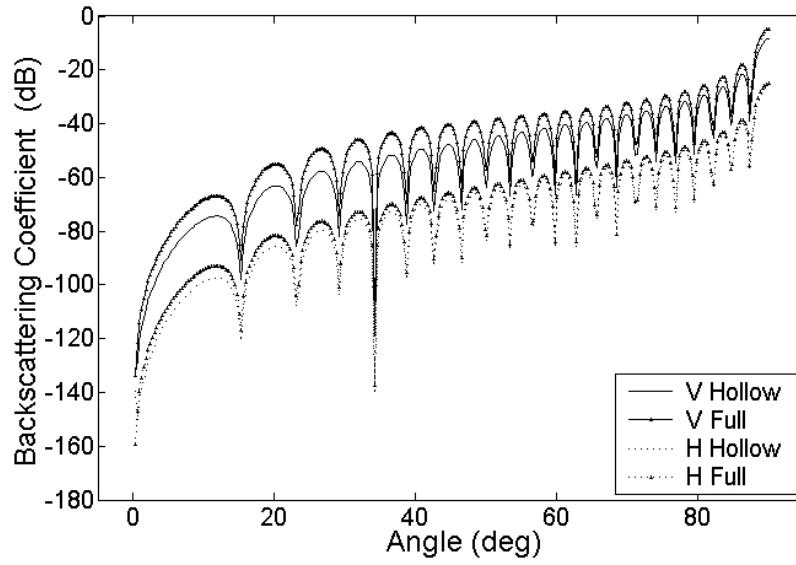


(a)

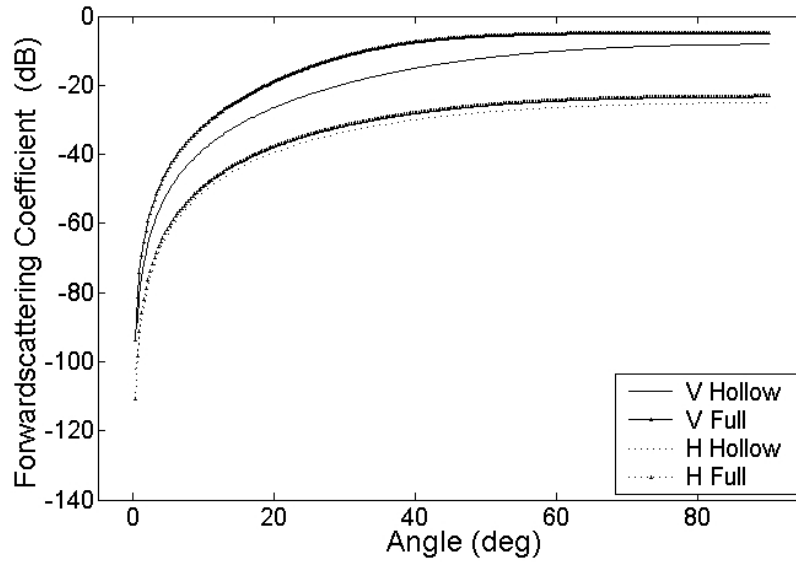


(b)

Figure 3.10: Backscattering (a) and forward scattering cross section coefficients (b) at L-band (1.2 GHz)

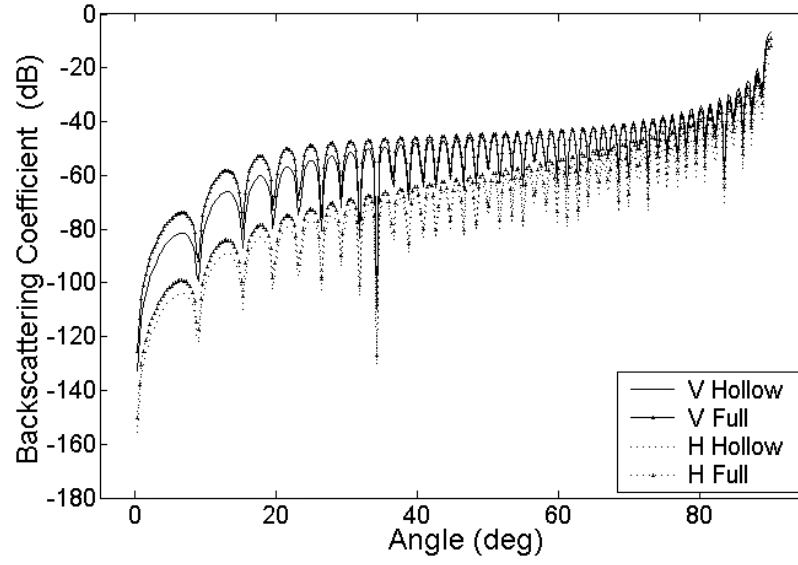


(a)

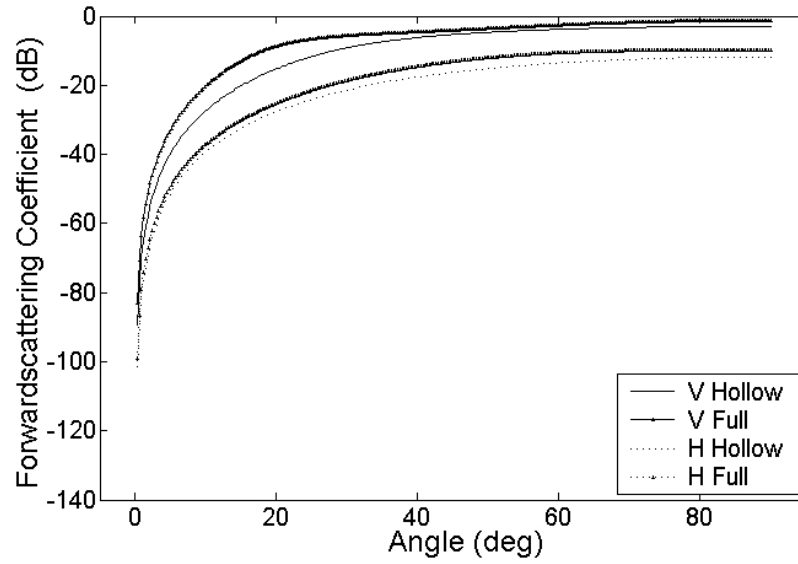


(b)

Figure 3.11: Backscattering (a) and forward scattering cross section coefficients (b) at C-band (5 GHz)

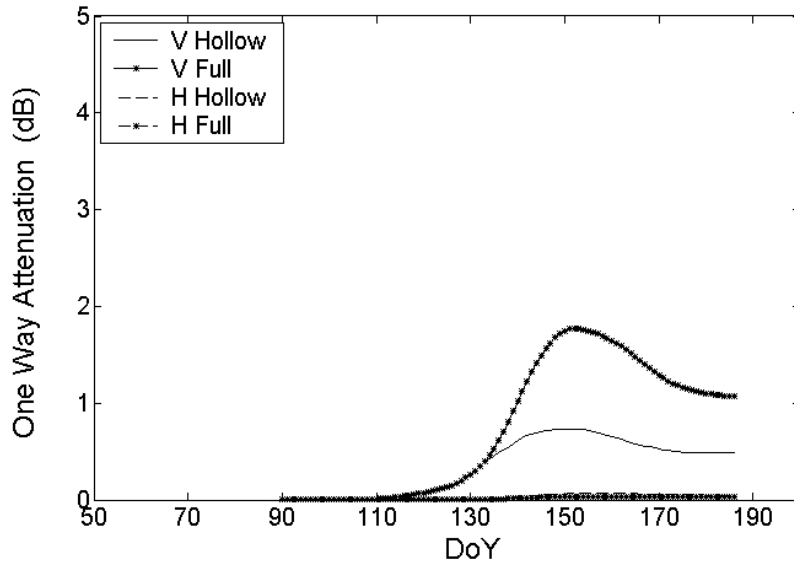


(a)

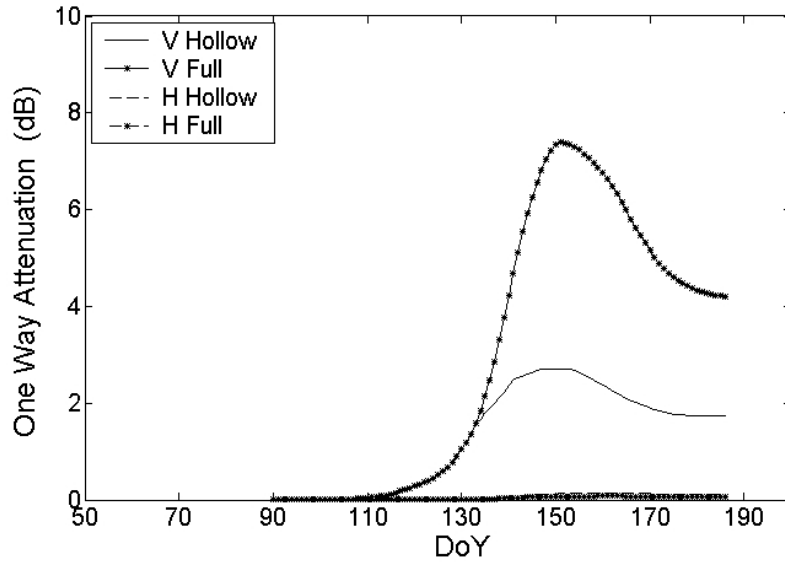


(b)

Figure 3.12: Backscattering (a) and forward scattering cross section coefficients (b) at X-band (10 GHz)

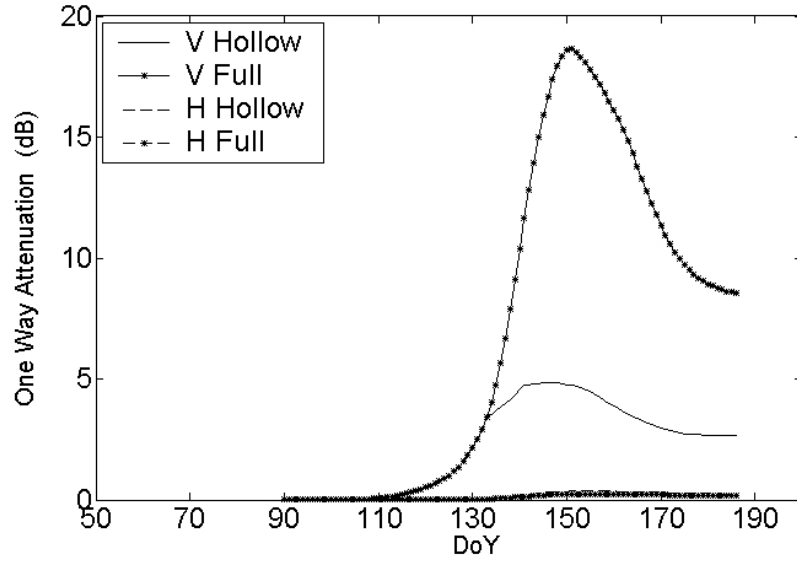


(a)

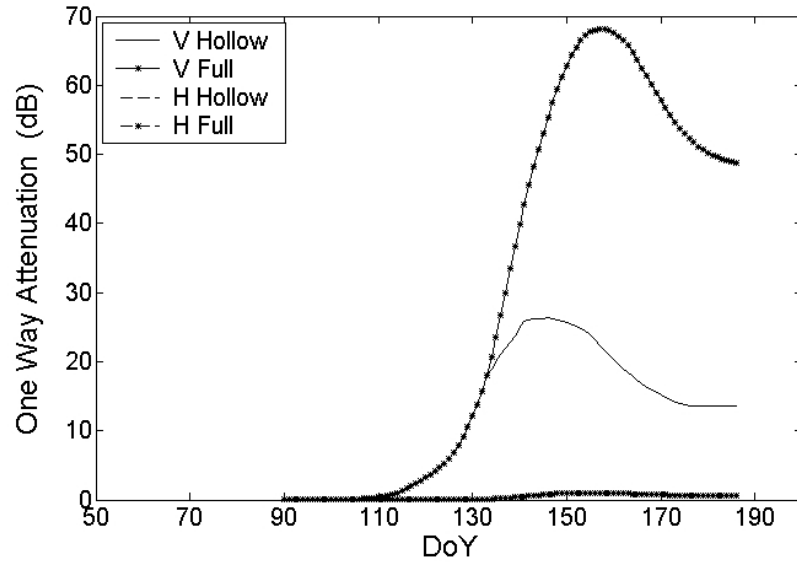


(b)

Figure 3.13: Attenuation trends at L-band (1.2 GHz): (a) incident angle $\theta_i = 25^\circ$; (b) incident angle $\theta_i = 45^\circ$.

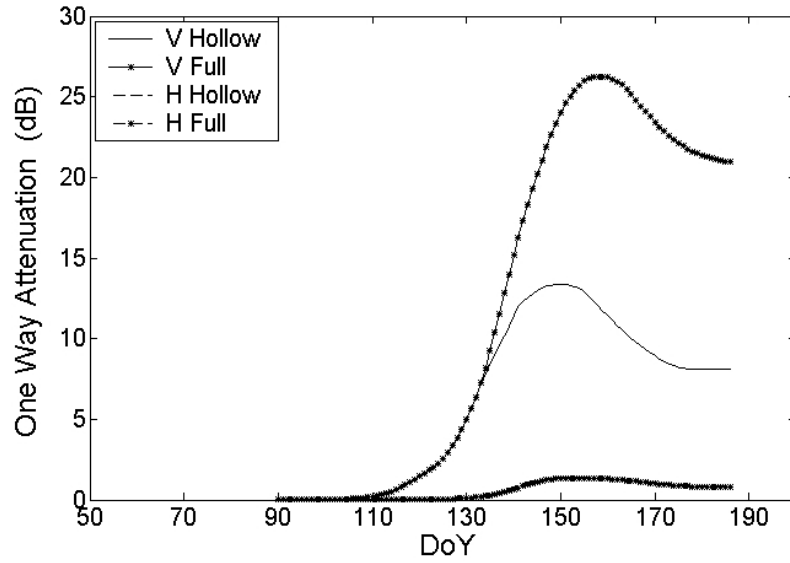


(a)

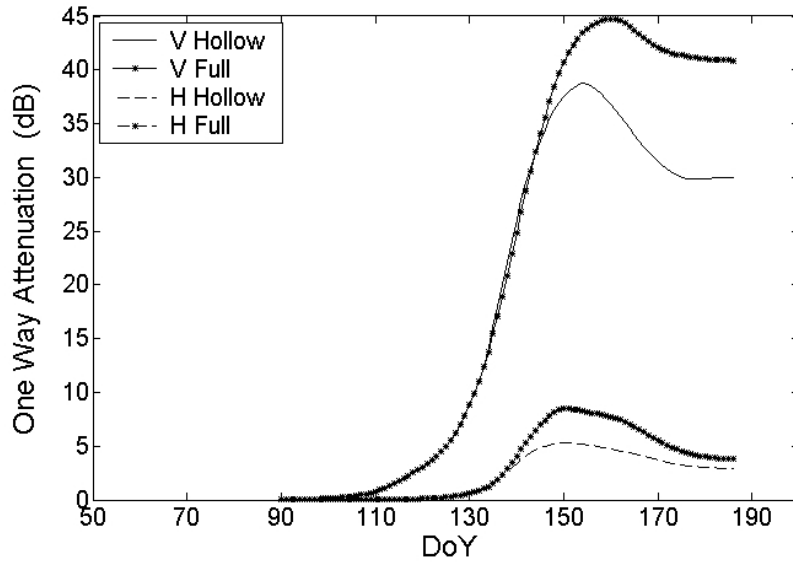


(b)

Figure 3.14: Attenuation trends at C-band (5 GHz) (a) incident angle $\theta_i = 25^\circ$; (b) incident angle $\theta_i = 45^\circ$.



(a)



(b)

Figure 3.15: Attenuation trends at X-band (10 GHz) (a) incident angle $\theta_i = 25^\circ$; (b) incident angle $\theta_i = 45^\circ$.

measured in Avignone site, by adopting the equation (3.46).

$$A = 10 \cdot \log(e^{N\sigma_e \sec \theta_i}) \quad (3.46)$$

where σ_e represent the extinction cross section of a single stem, computed by means of the forward scattering theorem and θ_i represents the incident angle.

Results of the simulations show that cylinder scattering and attenuation at vertical polarization are significantly reduced by the hollowness of the cylinder. The main differences are visible at V polarization, where, due to the vertical orientation of the stems, the electromagnetic interaction is more evident. The highest effects, concerning the attenuation, for a layer composed by vertical stems, are observed at C-band, where maximum values of attenuation reduction are about 10 dB at 25° incidence angle, and more than 30 dB at 45° . At horizontal polarization, the difference between the two approaches is considerably lower, both in scattering and attenuation. At L and C-band, attenuation keeps lower than 0.5 dB, and increases up to about 3 dB at X-band, 45° incidence angle.

3.4 Conclusions

In this chapter, a formulation for the bistatic scattering cross section of dielectric curved sheets has been derived, and has been included in the electromagnetic model of crops developed at Tor Vergata. Leaves are usually represented by dielectric circular discs, but curved sheets preserves the continuity of long leaves, thus better representing their geometrical properties. Theoretical simulations of backscattering from wheat and corn canopies made up of circular discs or sheets have been shown and compared in this chapter. Differences between the two approaches are present, especially at low angles, when the sheet model provides a lower backscattering value with respect to the disc model.

Moreover a dielectric hollow cylinder has been adopted to reproduce the stem hollowness of the wheat during and after the ripe growth period. Significant differences have been observed for the scattering and attenuation values at V polarization at L, C and X-bands, while at H polarization slight differences have been only seen at X-band.

Chapter 4

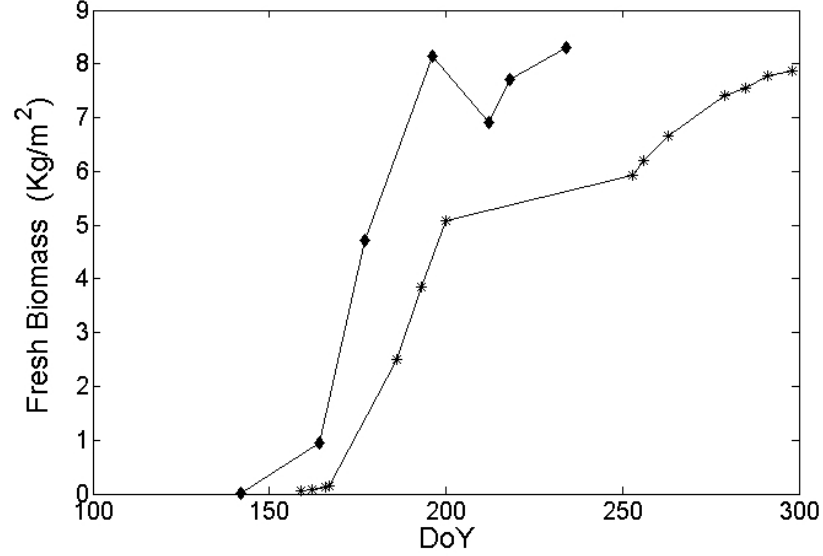
Application to Agricultural Fields

The present chapter describes propose some comparisons between model simulations and experimental data for some fields. Comparisons have a twofold purpose: first to investigate about the reliability of the new theoretical approaches described in Chapter 3, second to propose a systematic validation of the whole electromagnetic model. Both corn and wheat are considered, in different field sites and with the support of detailed ground data collection. The analysis is concentrated in the C-band (5.3 GHz) where a large data collection is available from ERS1/2, ENVISAT and RADARSAT.

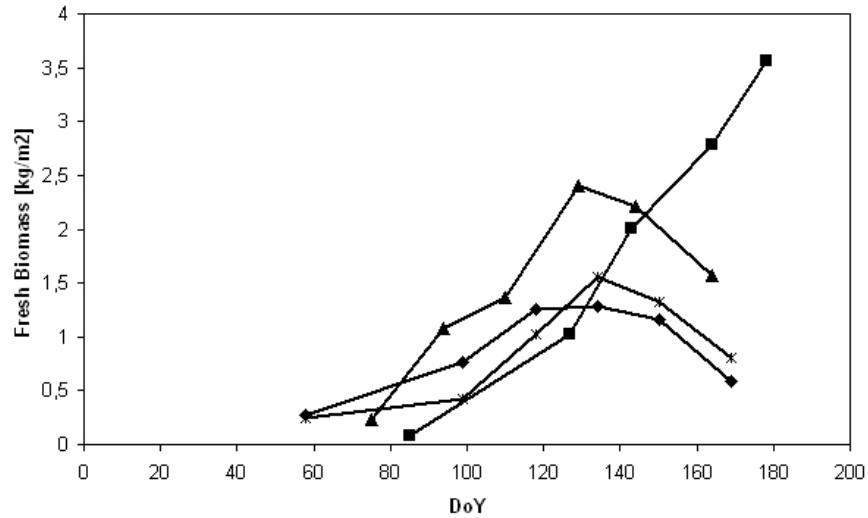
4.1 Experimental data set

In this section, the sites used for the model validation are described. Radar data and ground data cover one corn field at the Central Plain site (CH), three wheat fields at the Matera site (I) (collected during two different campaigns), one corn field and one wheat field at the Loamy site (B).

In order to give a general view, the crop biomass trends measured on each site during the temporal window of our interest are reported in Figure 4.1(a) for the corn fields, and Figure 4.1(b) for the wheat fields. It can be observed that the growth cycles on the two corn plantations are shifted with respect to each other (at the Loamy site the cycle is earlier). The four wheat fields present differences both in time location and in maximum values.



(a)



(b)

Figure 4.1: Fresh biomass measured on the fields: (a) 2 corn fields: Central Plain (Dots), Loamy (Diamonds) (b) 4 whet fields: Matera 2001 campaign (Triangles), Field 5 at Matera 2003 campaign (Diamonds), Field 6 at Matera 2003 (Stars), Loamy (Squares)

4.1.1 Central Plain Data Set

Several measurements over crops were performed at the Swiss Central Plain site using RASAM, from 1984 to 1991. RASAM is a ground-based microwave radiometer/scatterometer system. Signatures were collected at several frequencies, at several angles between 10° and 70° , and at VV, HH, HV and VH polarizations [Wegmüller \(1993\)](#). We have considered a time series of co- and cross-polarized backscattering coefficients collected at C-band over a corn field covering a long period, from May 1988 to the end of October 1988 at 30° incidence angle. The field was dense, and reached a maximum biomass of about 8 kg/m^2 in full growth. Ground data were not sufficiently detailed to provide all the inputs required by the model, but covered some significant parameters such as soil moisture, soil roughness, crop height, wet and dry biomass. They are reported in [Table 4.1](#) together with other parameters used as model inputs, which were calculated by means of an empirical routine implemented on the basis of past ground surveys on corn crops [Paloscia \(1991\)](#).

Day Of Year		159	162	166	167	186	193	200	253	256	263	279	285	291	298
Incident Angle	[deg]	30	30	30	30	30	30	30	30	30	30	30	30	30	30
Soil Property															
Moisture Content	[m ³ /m ³]	0.34	0.23	0.29	0.31	0.3	0.26	0.2	0.21	0.22	0.23	0.29	0.32	0.3	0.31
Correlation lenght	[cm]	5	5	5	5	5	5	5	5	5	5	5	5	5	5
Roughness Std	[cm]	1	1	1	1	1	1	1	1	1	1	1	1	1	1
Fresh Biomass	[kg/m ²]	0.06	0.07	0.13	0.15	2.49	3.85	5.08	5.93	5.19	6.65	7.42	7.54	7.78	7.86
Leaves Property															
Leaf Area Index**	[m ² /m ²]	0.41	0.57	0.84	0.92	2.83	3.73	4.36	4.49	4.49	4.49	4.49	4.49	4.49	4.49
Moisture Content	[kg/kg]	0.88	0.89	0.89	0.89	0.89	0.88	0.88	0.7	0.7	0.68	0.65	0.64	0.62	0.61
Sheet Lenght	[cm]	19.7	22.9	27.4	28.4	46.3	51.4	53.6	53.4	53.4	53.4	53.4	53.4	53.4	53.4
Sheet Width/Disc Diameter	[cm]	3.28	4.57	4.74	6.06	8.57	8.94	8.91	8.91	8.91	8.91	8.91	8.91	8.91	8.91
Sheet and Disc Thickness	[cm]	0.03	0.03	0.03	0.03	0.03	0.03	0.03	0.03	0.03	0.03	0.03	0.03	0.03	0.03
Stems Property															
Moisture Content	[kg/kg]	0.88	0.89	0.89	0.89	0.89	0.88	0.88	0.7	0.7	0.68	0.65	0.64	0.62	0.61
Density	[m ⁻²]	8	8	8	8	8	8	8	8	8	8	8	8	8	8
Height	[cm]	15.7	21	30	32.2	88.5	118	150	165	165	165	165	165	165	165
Outer Radius	[cm]	1.01	1.09	1.21	1.23	1.47	1.35	1.13	1.01	1.01	1.01	1.01	1.01	1.01	1.01

Table 4.1: Main observation parameters and ground data used in model simulation of the corn RASAM scatterometer data at Central Plain.

4.1.2 Matera Data Set

An experimental campaign was carried out at the Italian Matera site in 2001, over three wheat fields, denominated field 1, 2 and 3, in correspondence with ERS-2 overpasses. Field sizes range between three and ten hectares. We have considered ERS-2 SAR signatures collected on field 3, for which detailed ground truth were available, which were extracted from six standard ESA PRI products. All the images were acquired in two adjacent descending orbit tracks with 20° and 25° incidence angle. Data were calibrated and co-registered using the ESA TOOLBOX software package. The number of pixels averaged to compute the backscattering coefficient ranged between 100 and 400. In this study, ground measurements collected over a fourth field, which is very close to field 3, have been used as model inputs. Ground measurements were detailed, and covered the significant variables required by the model as inputs, as shown in Table 4.2. The maximum fresh biomass was slightly higher than 2 kg/m^2 .

In 2003, two wheat fields (called field 5 and field 6) were monitored at the same site by both Envisat ASAR and ERS-2 SAR. The data collected by the two instruments have been joined together and constitute the third data set we took into account for the following model validation. All ground variables measured during 2001 Matera campaign were also measured during 2003 campaign Wegmüller et al. (2005) and used to input the model as reported by Table 4.3 and 4.4. The 2003 season was dry, and the maximum biomass was less than 2 kg/m^2 , for both fields. When ground measurements were not collected coincidentally to SAR acquisition, on both 2001 and 2003 campaigns, the data collected on a close day were considered. This is the case for the values followed by a star in Table 4.2–4.3–4.4. Finally, we notice that the LAI values reported in the tables concerning the Matera campaigns, were not directly measured, but derived from leaf density and leaf dimensions measurements.

Day Of Year		75	94	110	129	144	164
Incident Angle	[deg]	24.5	20.5	24.5	20.5	24.5	20.5
Soil Property							
Moisture Content	[m ³ /m ³]	0.21	0.18	0.11	0.29	0.09	0.05
Correlation lenght	[cm]	6	6	6	6	6	6
Roughness Std	[cm]	1.3	1.3	1.3	1.3	1.3	1.3
Fresh Biomass	[kg/m ²]	0.23	1.07	1.37	2.4	2.2	1.56
Leaves Property							
Leaf Area Index**	[m ² /m ²]	0.57	2.28	4.07	3.15	1.77	1.87
Moisture Content	[kg/kg]	0.84	0.79	0.78	0.68	0.42	0.09
Disc Radius	[cm]	0.2	0.4	0.5	0.45*	0.4	0.4*
Disc Thickness	[cm]	0.02	0.02	0.02	0.02*	0.015	0.015*
Stems Property							
Moisture Content	[kg/kg]	0.59	0.83	0.83	0.65	0.63	0.55
Density	[m ⁻²]	693	523	512.4	601.7	418	440.
Height	[cm]	5.1	16.1	27.8	54.9*	67.4	61.6
Outer Radius	[cm]	0.09	0.15	0.18	0.21*	0.2	0.17
Inner Radius	[cm]	0.	0.	0.08	0.13	0.1	0.09
Ears Property							
Moisture Content	[kg/kg]				0.65	0.59	0.25
Lenght	[cm]				6.1	5.9	4.8
Radius	[cm]				0.21	0.39	0.48

Table 4.2: Main observation parameters and ground data used in model simulation of the wheat SAR data at Matera in the 2001 campaign. * This measurement was not carried out coincidentally to SAR acquisition, so that the value measured on a close day was considered. ** LAI was not directly measured, but derived from leaf density and leaf dimensions measurements

Day Of Year		64	99	115	134	150	169
Incident Angle	[deg]	20.5	20.5	24.5	20.5	24.5	20.5
Soil Property							
Moisture Content	[m ³ /m ³]	0.27	0.2	0.18	0.08	0.08	0.11
Correlation lenght	[cm]	24	24	24	24	24	24
Roughness Std	[cm]	0.6	0.6	0.6	0.6	0.6	0.6
Fresh Biomass	[kg/m ²]	0.27*	0.76	1.26*	1.29	1.16	0.59
Leaves Property							
Leaf Area Index**	[m ² /m ²]	0.73	3.2	4.9	5.2	4.2	1.48
Moisture	[kg/kg]	0.76*	0.73	0.71*	0.53	0.25	0.12
Disc Radius	[cm]	0.15*	0.36	0.4*	0.48	0.36	0.18
Disc Thickness	[cm]	0.03*	0.03	0.03*	0.03*	0.03	0.03
Stems Property							
Moisture Content	[kg/kg]	0.8*	0.78	0.74*	0.63	0.47	0.18
Density	[m ⁻²]	428.*	523	758*	699	703	574
Height	[cm]	5.46*	14.4	26.8*	56.6	47.8	44.9
Outer Radius	[cm]	0.16*	0.1	0.14*	0.12*	0.12	0.12
Inner Radius	[cm]	0.	0.	0.03	0.055	0.064	0.088
Ears Property							
Moisture Content	[kg/kg]				0.6	0.49	0.07
Lenght	[cm]				5.1	5.	5.3
Radius	[cm]				0.2	0.3	0.29

Table 4.3: Main observation parameters and ground data used in model simulation of the wheat SAR data at the field 5 of Matera in the 2003 campaign. *,** See notes of Table 4.2

Day Of Year		64	99	115	134	150	169
Incident Angle	[deg]	20.5	20.5	24.5	20.5	24.5	20.5
Soil Property							
Moisture Content	[m ³ /m ³]	0.29	0.24	0.24	0.12	0.12	0.098
Correlation lenght	[cm]	24	24	24	24	24	24
Roughness Std	[cm]	0.6	0.6	0.6	0.6	0.6	0.6
Fresh Biomass	[kg/m ²]	0.25*	0.42	1.02*	1.56	1.33	0.8
Leaves Property							
Leaf Area Index**	[m ² /m ²]	1	2.64	4.9	4.5	3.7	4.84
Moisture	[kg/kg]	0.7*	0.7	0.74*	0.68	0.42	0.16
Disc Radius	[cm]	0.2*	0.33	0.42*	0.44*	0.44	0.67
Disc Thickness	[cm]	0.03*	0.03	0.03*	0.03*	0.03	0.03
Stems Property							
Moisture Content	[kg/kg]	0.75*	0.76	0.77*	0.7	0.45	0.41
Density	[m ⁻²]	558.7*	564.7	752*	684	460	440.3
Height	[cm]	8.34*	8.4	20.8*	48.8*	48.8	47.5
Outer Radius	[cm]	0.1*	0.13	0.14*	0.13*	0.13	0.13
Inner Radius	[cm]	0.	0.	0.03	0.052	0.06	0.083
Ears Property							
Moisture Content	[kg/kg]				0.65	0.5	0.21
Lenght	[cm]				5.2*	5.2	4.98
Radius	[cm]				0.19*	0.35	0.39

Table 4.4: Main observation parameters and ground data used in model simulation of the wheat SAR data at the field 6 of Matera in the 2003 campaign. *,** See notes of Table 4.2

4.1.3 Loamy Data Set

In spring-summer 2003, one corn field and one wheat field were monitored at the Belgian Loamy site by both Envisat ASAR and ERS-2 SAR along 5 different orbits with incidence angles ranging from 20° to 42° . The data collected by the two instruments have been joined together. Ground measurements were detailed, and covered the significant variables required by the model as inputs [Blaes \(2005\)](#). They are reported in [Table 4.5-4.6](#) for the corn field and the wheat field, respectively. The maximum value for wheat biomass was about 4 kg/m^2 and was reached later with respect to other sites. The corn field reached a maximum fresh biomass value of about 8 kg/m^2 .

Day Of Year		142	164	177	196	212	218	234
Incident Angle	[deg]	25.8	24	33	30	25.8	20.5	24
Soil Property								
Moisture Content	[m ³ /m ³]	0.31	0.16	0.13	0.1	0.19	0.12	0.09
Correlation lenght	[cm]	2.5	2.5	2.5	2.5	2.5	2.5	2.5
Roughness Std	[cm]	1.	1.	1.	1.	1.	1.	1.
Fresh Biomass	[kg/m ²]	0.01	0.94	4.71	8.15	6.91	7.72	8.31
Leaves Property								
Leaf Area Index**	[m ² /m ²]	0.03	1.29	4.62	6.21	5.85	5.8	5.8
Moisture	[kg/kg]	0.82	0.87	0.85	0.82	0.81	0.8	0.8
Sheet Lenght	[cm]	7.47	31.16	55.52	67.45	72.44	70.26	76.23
Sheet Width/Disc Diameter	[cm]	1.35	4.07	6.37	7.22	7.92	8.1	8.55
Sheet and Disc Thickness	[cm]	0.02	0.02	0.024	0.026	0.025	0.028	0.026
Stems Property								
Moisture Content	[kg/kg]	0.82	0.94	0.93	0.88	0.82	0.81	0.82
Density	[m ⁻²]	10.2	10.2	10.2	10.2	10.2	10.2	10.2
Height	[cm]	1.7	22.44	77.8	244	256	251	261.7
Radius	[cm]	0.22	0.86	1.21	1.02	0.83	0.94	0.82

Table 4.5: Main observation parameters and ground data used in model simulation of the corn ENVISAT and ERS-2 SAR data at Loamy in the 2003 campaign

Day Of Year		85	126	142	164	177
Incident Angle	[deg]	42	30	25.8	24	33
Soil Property						
Moisture Content	[m ³ /m ³]	0.18	0.32	0.33	0.18	0.1
Correlation lenght	[cm]	7.5-20	7.5-20	7.5-20	7.5-20	7.5-20
Roughness Std	[cm]	1.8	1.8	1.8	1.8	1.8
Fresh Biomass	[kg/m ²]	0.08	1.02	2.01	2.78	3.56
Leaves Property						
Leaf Area Index**	[m ² /m ²]	0.1	1.84	2.19	2.92	2.18
Moisture	[kg/kg]	0.58	0.77	0.78	0.63	0.51
Disc Radius	[cm]	0.17	0.32	0.4	0.67	0.47
Disc Thickness	[cm]	0.023	0.023	0.023	0.023	0.023
Stems Property						
Moisture Content	[kg/kg]	0.58	0.8	0.8	0.7	0.68
Density	[m ⁻²]	260	933	645.1	396.	436.
Height	[cm]	1.	10	16.8	58.8	69.1
Outer Radius	[cm]	0.1	0.16	0.16	0.19	0.175
Inner Radius	[cm]	0	0.	0	0.	0
Ears Property						
Moisture Content	[kg/kg]				0.7	0.63
Lenght	[cm]				11.4	9.6
Radius	[cm]				0.27	0.3
Inclination	[deg]				5-25	10-50

Table 4.6: Main observation parameters and ground data used in model simulation of the wheat ENVISAT and ERS-2 SAR data at Loamy in the 2003 campaign

4.2 Simulations and comparisons

The section aims at investigating about the model accuracy. In particular the single scatterer approximations introduced in Chapter 3 will be considered. In particular, the dielectric curved sheet theory will be adopted to represent the corn leaves, while the hollow cylinder will be adopted to reproduce the hollowness of wheat stems during the ripe period.

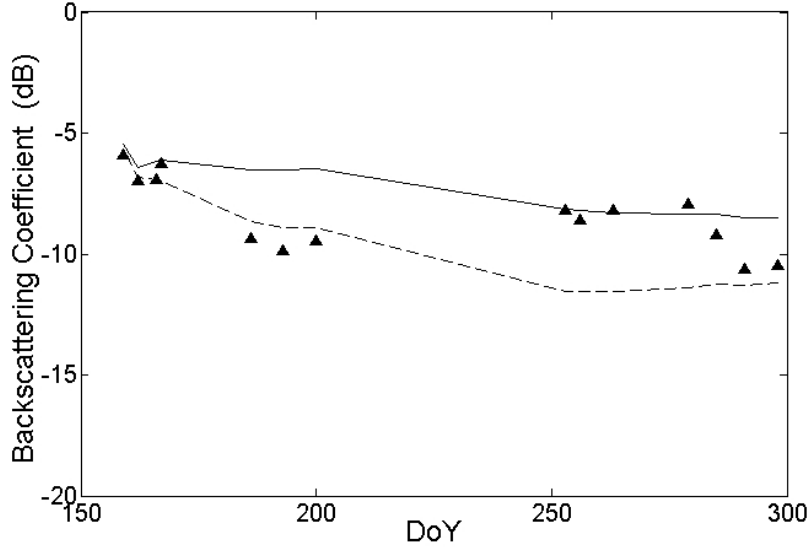
4.2.1 Corn fields

Model simulations have been compared with experimental data collected over both the corn sites described in section 4.1. For the Central Plain site, the model has been run at C-band and for an incidence angle of 30° , Figure 4.2–4.3 represent comparisons at VV, HH and HV polarizations, respectively. The simulations have been repeated by assuming the leaves subdivided into circular discs and by means of curved sheet approximation. In general, experimental data are fairly well reproduced: the sheet model leads to lower values, which reproduce better experimental data at early stage, while the disc model gives a slightly better correspondence in full growth.

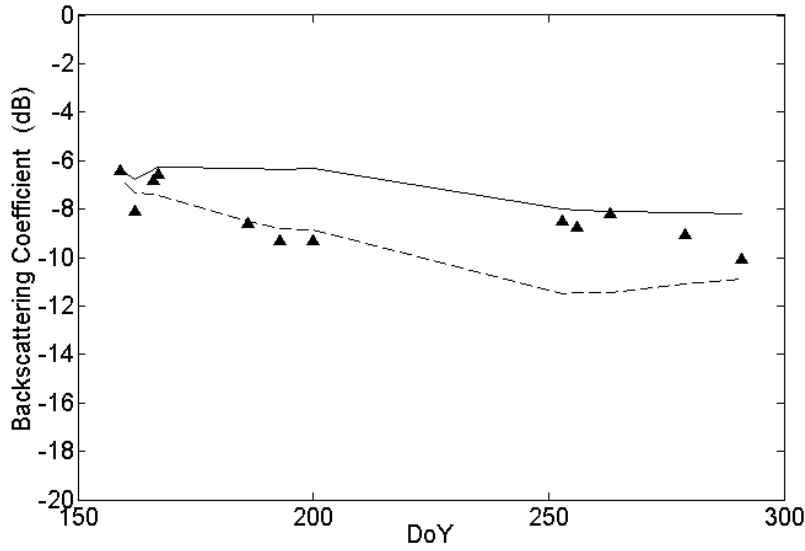
In Figure 4.4, the sheet and disc models are compared against experimental data collected at Loamy site. Here the sheet model gives the best correspondence during the whole observation interval. From an inspection of the various contributions to backscattering, it turned out that, for both data sets, soil dominates at early stage, as expected, and consequently the variations of soil moisture are reproduced. Vegetation contribution becomes dominant after days 170–180, that is when biomass gets to about $2\text{--}3\text{ kg/m}^2$, thus reducing the σ^o dynamics. In Figure 4.2–4.3 and 4.4, the disc model produces σ^o values slightly higher than the ones of the sheet model. Several factors could contribute to this effect, such as the higher number of scatterers in the case of small discs, and the sheet curvature which reduces the scatterer effective area in the backscattering direction. The above simulations have been performed calculating the vegetation permittivity by means of the model described in Ulaby and El-Rayes (1987). We have however checked that using the model developed by Mätzler (1994) slightly lower values, by about 1 dB, are obtained.

4.2.2 Wheat fields

Signatures collected at Matera site, in 2001 by ERS-2 SAR, are compared with simulation results obtained by using the “full cylinder” model and the



(a)



(b)

Figure 4.2: Comparison between corn Central Plain multitemporal σ^o 's and values simulated using disc and sheet models, at C-band and incident angle $\theta_i = 30^\circ$. (a) VV polarization; (b) HH polarization. Triangles: experimental data. Continuous line: disc model. Dashed line: sheet model.

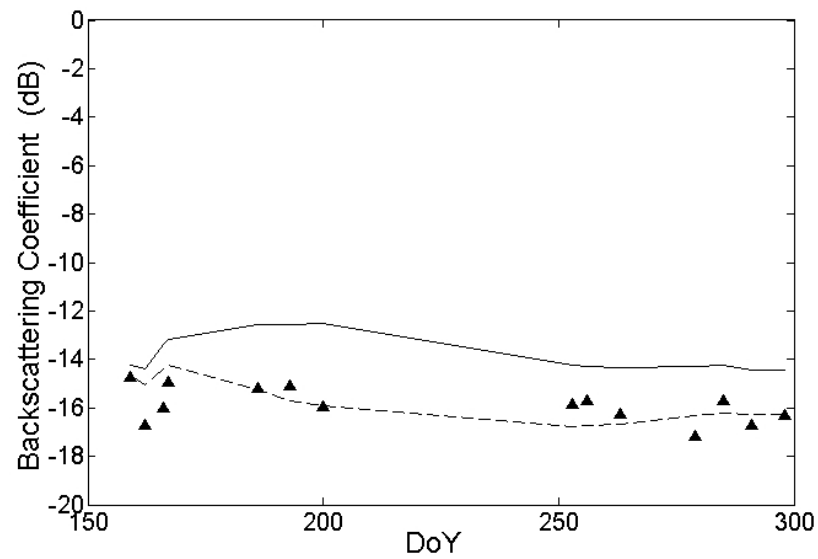


Figure 4.3: Comparison between corn Central Plain multitemporal σ^o 's and values simulated using disc and sheet models, at C-band and incident angle $\theta_i = 30^\circ$, at HV polarization. Triangles: experimental data, continuous line: disc model and dashed line: sheet model.

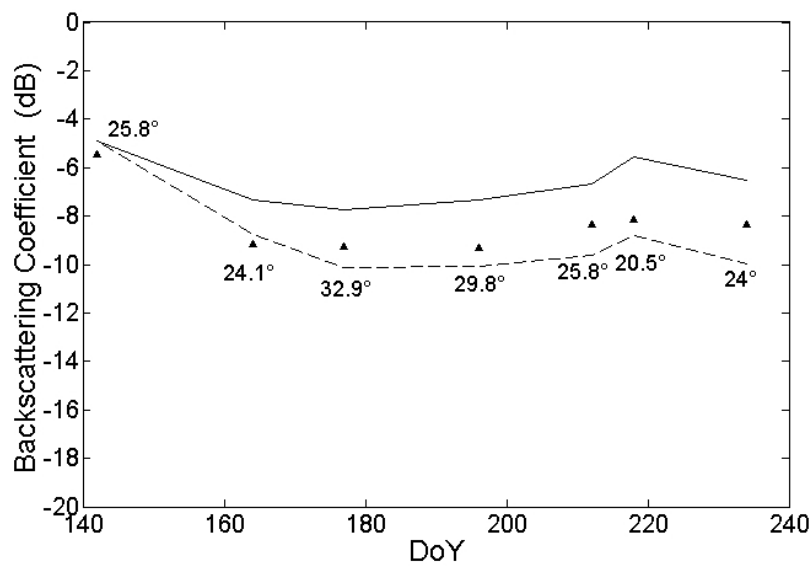


Figure 4.4: Comparison between maize multitemporal σ^o 's at Loamy site and values simulated using disc and sheet models. C-band, VV polarization - notice that backscatter values at different incidence angles are included (see Table 4.5). Triangles: experimental data. Continuous line: disc model. Dashed line: sheet model

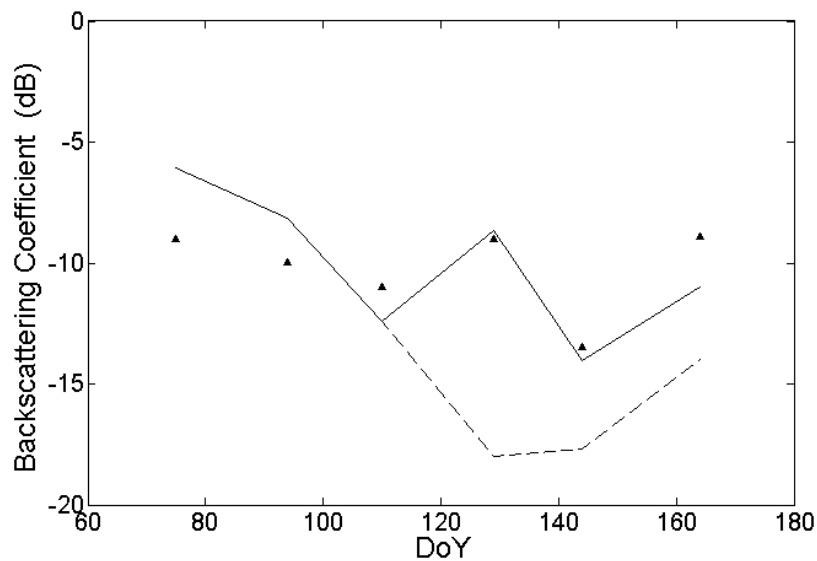
“hollow cylinder” model. From Figure 4.5(a) it is visible, as at early stage, the two models give the same results since from the weight measurements the stem inner radius is zero, that is the stem was full. In the mature stage, when the stem became hollow, the “hollow cylinder” model represents better the experimental data while the full cylinder model underestimates wheat backscattering. This is due to a strong difference in attenuation, which is lower for the case of the hollow cylinder (see figures 3.14(a)–(b)). In particular, the full cylinder model does not allow to reproduce the σ^o increase on day 129, when there was an increase of soil moisture due to rain.

Figure 4.5(b) shows the contributions of the single components, for the case of the hollow cylinder. It can be observed that in the first days, backscattering comes from the soil which shows a decreasing trend due to decreasing soil moisture content and increasing attenuation of the plants. On the last day, the soil contribution increases again, despite the soil moisture keeps on decreasing, because of the reduced attenuation introduced by the dry stems (see decreasing biomass at the end of the wheat cycle in Figure 4.1(b)). On its turn, volume contribution initially increases and then gets again lower than the ground contribution, due to vegetation drying.

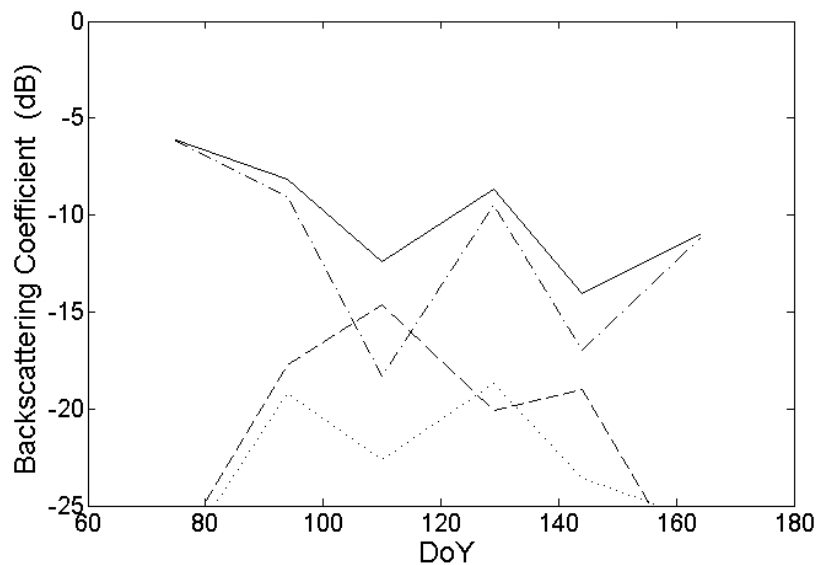
Comparisons between the signatures collected at C-band in 2003 and the simulations carried out by means of the 2 model approaches are shown in Figure 4.6(a)–(b), for field 5 and 6, respectively, of the Matera site. Here the correspondence is generally good for both fields, and it is better for the hollow cylinder, in both fields due to the lower attenuation of soil backscattering. Because of the low biomass, the backscattering is generally much influenced by soil contribution, while the vegetation contribution is significant only in the middle phase of growth.

Finally, in Figure 4.7(a) the Loamy site is considered. For this site, the stem has been modelled only by means of a full cylinder with radius equal to the measured one. Indeed, from the weight measurements it appeared that the stem of the wheat plants at Loamy was not yet hollow for the time interval of observation, since the stem inner radius resulted to be 0. In Figure 4.7(a), together with SAR data, the incidence angle at each acquisition is reported for ease of reference.

In Figure 4.7(b) the time trend of the various backscattering components can be examined. A large discrepancy between experimental data and simulations is observed on the first day, when a low σ^o was measured. At this date vegetation was almost absent, and the surface model predicts a relatively high σ^o even if the soil is quite dry and the incidence angle is large, since ground measurements indicate the soil to be rough (height std = 1.8 cm). Around day 140, vegetation biomass gets to 2 kg/m² but, since

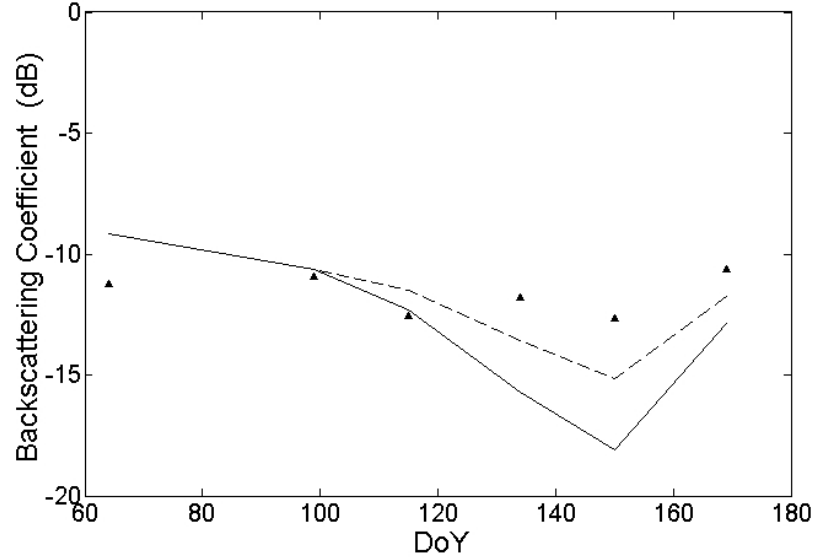


(a)

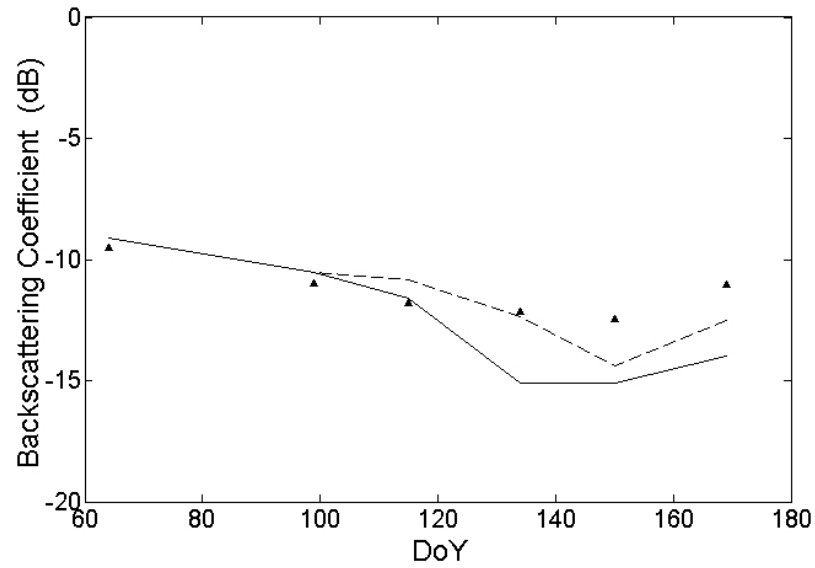


(b)

Figure 4.5: Comparison between multitemporal σ^o 's measured over a wheat field at Matera in 2001 at C-band, VV polarization. (a) SAR data (Triangles) and values simulated using full (continuous line) and hollow cylinder (dashed line) models. (b) Total backscattering (solid line), volume backscattering (dashed line), double bounce effect (dotted line), soil backscattering (dot-dashed line).

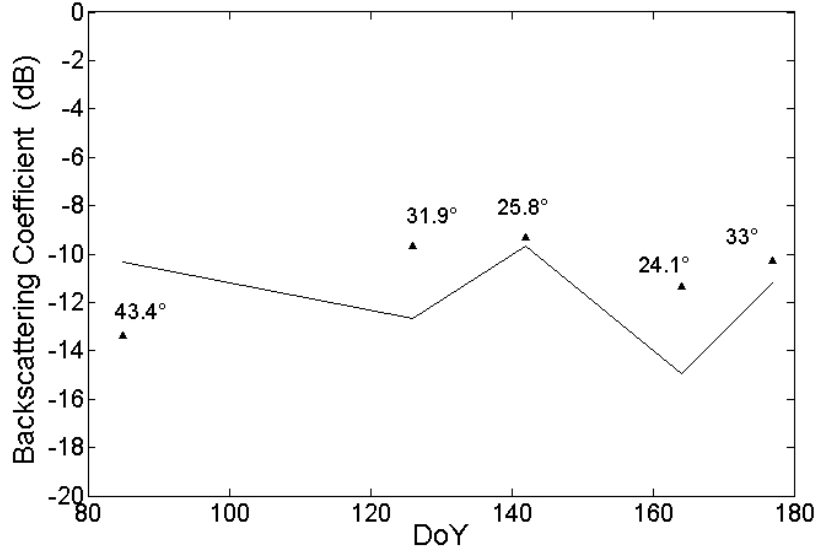


(a)

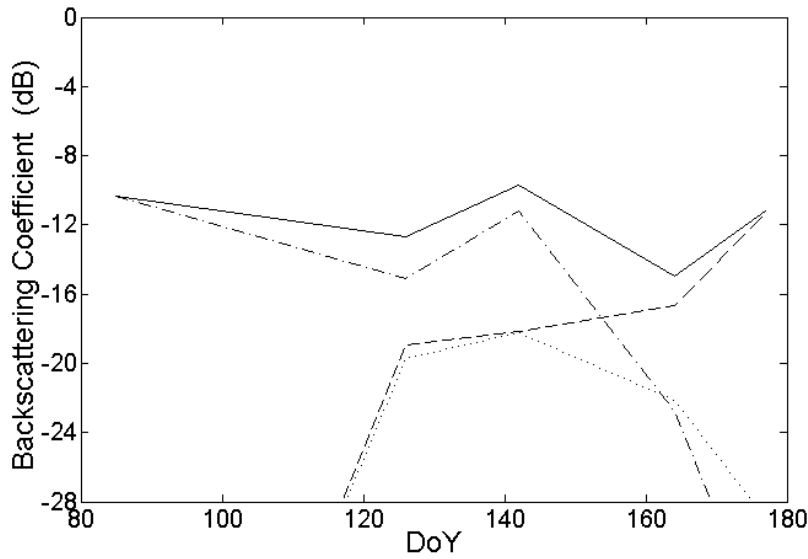


(b)

Figure 4.6: Comparison between multitemporal σ^o 's measured over wheat fields at Matera in 2003 (Triangles) and values simulated using full (Continuous line) and hollow cylinder (Dashed line) models. C-band, VV polarization. (a) Field 5; (b) Field 6.



(a)



(b)

Figure 4.7: Comparison between σ_{VV}^o 's at C-band measured by ENVISAT ASAR on the wheat field at Loamy and model simulations. (a) Triangles: experimental data. Continuous line: model simulations; (b) Total backscattering (solid line), volume backscattering (dashed line), Double bounce effect (dotted line), soil backscattering (dot-dashed line).

acquisition is made at low angle, its contribution is still low, while soil contribution is high due to the high SMC. On the last days, inclination of ears has been taken into account, as it is indicated in the ground measurements. An underestimation on the last day but one is still present, while in the last sample, σ^o showed an increase, in spite of the higher angle and the dry soil (see Table 4.6). This trend is reproduced by the model as a consequence of direct backscattering from ears and leaves, since soil backscattering becomes negligible due to the large crop biomass.

4.2.3 Accuracy Assessment and Conclusions

In this section, we quantify the accuracy of the model simulations by means of the RMS error in dB between simulated and measured backscattering coefficients. Table 4.7 shows the rms errors (dB) computed for the corn fields observed by RASAM at Central Plain and by Envisat/ERS at Loamy, in the case of the model results pertaining to the curved sheet approximation. The two data sets include all measurements collected at different angles and polarizations. Also the accuracy related to the wheat fields of Matera (both 2001 and 2003 campaigns) and Loamy is reported, with reference to the simulations performed applying the “hollow cylinder” model. The RMS errors are smaller than 2 dB, with the exception of the wheat field at Loamy.

	SITE	RMS [dB]	N. of samples
Corn Fields	Central Plain	1.44	48
	Loamy	0.96	7
Wheat Fields	Matera	1.78	20
	Loamy	2.23	5

Table 4.7: RMS errors (dB) in comparisons between simulated and experimental σ^o 's for corn and wheat fields.

In summary, the improvements on leaf and stem representation allowed to develop an electromagnetic model able to reproduce crop backscattering with reasonably low RMS. However, the ERS/ENVISAT measurements that we used for model validation show a reduced dynamic range which limits their practical application. This is due, in the case of the Loamy data sets (both corn and wheat) to the highly variable incidence angle; in the case of the Matera data sets, to the limited biomass of the wheat fields.

Chapter 5

Forests

The present chapter describes the recent improvements developments concerning the passive version of the Tor Vergata Model, in particular for forestry applications. An electromagnetic representation of litter will be provided. Moreover, in view of future space projects, a procedure has been developed to generate the input data set when only general information about forests is available.

5.1 Introduction

Several scientific and technological efforts, aimed at monitoring soil moisture by microwave spaceborne radiometers, are being done worldwide. Important projects, such as SMOS [Kerr et al. \(2001\)](#), based on L-band radiometers, are under development. For a global scale observation system, the presence of forests must be considered. Forests cover a large fraction of land, so that several pixels will be subject, totally or partially, to such a kind of cover. Only a limited number of theoretical and experimental studies have addressed the topic of emission by forests [Ferrazzoli and Guerriero \(1996\)](#); [Karam \(1997\)](#); [Pampaloni \(2004\)](#). Some important results are available, which have been summarized in [Pampaloni \(2004\)](#), but are still limited to few samples of covers and environmental conditions, especially at lower frequencies. The advantage of a theoretical approach lies in the possibility to consider the effects of several structural and environmental parameters, including soil moisture, soil roughness, presence of litter and/or understory, amount of woody and leafy biomass, geometrical structure of forest components. Also the effects of polarization and angle may be considered. Such an investigation cannot be done by using only the limited amount of experimental data

available at the present.

In the present chapter all the improvements, introduced into the passive Tor vergata Model, are described. The news introduced into the model regard two different aspects. The first one deals about the model capability to be able to represent a wide set of heterogeneous forest species. This properties is required by the world coverage foreseen with the SMOS stellite missions. The second point regards the electromagnetic representation of the litter, whose electromagnetic properties comprehension is a fundamental key for understanding the overall forest emissivity properties.

5.2 Specific Aspects for Forest Radiometry Modeling

In the passive version of the model, the overall reflectivity is first computed, and the emissivity is then obtained using the energy conservation law, introduced in §2.4. The model gives a discrete representation of the canopy, which is composed by an ensemble of single scatterers, whose electromagnetic properties are computed using suitable approximations.

The Crown of coniferous forests is composed by branches and needles. Both elements are depicted as cylindrical bodies and the infinite length approximation is used to obtain the scattering and absorption cross sections. The infinite length approximation is used also for Trunks. For a wave incoming from above, trunk scattering is strongly directed downward. Therefore, trunks are approximated to vertical absorbing cylinders in the reflectivity/emissivity computation. A simple absorbing layer is used to reproduce its behaviour. The Soil is represented as a dielectric half space with a rough interface, and its bistatic scattering coefficient is obtained by the IEM theory. The crown is subdivided into N thin sub-layers, which contain branches and needles with variable dimensions and orientation, a sketch of the geometric representation is depicted in Figure 5.1. Each layer is described by scattering and extinction matrices. The overall reflectivity is estimated by means of the Matrix Doubling Algorithm, introduced in §2.2.3. The model requires several input data, such as dimensions, orientation and permittivity of branches, trunks and needles, as well as soil and understory parameters.

Particular attention deserves the litter-understory layer, whose electromagnetic behaviour will be analyzed in §5.3. Recent studies have demonstrated that this component has an important influence on the overall forest emissivity [Della Vecchia et al. \(2006a\)](#). Furthermore, its contribution has

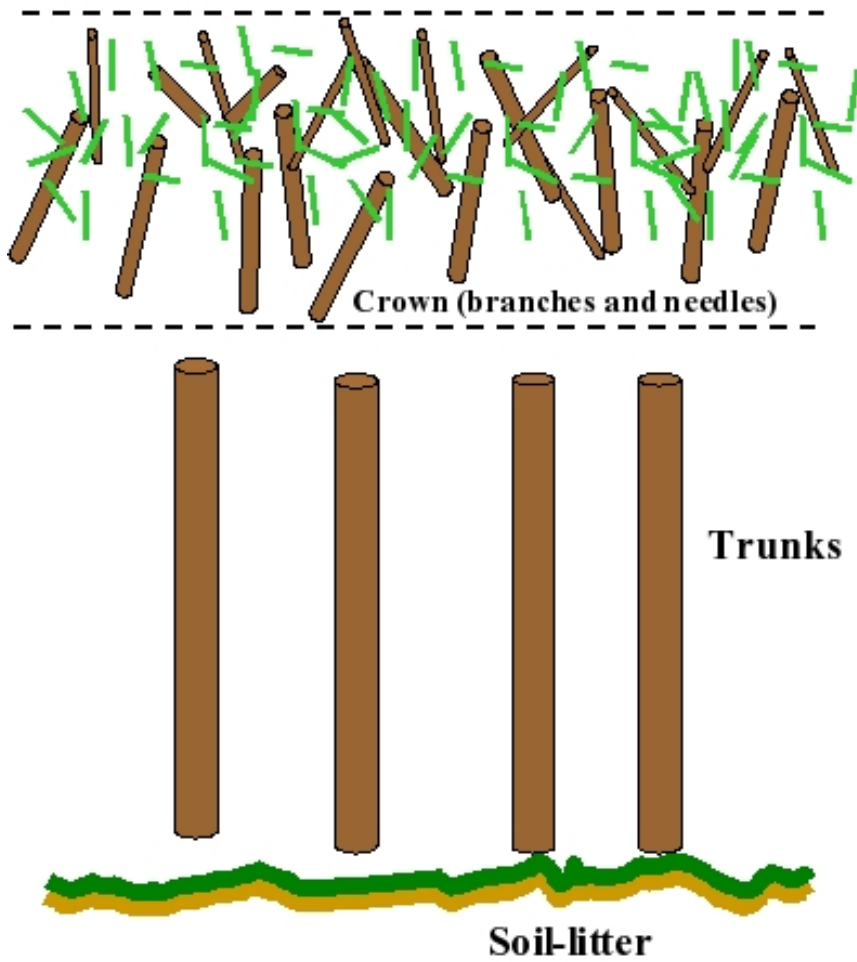


Figure 5.1: Sketch of forest model representation

been proved to be strictly correlated with the soil contribution [Grant et al. \(2006a,b\)](#).

5.3 Litter representation

In the previous model version [Ferrazzoli and Guerriero \(1996\)](#) the soil was described as a simple homogeneous half-space with a rough interface, and its permittivity was computed using the semi-empirical formula given by [Ulaby et al. \(1986\)](#). In the new version, the model has been refined in order to include litter effects. The procedure may be subdivided into various steps.

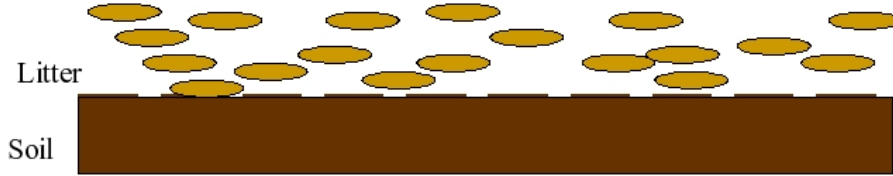


Figure 5.2: Sketch of litter model representation

First, the soil is assumed to have a flat interface, and to be overlaid by a dielectric layer, representing the litter. In this first stage, also the layer interfaces are assumed to be flat. The layer is a mixture of air and dielectric material, as depicted in [Figure 5.2](#). The dry biomass of the dielectric material $DDRY$ (kg/m^2) may be estimated by using litter-fall data available in [Cannell \(1982\)](#), and assuming two years of fall to be accumulated over the soil. This leads to the following empirical formulas, as supposed in [Della Vecchia et al. \(2006a\)](#), relating $DDRY$ to the Leaf Dry Biomass LDB (kg/m^2):

$$DDRY = \begin{cases} 1.246 \cdot LDB & \text{for Hardwood (Broadleaf) forests,} \\ 0.250 \cdot LDB & \text{for Softwood (Coniferous) forests.} \end{cases} \quad (5.1)$$

The gravimetric moisture of dielectric material DMC (kg/kg) is related to volumetric soil moisture SMC (m^3/m^3) by an empirical linear relationship based on recent measurements [Grant et al. \(2006a,b\)](#). The simple formula is:

$$DMC = \begin{cases} SMC & \text{for } 0 \leq SMC < 0.1, \\ 3.0971 \cdot SMC - 0.1817 & \text{for } 0.1 \leq SMC \leq 0.35, \\ 0.85 & \text{for } SMC > 0.35 \end{cases} \quad (5.2)$$

The correlation coefficient for this relationship is $R^2 = 0.84$.

The permittivity of the dielectric material is computed as a function of moisture, using the same empirical formula adopted for vegetation [Ulaby and El-Rayes \(1987\)](#). The thickness (TL) of the layer, which is a mixture of air and dielectric material, is related to total fresh biomass of the dielectric material DT (kg/m^2) using an empirical linear relationship derived by fitting the data published in [Putuhen and Cordery \(1996\)](#).

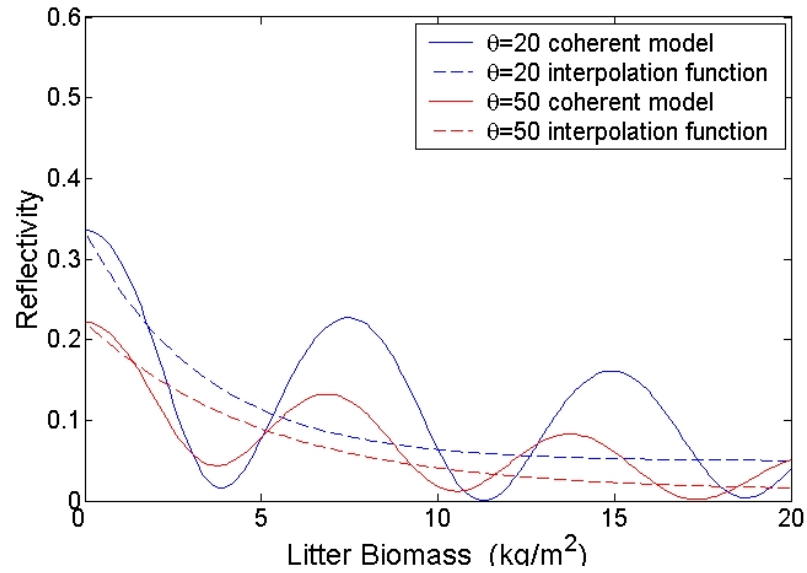
$$TL = 0.85 \cdot DT \quad (5.3)$$

where TL is in cm.

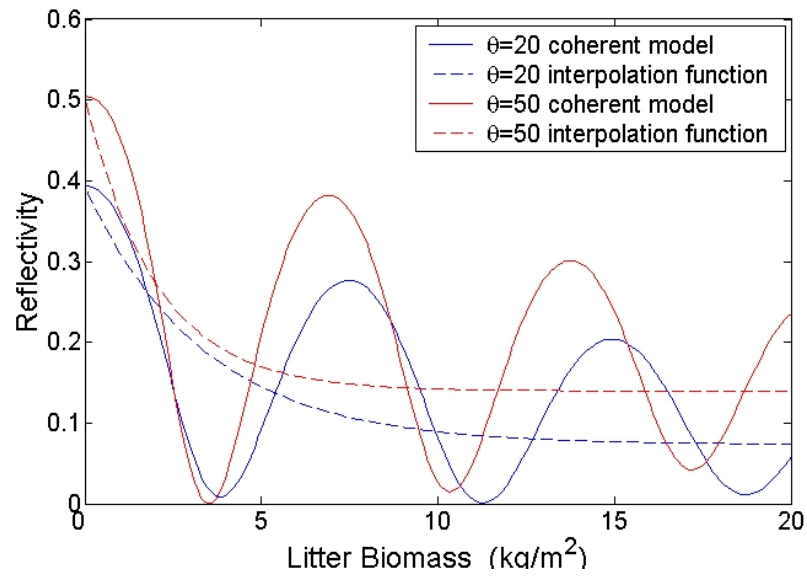
The corresponding volume fraction values, of dielectric material within the layer, are spread into the interval $[0.38-0.18]$, for litter moisture values corresponding to a range of volumetric soil moisture values of $[0.05-0.30]$. At this point the permittivity of the layer mixture is computed by means of the quadratic “refractive model” for mixtures given in [Ulaby et al. \(1986, pag. 2044\)](#). For soil permittivity, the dielectric model proposed in [Hallikainen et al. \(1985\)](#) is used.

The previously described procedure allows to evaluate the dielectric and geometrical parameters of a composite medium consisting of a dielectric half-space with a flat interface overlaid by a dielectric layer of given permittivity and thickness. At this point, the overall reflectivity of this composite medium is computed, at all required angles and at both horizontal (H) and vertical (V) polarizations, using the coherent multiple reflection model described in [Ulaby et al. \(1982\)](#). This coherent model predicts a trend of reflectivity as a function of layer thickness which is characterized by enhanced oscillations, due to coherent interactions among multiple reflected waves. In reality, this process is smoothed by the natural variations of layer thickness around its average value. In order to account for this, an averaging process is applied, making the reflectivity trend monotonic while keeping the asymptotic values. To this aim the parameters of an exponential function, giving the minimum rms difference with coherent model outputs, are estimated.

In order to clarify the procedure, we have considered the case of a flat soil with a volumetric moisture SMC equal to 20% overlaid by a litter layer of various biomass (or thickness) values. According to equation (5.1), the corresponding moisture of litter dielectric material is equal to 0.46. We have considered two angles (20° and 50°). Figure 5.3(a)–(b) shows the reflectivity as a function of litter biomass computed after the two steps of the procedure: 1) as a result of the coherent multiple reflection model; 2) after averaging to account for natural variations of layer thickness.



(a)



(b)

Figure 5.3: Simulated reflectivity of soil/litter as a function of litter biomass. Volumetric soil moisture = 20%; (a): Vertical polarization; (b) Horizontal polarization.

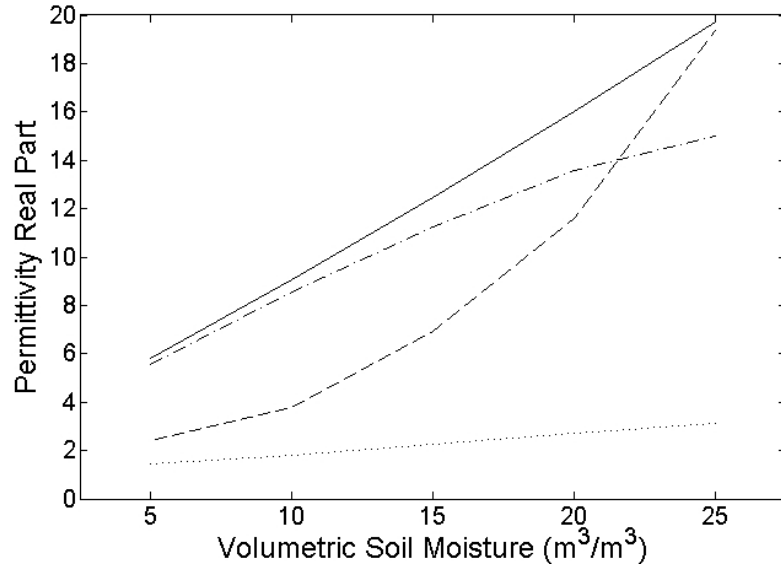
In the next step, an equivalent homogeneous half-space is considered and its permittivity is computed by minimizing a “cost function” proportional to the rms difference between the set of reflectivity values computed for the composite medium and the one computed for this homogeneous “equivalent” medium. The set is generated by applying the well established Fresnel formulas for flat half-spaces and considering all angles in the range from 0° to 60° , with a 10° step, and both polarizations. Thus, the whole soil-litter medium is reduced to a unique homogeneous half-space of given permittivity.

As an example, we have considered a soil overlaid by a litter layer with TL equal to 0.45 cm. First of all, we have estimated that the previously described reduction to a unique half-space leads to an overall rms error in reflectivity ranging from 0.01 (at the lower moistures) to 0.03 (at the higher moistures). Then, we have computed real and imaginary part of the dielectric constants obtained in the various steps, as a function of soil moisture: soil (ϵ_{rs}), dielectric material (ϵ_{rd}), litter mixture (i.e. dielectric material + air) (ϵ_{rl}) and equivalent half-space (ϵ_{re}). It is understood that the moisture of the dielectric material is related to soil moisture by equations (5.1) and (5.2). Results are shown in Figure 5.4(a)–(b) for real and imaginary parts, respectively. As expected the permittivity of the equivalent half-space is lower than soil one, and also its variations with respect to moisture are moderate. Permittivity differences between soil and equivalent half space are mostly evident in the real part, which is also the part that most influences overall reflectivity, and thus the numerical algorithm.

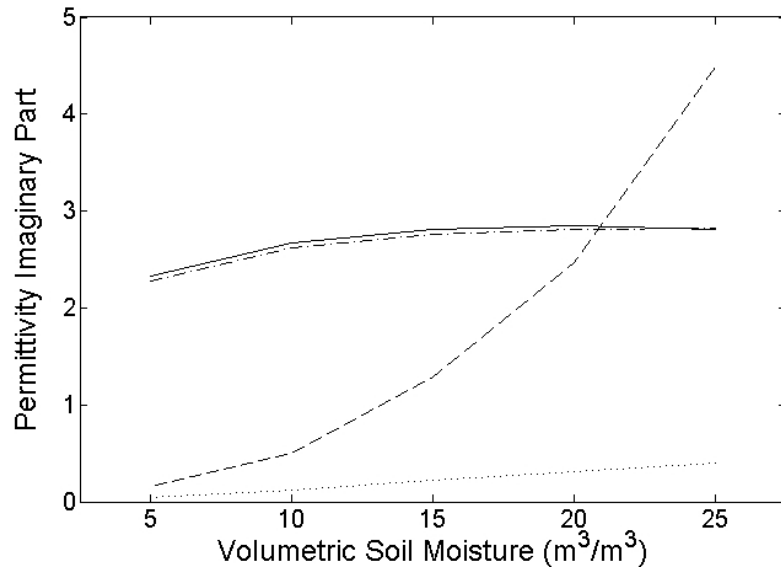
Finally, the roughness at the interface between air and the previously defined homogeneous half-space is introduced, and described by well established parameters, such as height standard deviation and correlation length. The bistatic scattering coefficient is computed by means of the Integral Equation Method Fung (1994) and is used to combine soil scattering with vegetation scattering.

5.4 Forest Structure Algorithm

In view of satellite missions such as SMOS, which will have the aim of mapping both the soil moisture and ocean salinity at world scale, becomes more and more important the possibility to develop suitable and large scale model. In this section, the approach used to adopt the Tor Vergata Model at global scale is introduced. The approach is finalized to predict the signatures of spaceborne radiometers, when only general information about ground data is available. The adopted methodology is based on allometric equations avail-



(a)



(b)

Figure 5.4: Real parts (a) and imaginary parts (b) of the dielectric constants, as a function of soil moisture: soil (ϵ_{rs}), dielectric material (ϵ_{rd}), litter mixture (ϵ_{rl}) and equivalent half-space (ϵ_{re})

able in the literature. The formulation includes also the new representation of forest litter just shown in §5.3.

Described by [Masson et al. \(2003\)](#); [Champeaux et al. \(2004\)](#), database ECOCLIMAP is a basic source, from which *LAI* (leaf area index) and forest species information is obtained. Information about density and geometry of trunks, branches and leaves is then derived. To obtain the input data required by the Tor Vergata Model (TVM) it is necessary to use also a set of allometric equations [Jenkins et al. \(2003, 2004\)](#), which link a simple parameter, such as the trunk diameter at breast height (*Dbh*), with dry biomass of the entire tree and its components: roots, branches, trunks and leaves. Some species treated in [Jenkins et al. \(2003, 2004\)](#) are typical of North America, but other ones, such as pine, fir or oak, are much more common and present in many other countries of the world. Neither information contained in [Jenkins et al. \(2003, 2004\)](#) nor ECOCLIMAP one are sufficient by themselves, but from a merge of both data sources it is possible to get a systematic description of many kinds of forests. In particular, allometric equations are used for a single tree, while *LAI* is used to estimate the number of trees per unit surface. The modelling work may be subdivided into 3 main steps, which will be described in the following:

1. Single tree description, using allometric equations for different forest kinds
2. Averaging and merging with *LAI* information, in order to provide inputs to TVM
3. Running the TVM

The following forest species are considered:

- Needleleaf
- Deciduous broadleaf
- Evergreen broadleaf, including Tropical forests
- Mixed forest
- Woodland

5.4.1 Single tree description

For a single tree belonging to a given forest species, the allometric equations of [Jenkins et al. \(2003, 2004\)](#) provide several important variables as

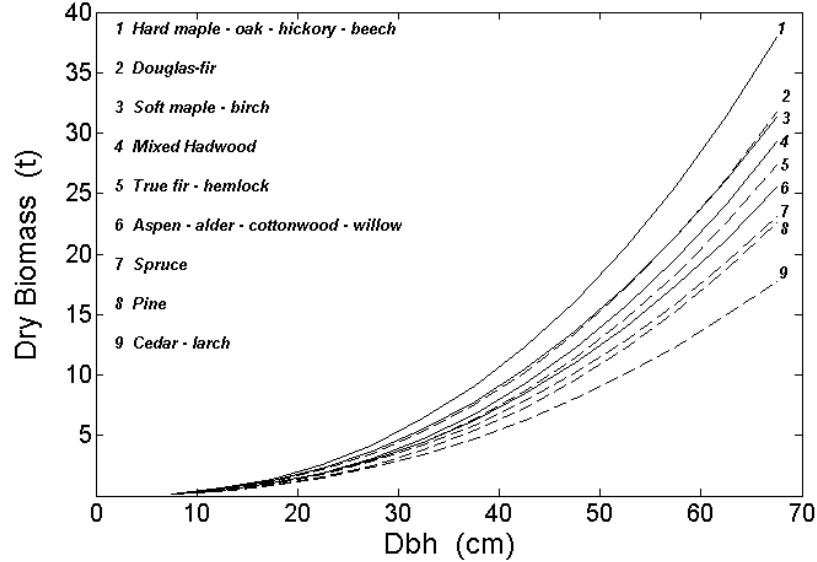


Figure 5.5: Total biomass for several kind of Softwood and Hardwood species

a function of Dbh . Figure 5.5 shows the trends of total dry biomass (in kg) for different Softwood and Hardwood species. Since the sensitivity to soil moisture variations depends strongly on total biomass, the information of Figure 5.5 is of fundamental importance. Other important information contained in Jenkins et al. (2003, 2004), regards the subdivision of total biomass. Indeed, another set of allometric equations allows us to assess how total biomass is subdivided into components.

Figure 5.6 shows the percentages, with respect to total dry biomass, of stem (trunk), branches and foliage dry biomass, for both hardwood and softwood forest typologies. The information content of Figure 5.6 is essential for TVM, because it uses a discrete approach to describe the electromagnetic interactions with single vegetation components.

However, the information contained in Jenkins et al. (2003, 2004) is not sufficient to develop a complete growth routine, because all the available data refer just to a single tree, whereas the model requires information about the entire forest, or a part of it. Indeed leaves, branches and stems densities are obtained by merging LAI information, available in ECOCLIMAP dataset, with allometric equations of Jenkins et al. (2003, 2004), as it is shown in the next Section.

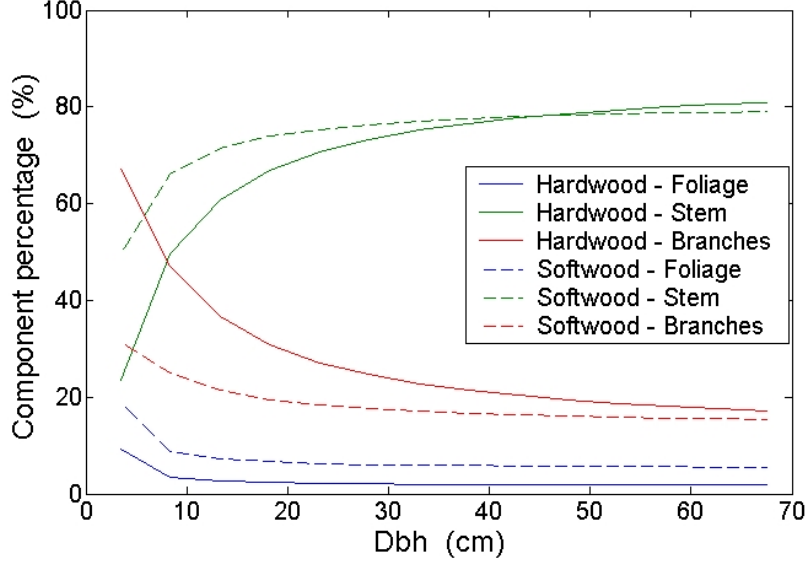


Figure 5.6: Component biomass percentages for Hardwood and Softwood species

5.4.2 Using ECOCLIMAP LAI information

The passage from “single tree” level to forest level requires two fundamental steps:

- To adopt a distribution of Dbh values within the considered forest plot
- To establish a realistic correspondence between LAI and forest density

Within an extended forest plot, assuming a single Dbh value is not realistic. Therefore, a distribution is taken, in such a way as to have:

$$N_{tr}(Dbh_i) = N_{tot} \int_{Dbh_i}^{Dbh_{i+1}} f_{N_{tr}}(Dbh_i) d(Dbh) \quad (5.4)$$

where:

- N_{tot} is the total number of trees per unit of surface [ha^{-1}]
- $f_{N_{tr}}$ is the selected distribution function for Dbh parameter
- $N_{tr}(Dbh_i)$ is the number of trees per unit of surface with diameter included in the range $Dbh_i - Dbh_{i+1}$ [ha^{-1}]

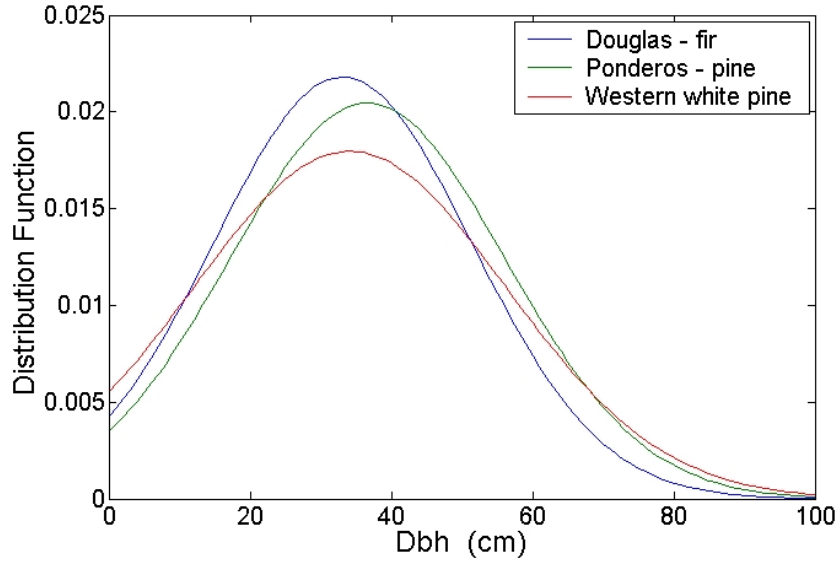


Figure 5.7: Distribution function for three coniferous species

Typical distribution functions of Dbh for coniferous forests are given in [Monserud and Marshall \(1999\)](#). Figure 5.4.2 shows the trends for three common coniferous species: Douglas-fir, Ponderosa pine and Western white pine. Other distributions are available in the literature for different species [Macelloni et al. \(2001a\)](#).

At this point, information about LAI and leaves dry biomass is used. The first step aims to link the LAI to leaves dry biomass (LDB) per unit of underlying surface. This is accomplished by fitting the measured data given in [Cannell \(1982\)](#) and depicted in Figure 5.4.2.

A linear relationship between LAI and LDB is assumed. A regression analysis gives:

$$LAI = \begin{cases} 1.49 \cdot LDB & \text{for Hardwood,} \\ 0.43 \cdot LDB & \text{for Softwood.} \end{cases} \quad (5.5)$$

By inversion of (5.5), the total forest LDB may be derived as a function of LAI . Once the forest LDB is known, a relationship with tree density may be established with the following considerations. A typical natural forest is composed of trees of different ages and dimensions, and this is represented by a distribution of Dbh . The range of Dbh values is subdivided into N

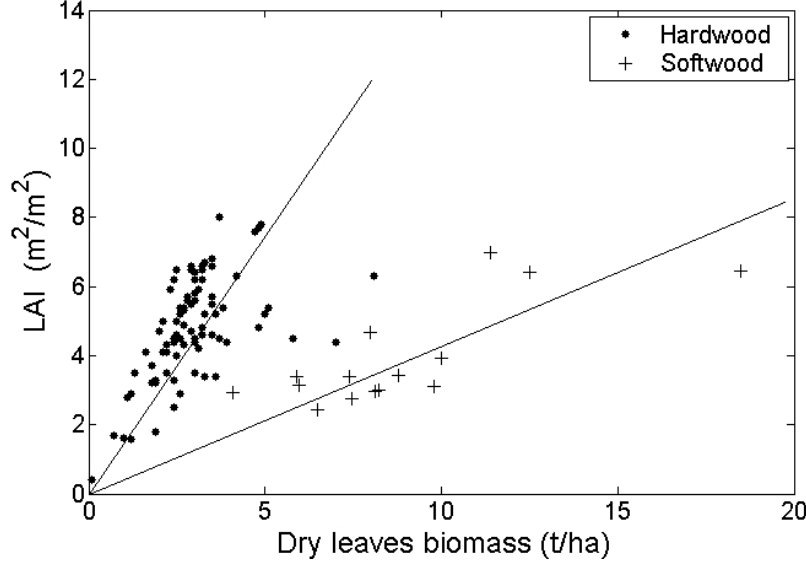


Figure 5.8: Relation between LAI values and dry leaves for Hardwood and Softwood species

discrete intervals. Therefore, the total LDB may be expressed as:

$$LDB = \sum_{i=1}^N LDB_i = \sum_{i=1}^N LDB(Dbh_i) N_{tr}(Dbh_i) = N_{tot} \sum_{i=1}^N LDB(Dbh_i) \int_{Dbh_i}^{Dbh_{i+1}} f_{N_{tr}}(Dbh_i) d(Dbh) \quad (5.6)$$

where

- LDB_i is the dry biomass (per unit of underlying surface) of leaves [t/ha], for all the trees with Dbh values within the i^{th} interval. Information about the total dry biomass of leaves for a single tree can be obtained from [Jenkins et al. \(2003, 2004\)](#),
- $LDB(Dbh_i)$ is the dry biomass [t] due to the trees with Dbh values within the i^{th} interval
- $N_{tot} \int_{Dbh_i}^{Dbh_{i+1}} f_{N_{tr}}(Dbh_i) d(Dbh)$ represents the number of trees [ha^{-1}] with Dbh within the i^{th} interval (i.e. with diameter included in the range $Dbh_i - Dbh_{i+1}$)

At this point allometric equations giving total dry biomass of single trees and component subdivision, as a function of Dbh , are used. For this scope, it is important to have the maximum yearly value of LAI , corresponding to full leaf development, and derive LDB values corresponding to it from (5.5). For a given forest species, we have Jenkins et al. (2003, 2004):

$$DB_{tot} = e^{(b_0 + b_1 \ln(Dbh))} \quad (5.7)$$

$$DB_x = DB_{tot} e^{(a_0 + \frac{a_1}{Dbh})} \quad (5.8)$$

where DB_{tot} is the total tree dry biomass, while DB_x is the component referred to leaf, stems or branches. b_0 and b_1 coefficients depend on tree species, whereas a_0 and a_1 depend also on the considered component. Using these equations for each Dbh interval, the value of $LDB(Dbh_i)$, to be used in (5.6), is computed. The same equation is then used to compute N_{tot} and, hence, absolute values of $N_{tr}(Dbh_i)$. In this way, dry biomass values for trunk, branch and leaf, may be converted from single tree values into values per unit of underlying surface. Figure 5.4.2 shows examples of biomass components, computed as a function of LAI . Pine forest data are represented with continuous lines, whereas Douglas-fir data are in dotted lines. $N_{tr}(Dbh_i)$ distributions, computed for Hardwood and Softwood forests, are shown in Figure 5.4.2.

5.4.3 Geometrical and moisture variables

The procedure described in the previous Sections gives the biomass of forest components (in [t/ha]) for each Dbh interval. Since the Tor Vergata Model needs geometrical dimensions and moistures as input, a suitable conversion procedure must be established. First of all, volumes of leaves, branches and trunks, per unit of underlying area, are computed. Since vegetation is composed by water and dry matter, we can establish, for each tree component, connections among water component, dry and fresh matter:

$$W_w = VM \cdot W \quad (5.9)$$

$$W_d = (1 - VM) \cdot W \quad (5.10)$$

hence

$$W_w = \frac{NM}{1 - VM} W_{dry} \quad (5.11)$$

where:

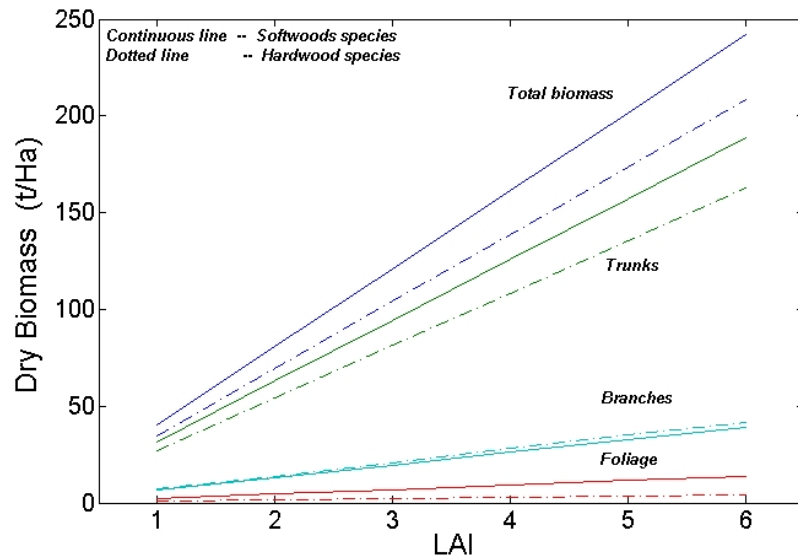


Figure 5.9: Dry biomass components as a function of LAI for Douglas-fir and Pine forests

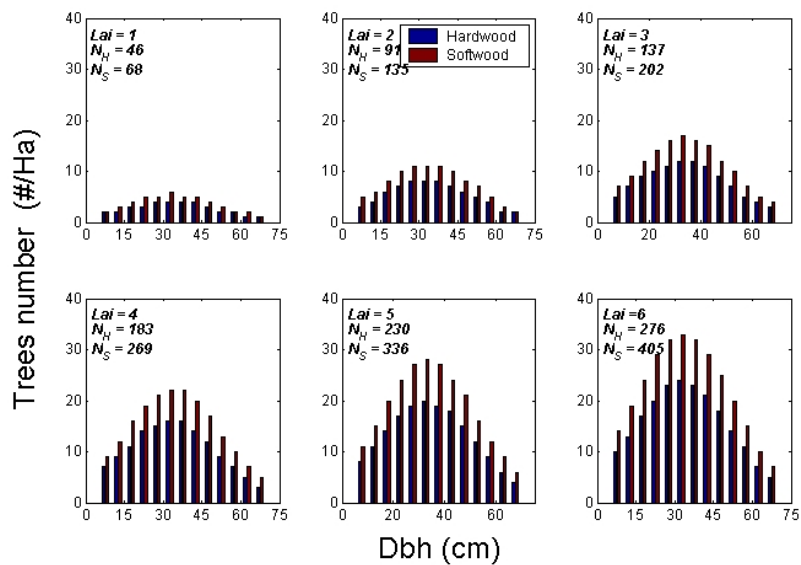


Figure 5.10: Douglas - fir and Pine numbers of trees per hectare, for different values of LAI

- VM (Vegetation moisture) is the fraction of water by weight (with respect to total fresh matter)
- W_w is the water weight [kg/m²]
- W_d is the dry matter weight [kg/m²]
- W is the fresh matter weight [kg/m²]

For each component, the volume may be computed as:

$$V = V_d + V_w = \frac{W_d}{\rho_d} + \frac{W_w}{\rho_w} = \frac{1}{\rho_d} + \frac{1}{\rho_w} \cdot \frac{VM}{1 - VM} = \left(\frac{1 - VM}{\rho_d} + \frac{VM}{\rho_w} \right) W \quad (5.12)$$

where:

- V and ρ are fresh matter volume [m³/m²] and effective density [g/cm³]
- V_w and ρ_w are water volume [m³/m²] and density [g/cm³]
- V_d and ρ_d are dry matter volume [m³/m²] and density [g/cm³]

$$W = \rho V \Rightarrow \rho = \frac{\rho_d \rho_w}{(1 - VM)\rho_w + VM\rho_d} \quad (5.13)$$

Since the dry matter is given by [Jenkins et al. \(2003, 2004\)](#), we can obtain the fresh one and then the volumes by using the previous relations and assuming VM to be known. Typical values for dry matter density are 0.3 g/cm³ for leaves and 0.4 g/cm³ for branches and trunks, whereas the corresponding typical values of vegetation moisture are 50% and 60%, respectively. Knowing the stem volume, it is possible to estimate the stem height as a function of Dbh . Results for Douglas-fir and Pine are shown in [Figure 5.4.3](#). An appreciable difference between two coniferous species is observed.

The overall branch volume may be obtained using the same procedure as for leaves, given by equations (5.9)–(5.12). A priori knowledge of VM will be supposed also in this case. The overall branch volume is subdivided into cylindrical branches of different diameters. We assume the maximum branch diameter to be equal to $Dbh/4$ for Hardwood species. For Softwood, we take the relationship between maximum branch diameter and Dbh given

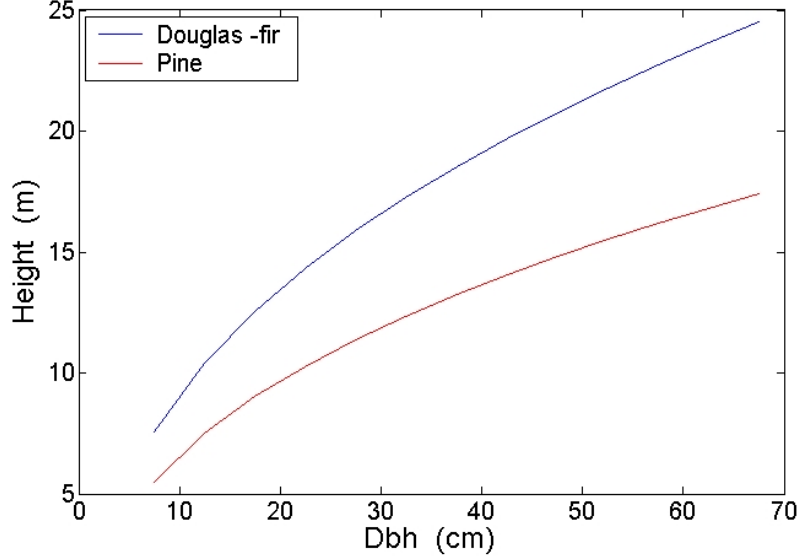


Figure 5.11: Trunks seight versus *Dbh* values

in [Kasischke et al. \(1994\)](#). The following function is adopted to reproduce the branches diameter distribution in [Saleh et al. \(2005\)](#):

$$P(\beta) = A \cos^n \left(\frac{\pi}{2} \frac{\beta - \beta_m}{\beta_0 - \beta_m} \right) \quad \beta_1 \leq \beta \leq \beta_2 \quad (5.14)$$

- $P(\beta)$ represents the density of probability of a random variable to be equal to $\tilde{\beta}$
- β_m is the value of the random variable with highest probability of occurrence
- β_0 is the value of the random variable with the lowest probability of occurrence
- β_1 and β_2 define the function range.

The relative volume of branches within a diameter range is obtained by integrating the fit function (5.14) between two diameters, with the appropriate model parameters. Figure 5.4.3 represents the branch diameter distribution functions for several *Dbh* values. In order to reproduce the natural curvature of branches, all branches are subdivided into elements 25 cm

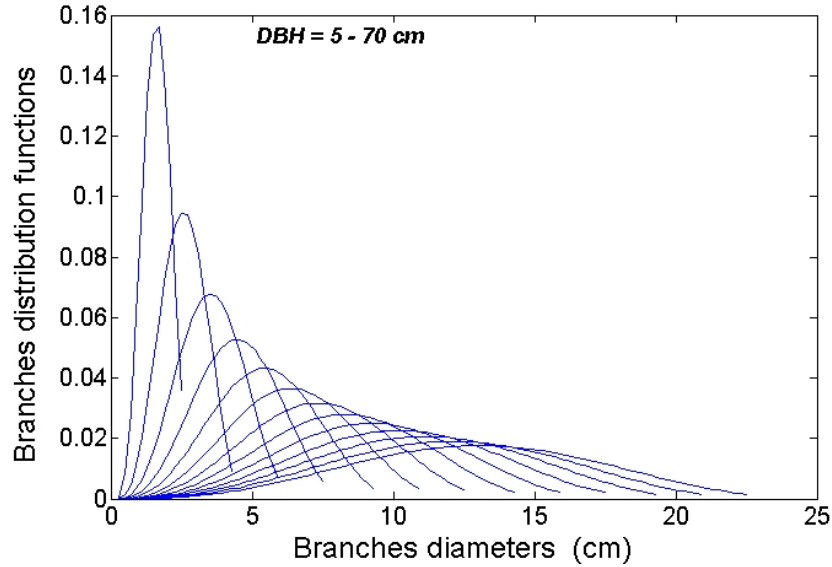


Figure 5.12: Diameter Branches distribution for Pine and Douglas-fir

long, similarly to the approach adopted in [Saleh et al. \(2005\)](#). For the time being, a random branch orientation distribution is adopted. This will be kept for smaller branches. Other distributions will be considered for larger branches and the effect on the overall emissivity will be evaluated.

As far as leaves are concerned, the model uses as input LAI and geometrical parameters, i.e. radius and thickness for broadleaf, radius and length for needleleaf. These parameters are available in [Saleh et al. \(2005\)](#); [Chauhan et al. \(1991\)](#); [Ranson et al. \(1997\)](#) for various species. In order to include leaf effects, a monthly sampling of *LAI* should be sufficient.

5.5 Parametric Analysis

As a summary of previous description, the overall emissivity simulation algorithm is structured as indicated below

1. Input

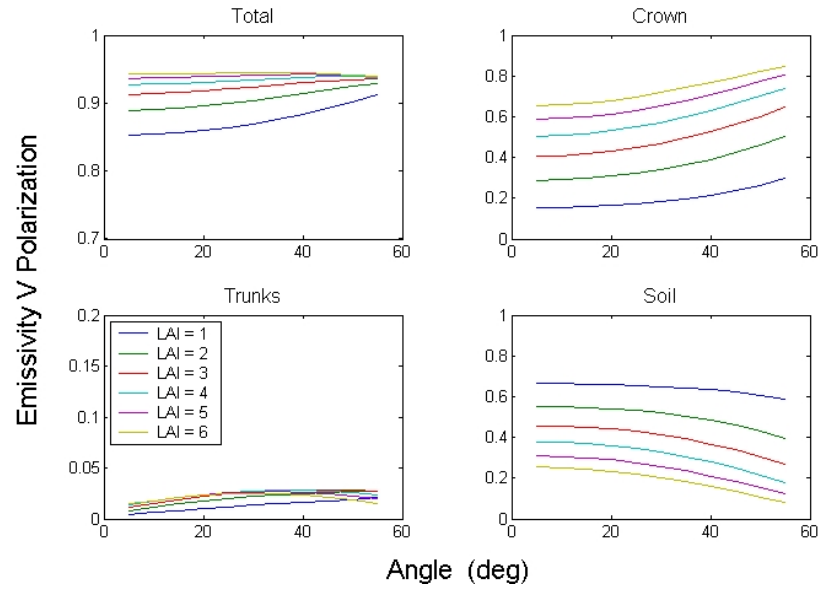
- Soil parameters
- Forest main category
- *LAI*

- Leaf (needle) dimensions
 - Gravimetric moisture of trunks, branches, leaves
 - Dry matter density of trunks, branches, leaves
2. For each Dbh value
 - Compute $LDB(Dbh_i)$ and N_{tot} as a function of LAI using equations (5.4)–(5.6)
 - Compute trunk volume per unit area and trunk dimensions using (5.7)–(5.12) for trunks
 - Compute branch volume per unit area using (5.7)–(5.12) for branches
 - Establish maximum branch diameter as a function of Dbh and apply branch diameter distribution of Figure 5.4.3
 - Compute leaf volume per unit area using (5.7)–(5.12) for leaves
 - Use information about leaf dimensions and compute number of leaves per area
 - Using TVM, compute scattering and absorption of all forest elements of the considered Dbh category
 3. The single contributions from all Dbh categories are combined and the overall scatter matrix of standing vegetation is computed.

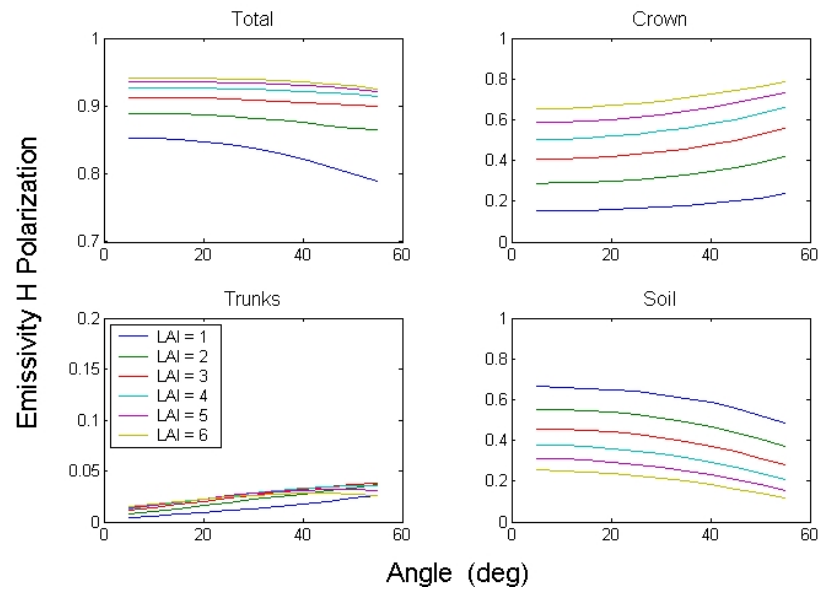
In this section, simulation results are reported. For soil, height standard deviation and correlation length have been assumed to be equal to 1.5 cm and 5 cm, respectively. Simulations have been made at L band (1.4 GHz) and for V and H polarizations. Single emissivity and transmissivity components are also reported.

5.5.1 Softwood

Figure 5.13(a)–(b) show overall emissivity and single components trends vs. observation angle at V and H polarization, with a Volumetric Soil Moisture Content (SMC) equal to 10%. Litter effects are here included in soil contribution. Figures show a low contribution from trunks, although they contain most of the biomass. The same trends, but for a SMC equal to 20%, are given in Figure 5.14(a)–(b). In order to describe completely the effects of single forest components, also transmissivity values are represented in Figure 5.15(a)–(b). A stronger contribution to attenuation comes from branches, a weak contribution comes from needles and trunks contribution

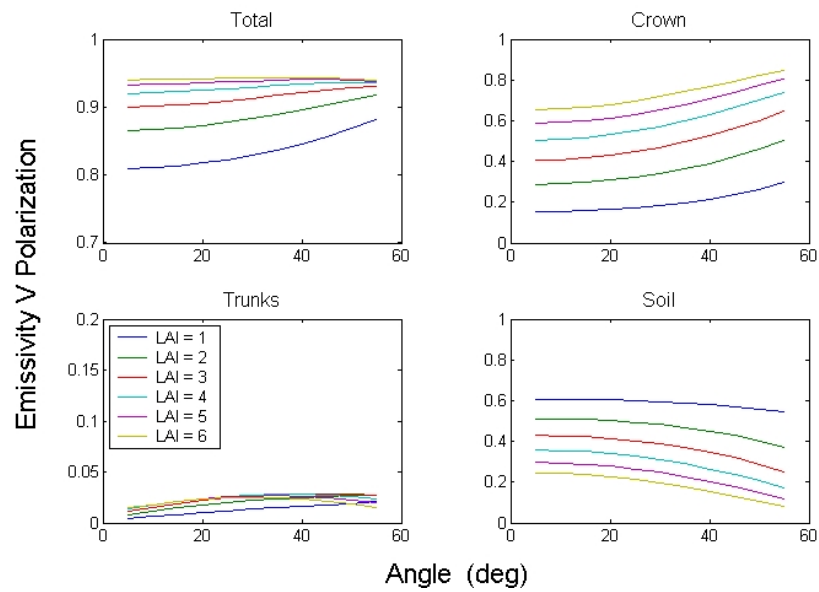


(a)

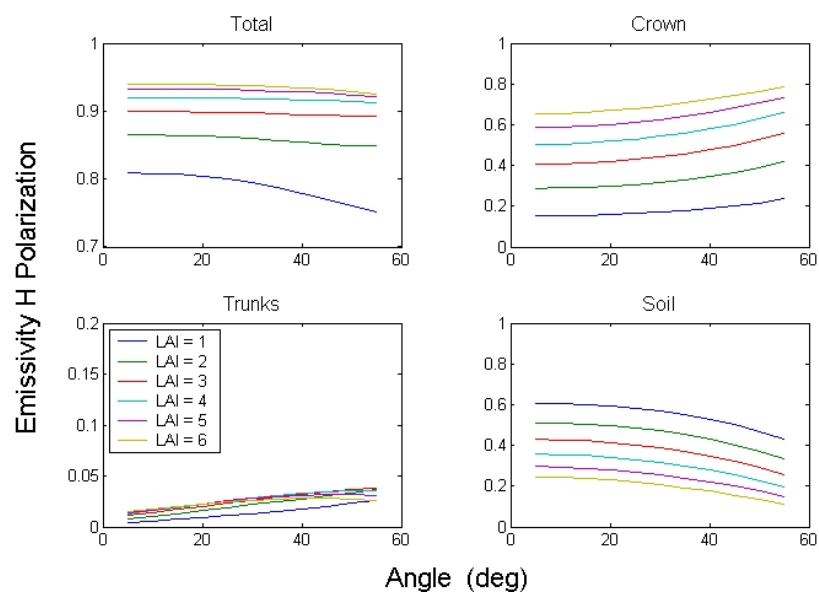


(b)

Figure 5.13: Emissivity vs observation angle for a SMC=10%; (a) : V polarization; (b) : H polarization.

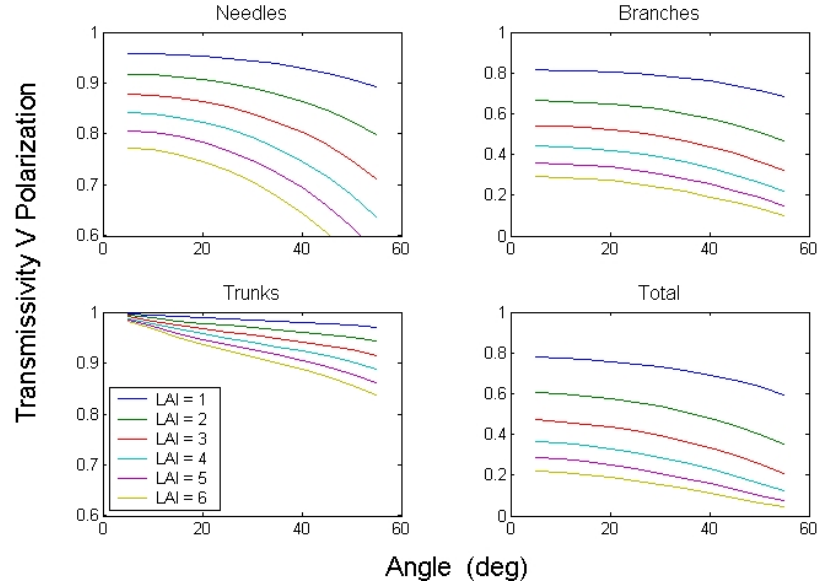


(a)

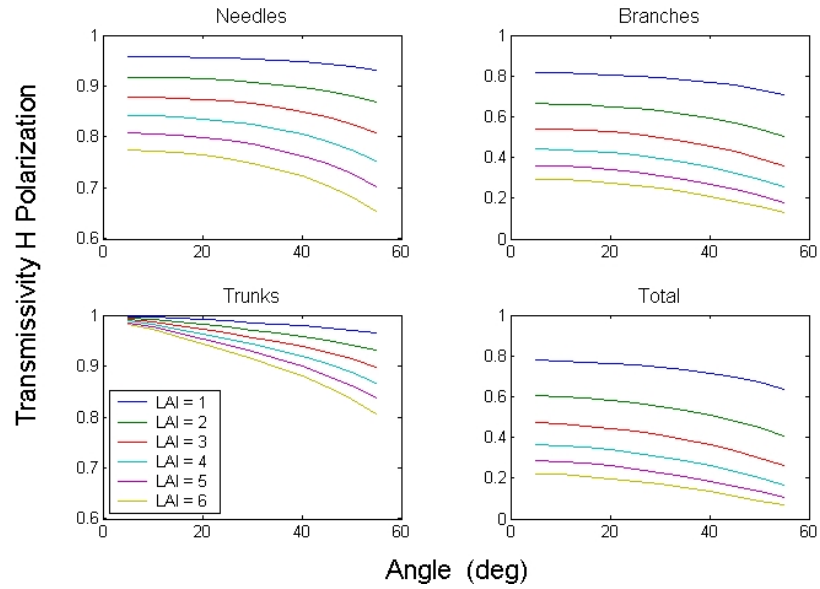


(b)

Figure 5.14: Emissivity vs observation angle for a SMC=20%; (a) : V polarization; (b) : H polarization.



(a)



(b)

Figure 5.15: Transmissivity vs observation angle; (a) : V polarization; (b) : H polarization.

is even lower (i.e. trunk transmissivity is close to the unity). Figure 5.16(a)–(b) allow to estimate the sensitivity with respect to soil moisture variations, which is a key issue for SMOS. The emissivity trends as a function of SMC are reported for angles of 25° and 45° , respectively. In the figures, upper plots show emissivity computed without including litter, while lower plots consider litter. As expected, the sensitivity is better for smaller angles, due to the lower value of attenuation. In absence of litter, some sensitivity is observed also at higher angles and for high values of LAI. However, this sensitivity disappears in presence of litter.

5.5.2 Hardwood

Results obtained for Hardwood forests are here shown. Figure 5.18(a)–(b) show overall emissivity and single components trends vs. observation angle at V and H polarization, with a Volumetric Soil Moisture Content (SMC) equal to 10%. Litter effects are here included in soil contribution. Figures show a low contribution from trunks, although they contain most of the biomass. The same trends, but for a SMC equal to 20%, are given in Figure 5.19(a)–(b). Similarly to the Needleleaf forest case, contribution from trunks is low. In order to describe completely the effects of single forest components, also transmissivities are represented in Figure 5.20(a)–(b). Figure 5.21(a)–(b) represent the sensitivity to soil moisture variations. The emissivity trends as a function of SMC are reported for angles of 25° and 45° , respectively. In the figures, upper plots show emissivity computed without including litter, while lower plots consider litter. Similarly to Needleleaf case, some sensitivity is observed also at 45° and for the higher values of LAI, but only if litter is not included.

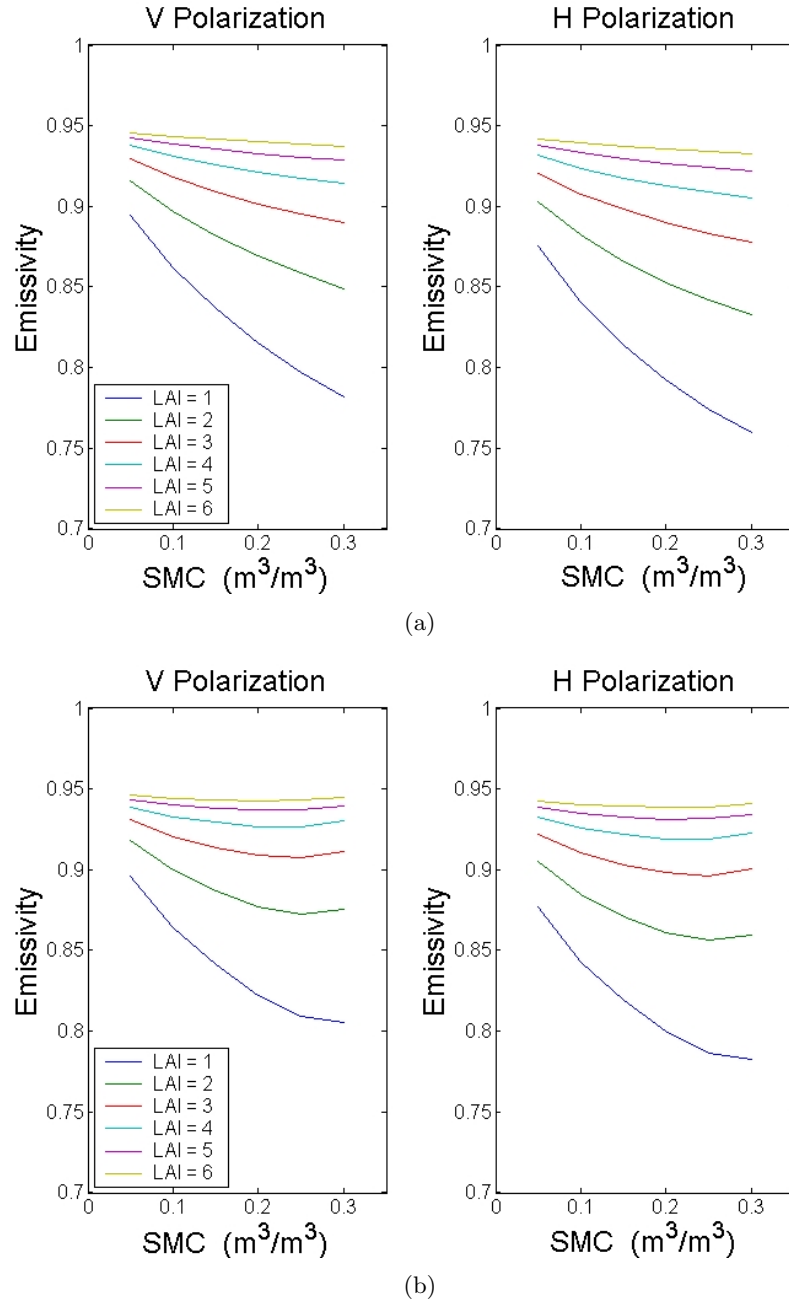


Figure 5.16: Emissivity vs SMC for $\theta = 25^\circ$; (a) : without litter; (b) : with litter.

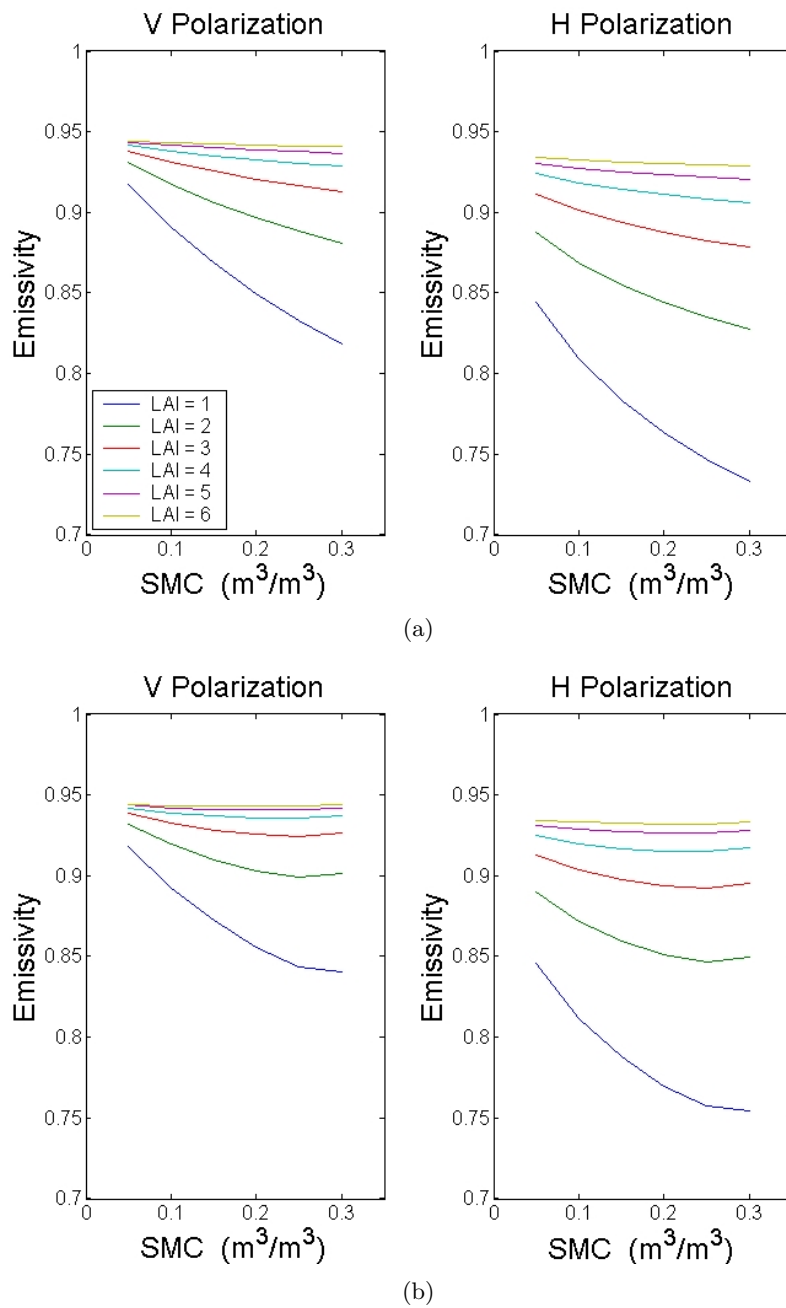
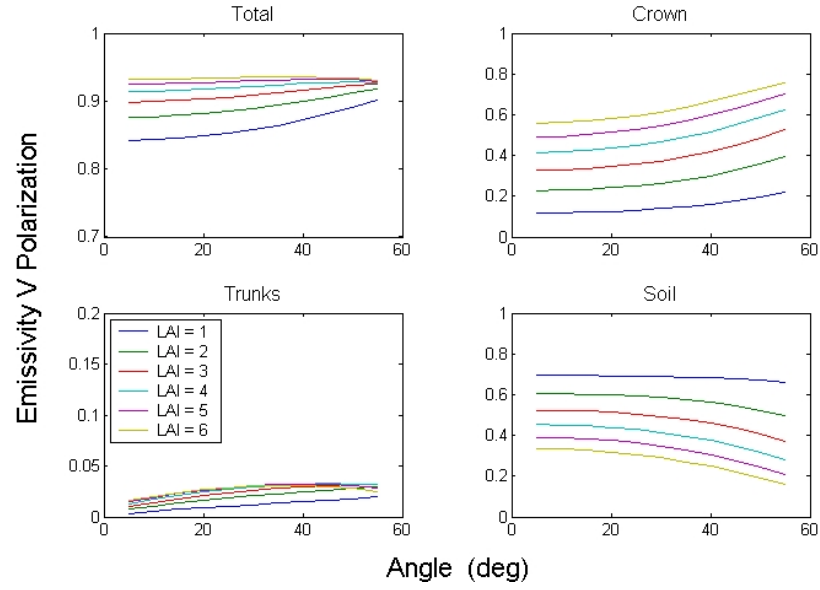
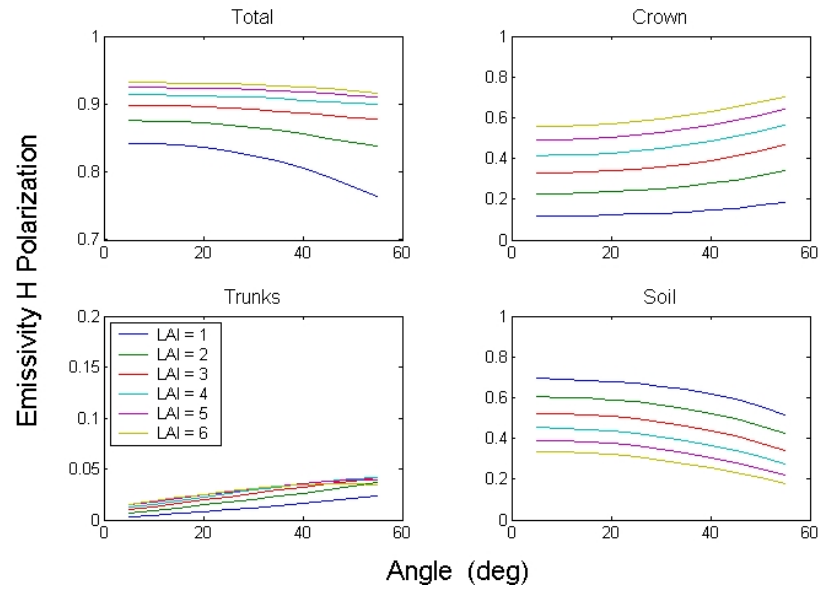


Figure 5.17: Emissivity vs SMC for $\theta = 45^\circ$; (a) : without litter; (b) : with litter.

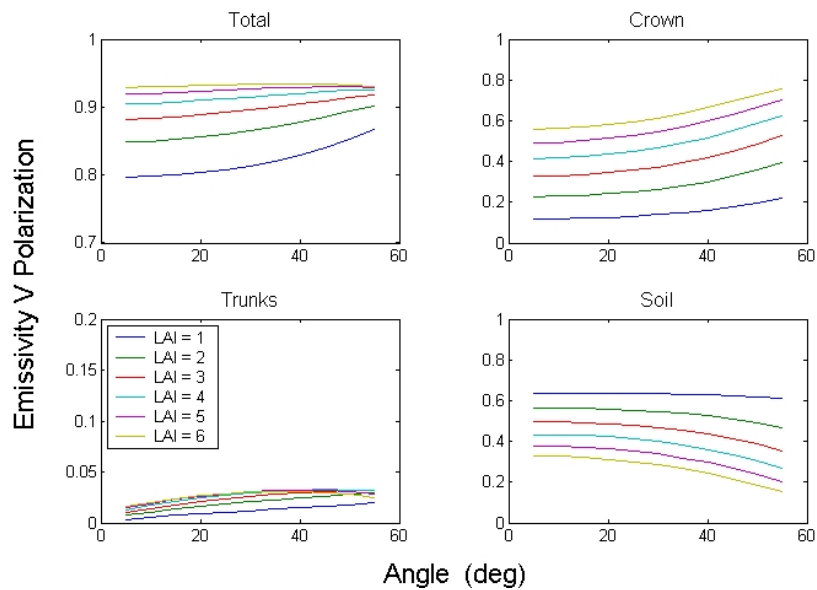


(a)

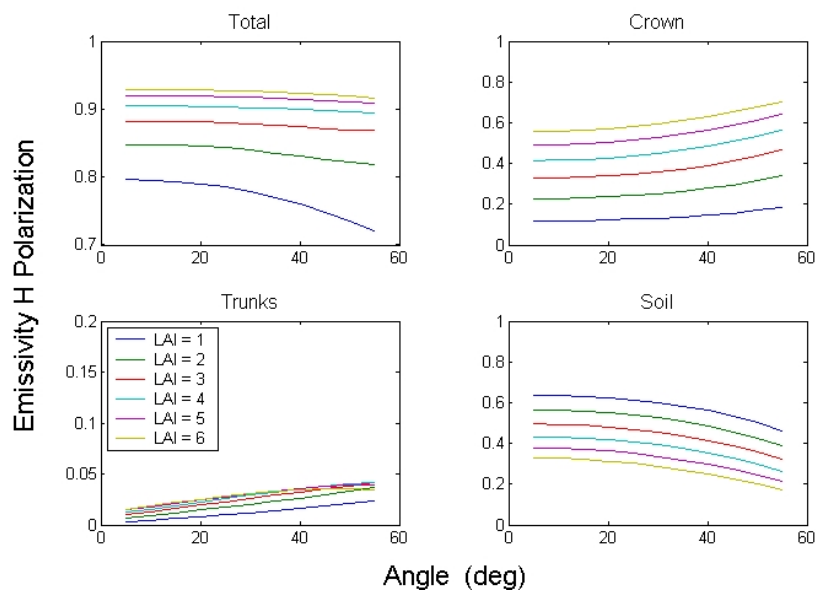


(b)

Figure 5.18: Emissivity vs observation angle for a SMC=10%; (a) : V polarization; (b) : H polarization.

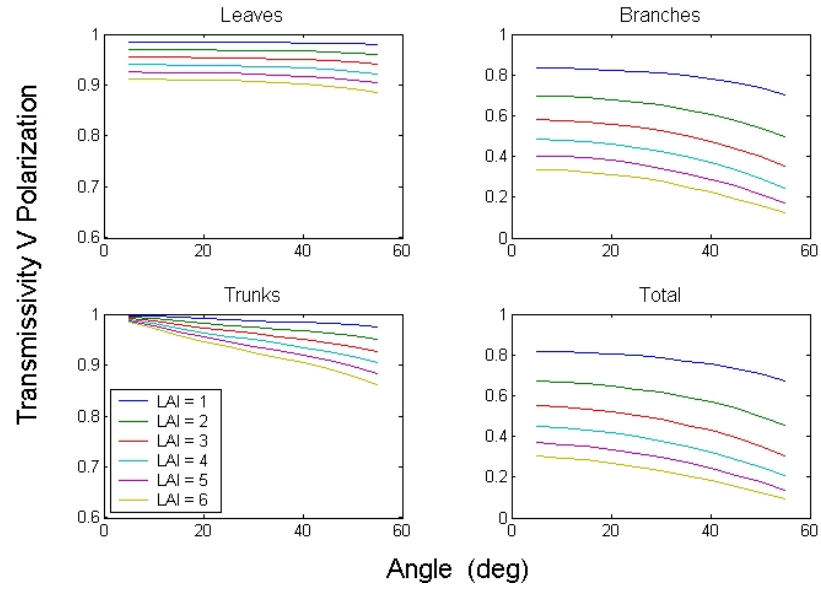


(a)

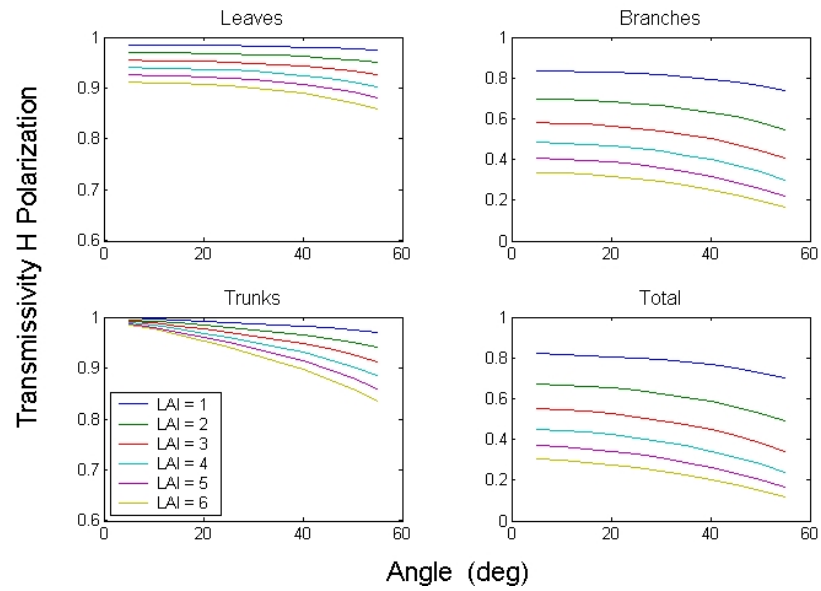


(b)

Figure 5.19: Emissivity vs observation angle for a SMC=20%; (a) : V polarization; (b) : H polarization.



(a)



(b)

Figure 5.20: Transmissivity vs observation angle; (a) : V polarization; (b) : H polarization.

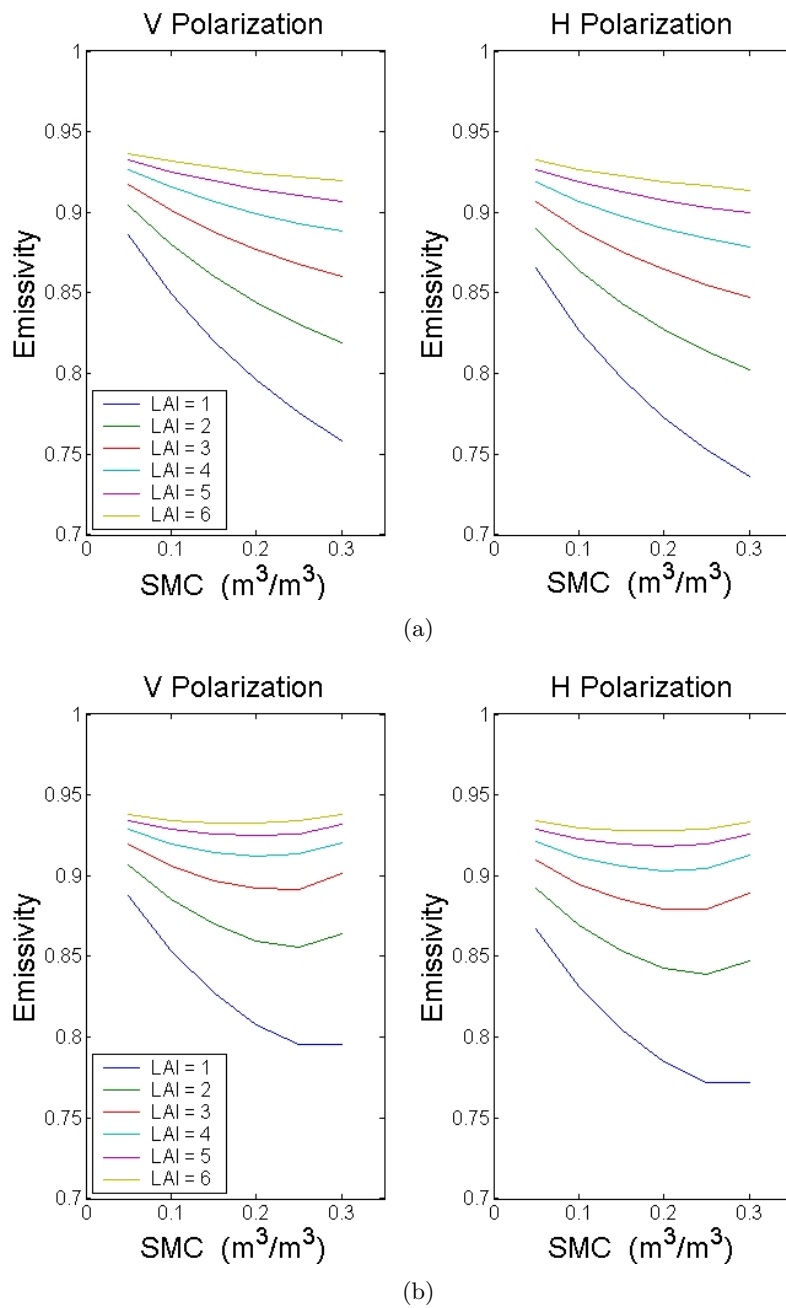


Figure 5.21: Emissivity vs SMC for $\theta = 25^\circ$; (a) : without litter; (b) : with litter.

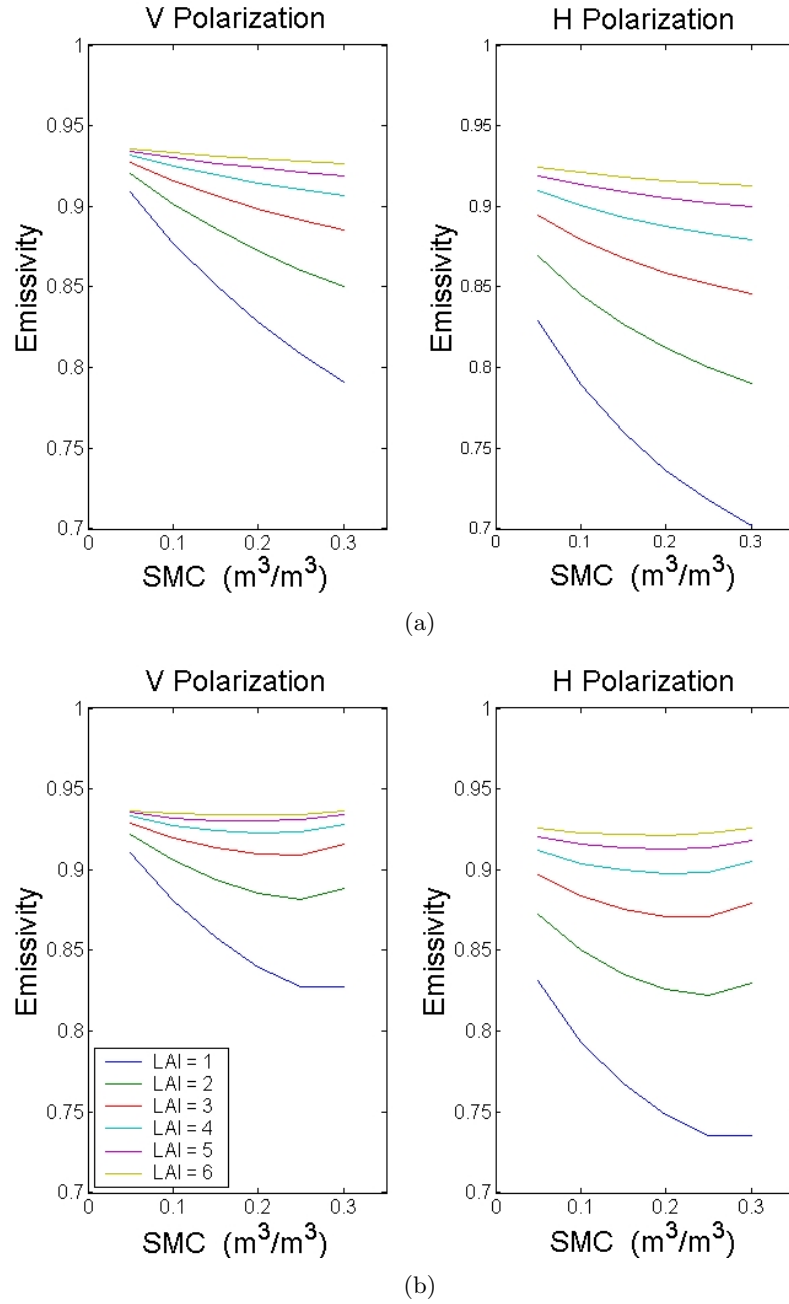


Figure 5.22: Emissivity vs SMC for $\theta = 45^\circ$; (a) : without litter; (b) : with litter.

Chapter 6

Forests Model Validation

The present chapter shows and discuss some comparisons between experimental emissivity data, collected in the framework of several campaigns, and simulations obtained by Tor Vergata Model described in Chapter 5. The campaign involves either Softwood and Hardwood forest species.

6.1 EuroSTARRS

The EuroSTARRS campaign is an experimental activity carried out in view of SMOS satellite mission. The airborne platform was equipped with an L-band (1.4 GHz) radiometer and it was able to measure brightness temperature at nominally vertical polarization at several angles in the range 5° – 50° Saleh et al. (2004). The flights took place between 17th and 23th of November 2001, and covered various kinds of surface such as bare soil, agricultural fields, coniferous and deciduous forests. The surface considered here includes the coniferous woods of Nezer, into Les Landes forest, where a large number of stands with different biomass are present. Simultaneously to airborne observations, volumetric soil moisture (*VSM*) was measured at stands of different ages. Values were close to $0.10 \text{ [m}^3/\text{m}^3]$ for 5 year-old stands, while were close to $0.15 \text{ [m}^3/\text{m}^3]$ for stands older than 20 years. Forest understory was very heterogeneous, mostly made of grass, shrubs, needles and dry ferns. Detailed measurements of its biophysical and geometrical properties are not available. Surface emissivity (e) was computed from measured brightness temperature (T_b) from STARRS, two-channel infrared temperature T_{ir} obtained concurrently to flights, and estimations of the downward sky brightness temperature T_{sky} , by the following equation $e = (T_b - T_{sky}) / (T_{ir} - T_{sky})$ Saleh et al. (2004). T_{ir} was measured at 12° only,

while a time interpolated value was assigned to all the angular observations for a given time t .

The forest was homogeneous, and the gradients in the canopy and in the soil-vegetation interface at morning (and rather cloudy conditions) were low. The rms error in surface temperature estimate by means of T_{ir} was evaluated to be under 2 K, and the error in T_{sky} estimation is about 1 K. Other inaccuracy sources may be due to integration within antenna main lobe, sidelobes and polarization mixing. Over Les Landes site, these problems were reduced by the low slope of the angular trends. Moreover, the aircraft pitch angle was always lower than 3° , and the roll angle had a standard deviation of less than 1° . The overall inaccuracy due to these errors was estimated to be about 1 K [Saleh et al. \(2004\)](#).

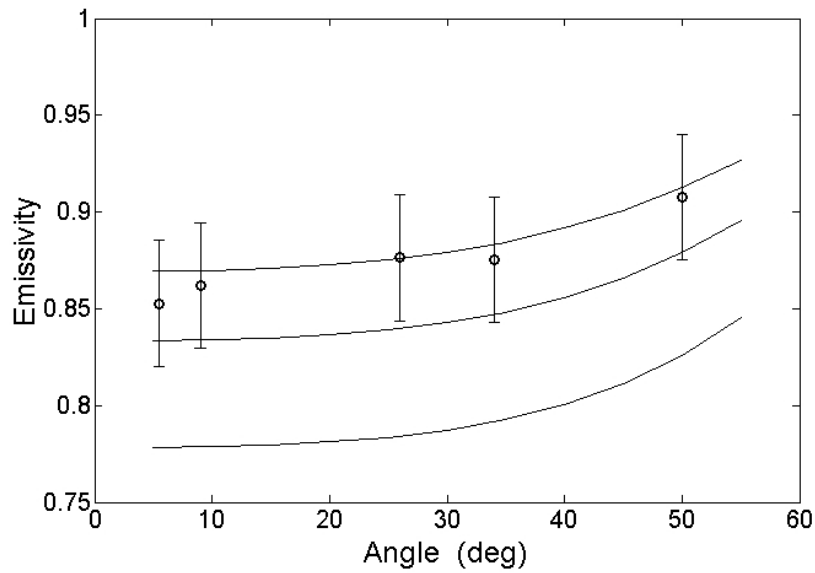
Comparison with Experimental Data

Emissivity values simulated by the model have been compared with values measured during the EuroSTARRS campaign over stands of the same age (i.e. 5, 26 and 32 years old). Detailed information about forest geometry and biophysical properties described in [Saleh et al. \(2005\)](#), as well as measured values of soil moisture, have been used as model inputs [Della Vecchia et al. \(2006d\)](#).

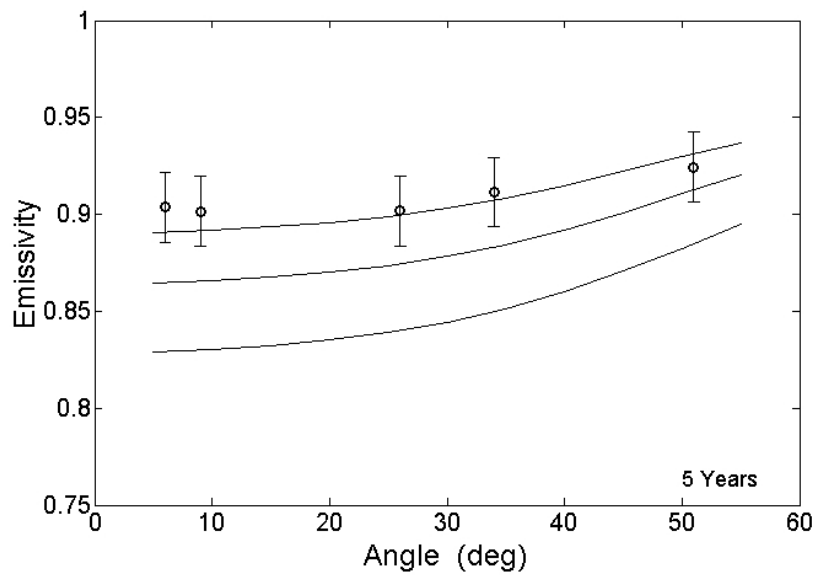
Unfortunately, detailed information about soil roughness and understory-litter vegetation was missing. Anyhow, since our objective was to investigate the effects of the coniferous tree components, we have followed the procedure indicated below.

- First of all, emissivity values measured over stands of very low age (2 years) have been taken as a reference for the background soil emission. The effects of arboreous vegetation are assumed to be very low over these stands. We have compared the measured emissivities with values simulated for bare soils with VSM equal to $0.10 \text{ [m}^3/\text{m}^3]$ and understory-litter optical depth τ equal to 0, 0.1 and 0.2, represented by means of an absorbing dielectric layer.
- Then, for forests 5, 26 and 32 years old, simulations have been made by considering the same soil roughness and the same values of understory-litter optical depth as above. Measured values of VSM have been used.

Figure [6.1\(a\)](#) shows trends of measured emissivity vs. observation angle for 2 year-old stands (error bars), and simulations obtained with a soil sur-

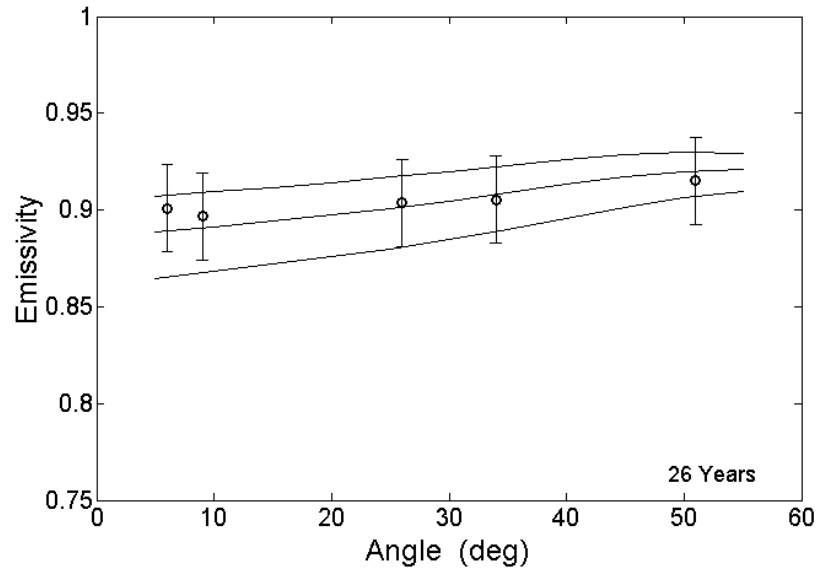


(a)

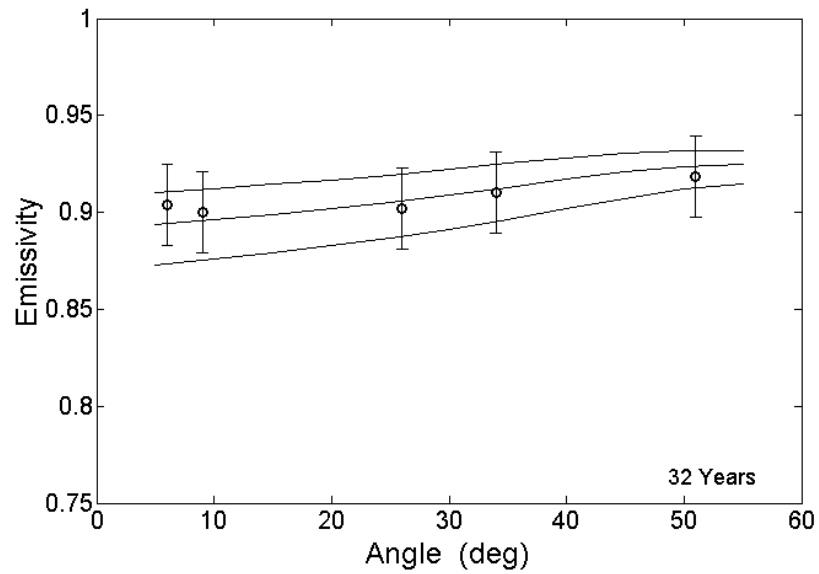


(b)

Figure 6.1: Modeled (lines) and observed ($\pm 1.5\sigma$ error bars) emissivity as a function of angle. L-band, V polarization. Understory-litter optical depths = 0, 0.1, 0.2. (a) 2 years; (b) 5 years.



(a)



(b)

Figure 6.2: Modeled (lines) and observed ($\pm 1.5\sigma$ error bars) emissivity as a function of angle. L-band, V polarization. Understory-litter optical depths = 0, 0.1, 0.2. (a) 26 years; (b) 32 years.

face height standard deviation equal to 1.5 cm. Three values of understory-litter optical depth have been included: 0, 0.1 and 0.2 (lines, from bottom to top). Experimental data include all the 2 year-old stands observed by the radiometer, which have an appreciable dispersion. The best correspondence between simulated and experimental data is obtained with $\tau = 0.2$. The associated standard error is equal to 0.02 emissivity units, mostly due to dispersion in experimental data. Then, the model has been run for the three forest stands of 5, 26 and 32 year-old.

Figure 6.1(b) and 6.2(a)-(b) shows the comparison between simulated emissivities for the same three values of understory/litter optical depth (lines) and experimental data ($\pm 1.5 \sigma$ error bars). For an understory-litter optical depth equal to 0.2 (i.e. the value providing a good fit to the 2 year-old stands emission) the following standard deviation errors are obtained (in emissivity units): 0.012 for the 5 year-old stands, 0.015 for the 26 year-old stands, 0.014 for the 32 year-old stands. These differences may depend to model approximations, related to the large number of forest and soil parameters influencing the overall emissivity, as well as some inaccuracy in the experimental data. For older forests, a slightly better correspondence would be obtained by assuming the understory-litter τ to be lower than 0.2.

6.2 Bray

Bray 2004 is a long term experiment carried out in view of SMOS mission. In fact, a multitemporal set of brightness temperatures was collected in Les Landes coniferous forest, between July and December 2004 [Grant et al. \(2006a,b\)](#). Measurements were carried out by the EMIRAD radiometer, operating at L-band 1.41 GHz and horizontal polarization. The radiometer antenna had a full beamwidth of 25° , and looked downward from a 40 m tower towards a 34 years old Maritime Pine forest, with an average tree height of 22 m. Measurements were averaged to half-hourly values for the final data analysis. A thermal IR radiometer (Heitronics KT 15.85D, 9.6 - 11.5 μm) was fixed next to the microwave instrument to give measurements of canopy temperature over approximately the same footprint. Soil temperature was measured at depths of 1, 2, 4, 8, 16, 64 and 10 cm below the soil surface, using thermocouples made by INRA and a CR21X Campbell Scientific data logger. During the radiometric measurements, volumetric soil moisture at 5 cm depth and litter moisture were measured with a sampling time of 10s and averaged to half-hourly values. Details of the experiment are given in [Grant et al. \(2006a,b\)](#).

Comparison with Experimental Data

In order to simulate the brightness temperatures measured over Bray site by the EMIRAD radiometer, the model was run using as input forest variables previously estimated for Les Landes parcels with an age as close as possible to the age of Bray parcel §6.1. In particular, we considered the data published in Saleh et al. (2005) for the Berganton site, which was 32 years old. Corresponding values of geometrical and physical parameters used as input were given after subdividing forest crown into two levels. For soil and litter variables, values measured on site were adopted. The volumetric soil moisture varied between about 10% and about 30% during the measuring time. Details about moisture measurements are given in Grant et al. (2006a,b). Litter moisture was derived by empirical equation (5.2), whose fresh biomass value was approximatively 10 kg/m².

The model computes the overall emissivity and the single components due to soil, canopy and canopy-soil multiple interactions. In order to evaluate the emitted brightness temperature, the simulated soil emissivity was multiplied by soil temperature, while the other components were multiplied by the canopy temperature. The three terms were finally added to each other. The canopy temperature was assumed to be equal to the measured infrared temperature, while the soil temperature was derived by direct measurements at 1 cm depth. Comparisons were done at a 45° angle and horizontal polarization. Results are shown in Figure 6.3(a), four time intervals with almost continuous measurements have been considered. Days of Year are: 250–252, 255–265, 271–281, 286–307, 313–327, 335–342 and 347–348. Also the trend obtained by neglecting the litter is reported for comparison. Figure 6.3(b) shows the trends of canopy temperature, soil temperature, and soil moisture. It may be observed that the measured brightness temperature shows daily variations, mostly related to variations of canopy temperature, and long term variations, related to a seasonal effect of temperature decrease and soil moisture increase. The model reproduces well both the absolute values of brightness temperature and its variations, although with a slight overestimation. If litter is not considered, an evident underestimation is observed, although variations are still represented. The overall standard error between measurements and simulations is equal to 3.65 K and increases up to 17.98 K if litter is not included in the model.

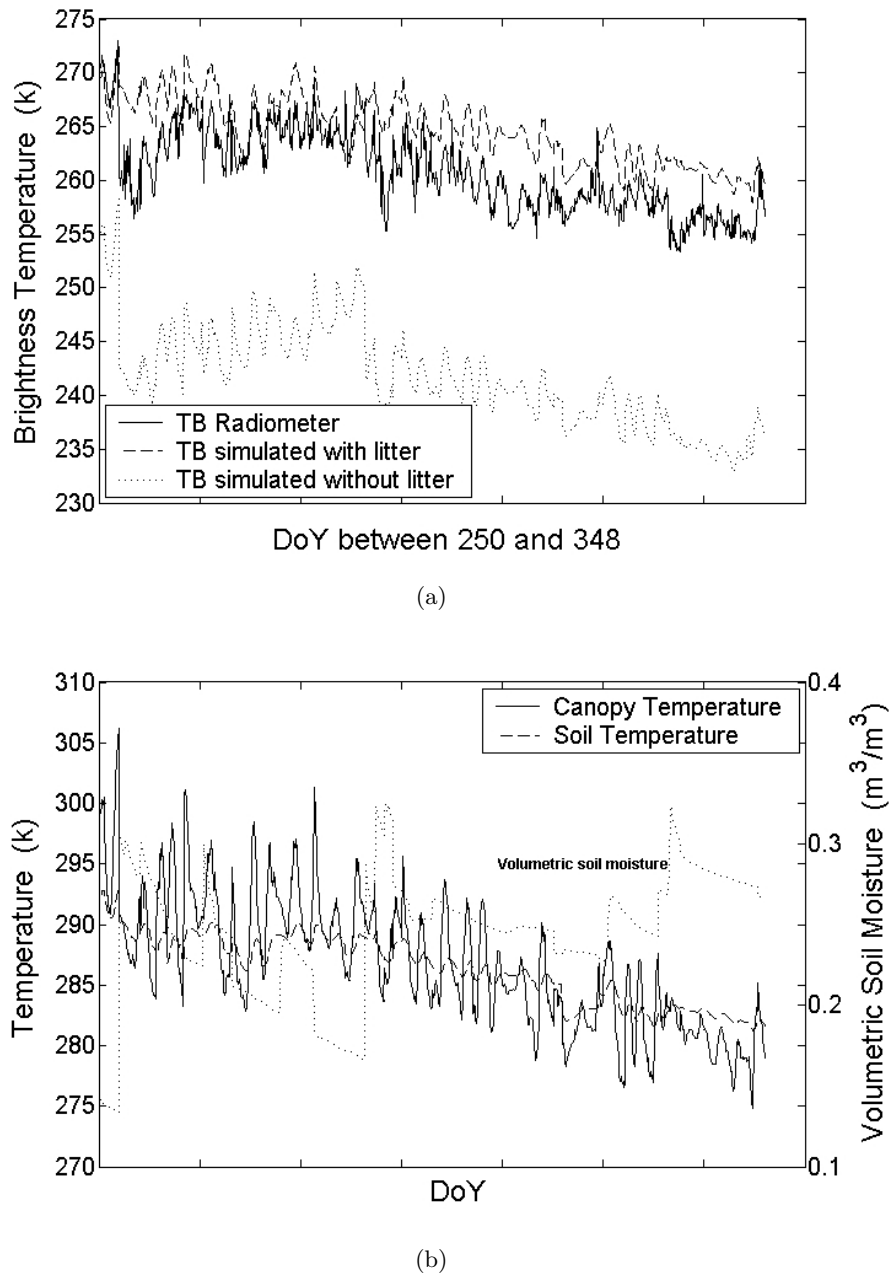


Figure 6.3: Multitemporal trends at Bray site. (a) Brightness temperature (measured, simulated including litter, simulated without litter) at 45° , H polarization; (b) Soil moisture, soil and canopy temperature.

6.3 Jülich

A long term experiment was carried out on the deciduous forest site in the research centre of Jülich (Germany), between the autumn 2004 to spring 2005. Two radiometers were used for the experiment, the L-band 1.4 GHz radiometer ELBARA and the X-band radiometer MORA at 11.4 GHz. Thermal infrared temperature was measured by means the infrared radiometer Everest Interscience 4000.4ZH, carried on ELBARA, whose spectral range is $[8-15] \mu m$ and temperature range is $[243-1033] K$ with an accuracy of $\pm 1 K$. Both the microwave and infrared instruments have a beamwidth about 15° . The thermistor Campbell S-TL107 was used in order to collect soil surface temperature between 0 cm and 16 cm of deep, furthermore a continuous monitoring of soil moisture values was carried out.

During the campaign two different radiometer configurations were adopted, Figure 6.4(a)-(b), give a sketch of both. Hereafter they will be named respectively “Upward Looking” configuration and “Downward Looking” configuration.

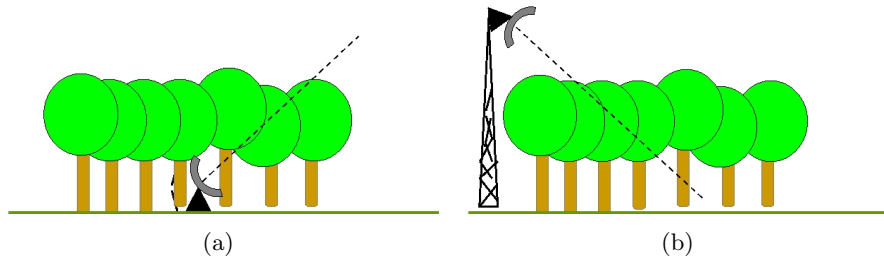


Figure 6.4: Sketch of radiometer configuration: (a) Upward configuration; (b) Downward configuration.

Upward Looking

This radiometer configuration, was adopted in the first part of the experiment, between 30th of September and 22nd of November 2004. All the instruments were located on a track, under the observed forest, and directed towards to the sky, as depicted in Figure 6.4(a).

Unfortunately, not all the information about soil and vegetation were collected, (moisture and temperature). Some of the available information are plotted in Figure 6.5, also *Dbh* distribution was made available. For this reason, only *LAI* value, indirectly obtained from the leaves biomass, and

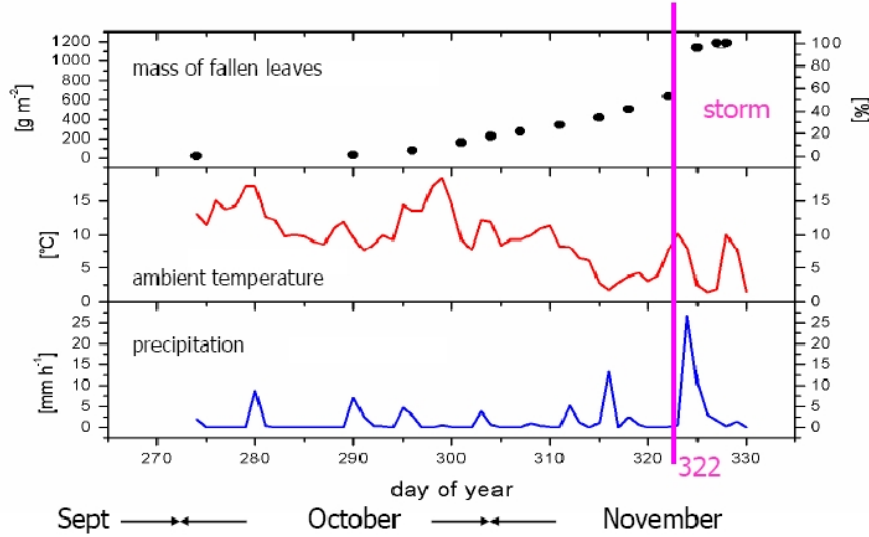
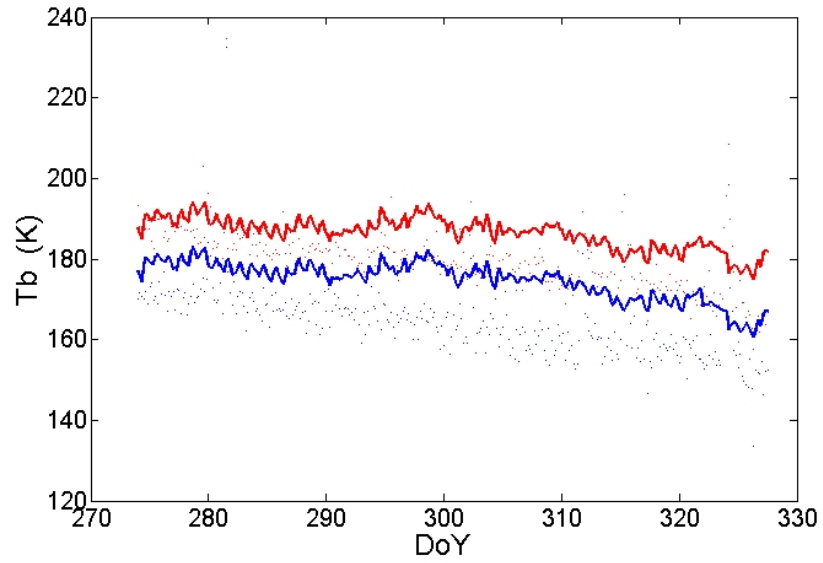


Figure 6.5: Data ground collected during the experiment. From bottom to up, precipitation rate [mm/ha], environmental temperature °C and leaves fallen.

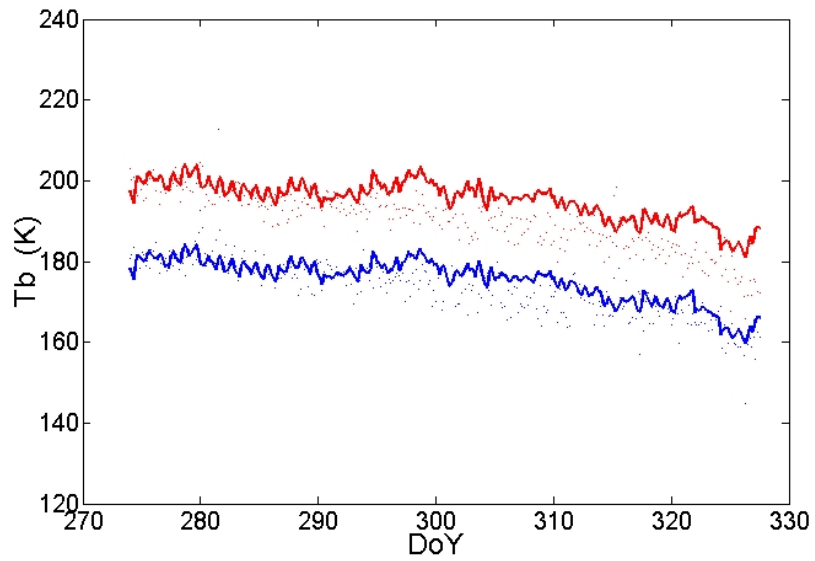
plants density were used as input for the model, and the overall description of the canopy were taken by the canopy growth routine, and litter model, proposed in Chapter 5.

The particular configuration and the long period of observation make it possible to get an insight into specific problems: a) to single out the vegetation contribution, b) to take advantage from the defoliation in order to also analyse the leaf emissivity component.

Results are shown in Figure 6.6(a)-(b). Measured and simulated brightness temperatures are shown as a function of the day of year. Measured crown brightness temperatures are about 180–190 K, and decrease by about 20 K during the defoliation process. It is quite clear that a T_b decrease of almost 10K is due to the temperature (Figure 6.5), while the remaining 10K are due at the defoliation effect. These brightness values are appreciably lower than values measured by downward looking radiometers, observing soils covered by forests. Therefore, the experiment confirms the prediction that in future spaceborne observations, at L-band, the emission of soil/litter ensemble will be appreciable, even under dense forests. The model reproduces with a quite good accuracy the absolute brightness values and the defoliation effects. Horizontally polarized brightness temperatures are slightly



(a)



(b)

Figure 6.6: Comparison between simulated (continuous lines) and measured (dots) brightness temperatures vs. Day of Year, 40° (blue) and 60° (red): (a) V polarization; (b) H polarization.

higher than vertically polarized ones. Also this effect is reproduced by the model, at least at 60° , and is attributed to polarized trunk shadowing which occurs for the particular configuration of this experiment, i.e. with an upward looking radiometer.

Downward Looking

In the second part of the campaign the radiometers were moved on a 100m high tower, and looked down towards the same forest site analyzed in the first part of the experiment. The aim of the experiment was still to investigate about the radiometric sensitivity with respect to known variables under a dense forest. In order to single out canopy emission from soil emission, a foil was also introduced under the forest during the spring 2005, as shown in Figure 6.7(a)-(b).

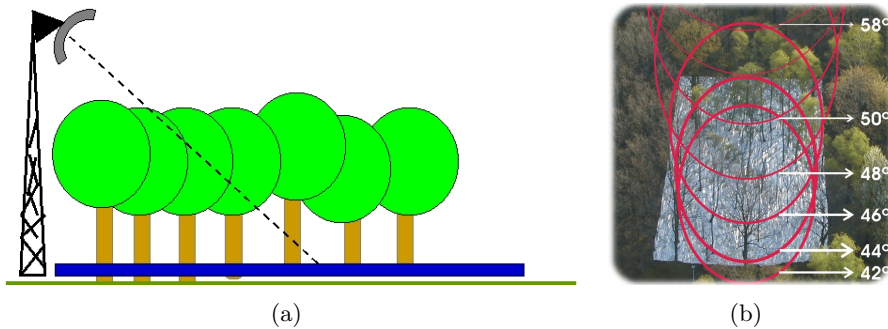
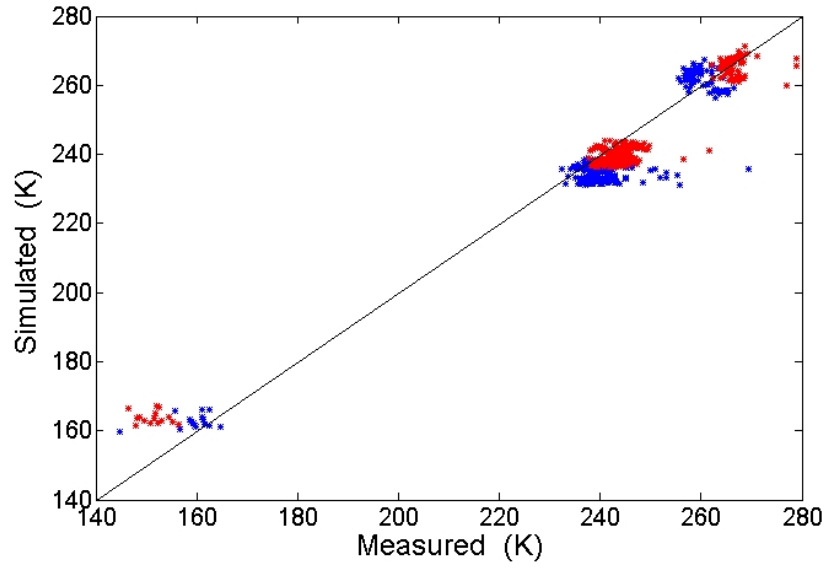


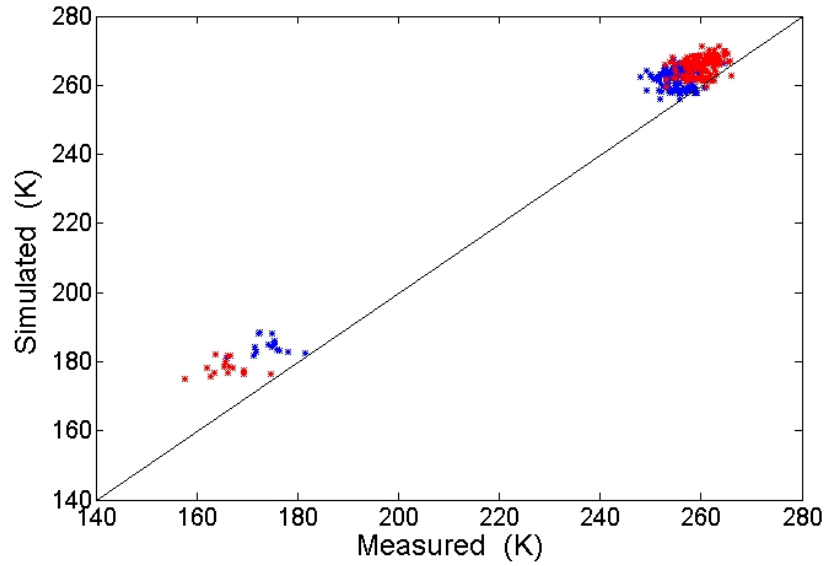
Figure 6.7: Downward looking configuration with foil: (a) sketch of the configuration; (b) picture of the foil from the tower.

The Figure 6.8(a)-(b) show a direct comparison among T_b collected for all the described radiometer configurations, at observation angle of 40° and 60° , and when the defoliation was completed. By comparison between the brightness temperature values with the sky as background and the radiometric values collected from the tower with the soil as background, it is possible to single out the soil and the canopy contributions. Under the enhanced developed forest of Jülich, the difference between upward looking and downward looking T_b 's is almost 100K at 40° and 80K at 60° . Moreover at 40° , where radiometric data were collected from the tower still in the presence of the foil, it is possible quantify the alteration induced by it, which is at about 20K.

The Figure 6.8(a)-(b) also shows the predicted brightness temperatures



(a)



(b)

Figure 6.8: Data collected from both the radiometer configurations: (a) observation angle of 40° ; (b) observation angle of 60° .

versus measured values. The model shows a quite good reliability in the reproduction of the brightness temperature, in all the proposed radiometric configurations. The discrepancy are small, when compared with the overall dynamic range.

6.4 STAAARTE

A multifrequency campaign, was carried out in the framework of the European Community Scientific Training and Access to Aircraft for Atmospheric Research Throughout Europe (STAAARTE) 1999 Project [Macelloni et al. \(2001a\)](#). Scope of the project was to investigate about the use of microwave radiometry in the study of characteristics of Mediterranean forests, in particular forest classification and phenological status by means of the higher frequencies and forest biomass estimation by means of lower frequencies.

The IROE microwave sensors, operating at several frequencies (1.4, 6.8, 10 and 37 GHz) characterized by a radiometric accuracy of about 1 K, were located over two different aircrafts. An ARAT (Fokker 27) hosted the higher frequency instruments, dual polarization and with an observation angle of 30° . Instead, an ultralight aircraft carried on the L-band radiometer at vertical polarization. Both the ARAT and the ultralight aircraft carried of an infrared radiometer (8–14 μm), in order to estimate the surface temperature and hence the emissivity.

The observed forest sites included both deciduous species, beech (*Fagus sylvatica*), turkey oak (*Quercus cerris* L.), holm oak (*Quercus ilex* L.) and two coniferous forest sites, fir and pine.

During the campaign several ground data were collected. A quite detailed information regarding the forest were collected, in particular LAI, trunk diameter, basal area, plant density, height and woody volume were measured, but no information about soil has been taken. As the flies, have taken place two weeks late the last significant rainfall, it is reasonable to suppose a quite homogeneous and dry soil.

Comparison with Experimental Data

In order to propose a model comparison with the radiometric data collected during the experiment, showed in Figure 6.9, some of the ground data were used in input for the Tor Vergata Model. As not all the information required by the model was available from ground measurements, the canopy growth routine and litter model, proposed in Chapter 5 was adopted. The roughness soil standard deviation has been fixed equato to 1 cm, and the soil moisture

content to 5% in summer and 15% in winter. The presence of an understory with an optical thickness of 0.1 (due to a biomass of about 1 Kg/mm²) has been taken into account in the summerr simulations.

The basic input used were the LAI value and plant density, the forest canopy data are summarized in the Table 6.4.

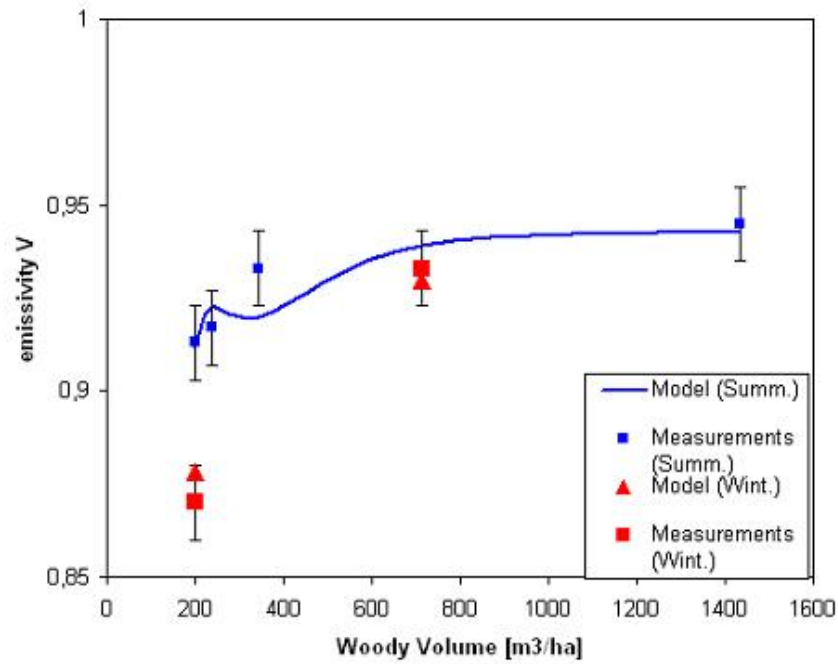


Figure 6.9: Comparison between simulated data and radiometric values collected during the campaign, over the sites specified in the Table 6.4

Site	Dbh Range [cm]	Mean Dbh [cm]	Dbh Std	LAI
Uignano				
Turkey Oak	0–40	13.5	10	0–2.2*
Cologne				
Holm Oak	0–40	19.5	10	5.1
Cala Violina				
Holm Oak	0–40	14.9	10	4.2
Teso				
Beech	0–80	36	10	0–3.6*
Vallombrosa				
Beech	0–80	40.5	10	4.3

Table 6.1: Main ground data collected in the deciduous site, * Respectively winter and summer Leaf Area Index (LAI) values.

Bibliography

- Alvarez-Perez, J. (2001). An extension of the IEM/IEMM surface scattering model. *Waves in Random Media*, 11:307–329.
- Attema, E. and Ulaby, F. (1978). Vegetation modeled as a water cloud. *Radio Science*, 13:357–364.
- Blaes, X. (2005). *Experimental and modelling analysis for crop monitoring using advanced SAR remote sensing techniques*. PhD thesis, Université Catholique de Louvain, Belgium.
- Bracaglia, M., Ferrazzoli, P., and Guerriero, L. (1995). A fully polarimetric multiple scattering model for crops. *Remote Sensing of the Environment*, 54:170–179.
- Cannell, M. (1982). *World Forest Biomass and Primary Production Data*. New York: Academic.
- Champeaux, J., Kyung-Soo, H., Arcos, D., Habets, F., and Masson, V. (2004). Ecoclimap II: A new approach at global and european scale for ecosystems mapping and associated surface parameters database using SPOT/VEGETATION data - first results. Proceedings of IGARSS 2004.
- Chauhan, N., Lang, R., and Ranson, K. (1991). Radar modeling of a boreal forest. *IEEE Trans. Geosci. Remote Sensing*, 29.
- Chiu, T. and Sarabandi, K. (2000). Electromagnetic scattering from short branching vegetation. *IEEE Trans. Geosci. Remote Sensing*, 38:911–925.
- Cookmartin, G., Saich, P., Quegan, S., Cordey, R., Burgess-Allen, P., and Sowter, A. (2000). Modeling microwave interactions with crops and comparison with ERS-2 sar observations. *IEEE Trans. Geosci. Remote Sensing*, 38:658–670.

- De Roo, R., Du, Y., Ulaby, F., and Dobson, M. (2001). A semiempirical backscattering model at L-band and C-band for a soybean canopy with soil moisture inversion. *IEEE Trans. Geosci. Remote Sensing*, 39:864–872.
- Della Vecchia, A., Ferrazzoli, P., Giorgio, F., and Guerriero (2006a). A large scale approach to estimate L-band emission from forest covered surfaces. Proceedings of RAQRS 2006.
- Della Vecchia, A., Ferrazzoli, P., and Guerriero, L. (2004). Modeling microwave scattering from long curved leaves. *Waves in Random Media*, 14:333–343.
- Della Vecchia, A., Ferrazzoli, P., Guerriero, L., Blaes, X., Defourny, P., Dente, L., Mattia, F., Satalino, G., Strozzi, T., and Wegmuller, U. (2006b). Influence of geometrical factors on crop backscattering at C-band. *IEEE Trans. Geosci. Remote Sensing*, 44:778–790.
- Della Vecchia, A., Guerriero, L., Bruni, I., and Ferrazzoli, P. (2006c). A hollow cylinder microwave model for stems. *Journal of Electromagnetic Waves and Applications*, 20:301–318.
- Della Vecchia, A., Saleh, K., Ferrazzoli, P., Guerriero, L., and Wigneron, J. (2006d). Simulating L band emission of coniferous forests using a discrete model and a detailed geometrical representation. *IEEE Geoscience and Remote Sensing Letters*, 3:364–368.
- Dobson, M., Ulaby, F., Hallikainen, M., and El-Rayes, M. (1985). Microwave dielectric behavior of wet soil - part II: Dielectric mixing models. *IEEE Trans. Geosci. Remote Sensing*, 23:35–45.
- Eom, H. and Fung, A. (1984). A scatter model for vegetation up to Ku-band. *Remote Sensing of the Environment*, 15:185–200.
- Ferrazzoli, P. and Guerriero, L. (1995). Radar sensitivity to tree geometry and woody volume: a model analysis. *IEEE Trans. Geosci. Remote Sensing*, 33:360–371.
- Ferrazzoli, P. and Guerriero, L. (1996). Passive microwave remote sensing of forests: a model investigation. *IEEE Trans. Geosci. Remote Sensing*, 34:433–443.
- Ferrazzoli, P., Guerriero, L., and Wigneron, J. (2002). Simulating L-band emission of forests in view of future satellite applications. *IEEE Trans. Geosci. Remote Sensing*.

- Ferrazzoli, P., Wigneron, J., Guerriero, L., and Chanzy, A. (2000). Multifrequency emission of wheat: modeling and applications. *IEEE Trans. Geosci. Remote Sensing*, 38:2598–2607.
- Franchois, A., Piñeiro, Y., and Lang, R. (1998). Microwave permittivity measurements of two conifers. *IEEE Trans. Geosci. Remote Sensing*, 36:1384–1395.
- Franz, V. W. (1948). Zur formulierung des huygensschen prinzipts. *Z. Naturforsch*, 3a:500–506.
- Fung, A. (1979). Scattering from a vegetation layer. *IEEE Trans. Geosci. Remote Sensing*, 17:1–6.
- Fung, A. (1994). *Microwave scattering and emission models and their applications*. Artech House.
- Fung, A. and Ulaby, F. (1978). A scatter model for leafy vegetation. *IEEE Trans. Geosci. Remote Sensing*, 16:281–286.
- Grant, J., Wigneron, J., Van de Griend, A., Ruffiéé, G., Della Vecchia, A., Skou, N., and Le Crom, B. (2006a). L-band radiometric behaviour of pine forests for a variety of surface moisture conditions. Proceedings of RAQRS 2006.
- Grant, J., Wigneron, J., Van de Griend, A., Schmidl Søbjerg, S., and Skou, N. (2006b). Bray 2004 field experiment on microwave forest radiometry - L-band signal behaviour for varying conditions of surface wetness. *Remote Sensing of Environment*, in press.
- Hallikainen, M., Ulaby, F., Dobson, M., El-Rayes, M., and Wu, F. (1985). Microwave dielectric behaviour of wet soil-part I: Empirical models and experimental observations. *IEEE Trans. Geosci. Remote Sensing*, GE-23:25–34.
- Jackson, T., Schmugge, T., and Wang, J. (1982). Passive microwave sensing of soil-moisture under vegetation canopies. *Water Resources Research*, 18:1137–1142.
- Jenkins, J., Chojnacky, D., Heath, L., and Birdsey, R. (2004). Comprehensive database of diameter-based biomass regressions for north american tree species. Technical report, United States Department of Agriculture, <http://www.fs.fed.us/ne>. General Technical Report NE-319.

- Jenkins, J. C., Chojnacky, D., Heath, L. S., and Birdsey, R. A. (2003). National-scale biomass estimators for united states tree species. *Forest Science*, 49:12–26.
- Karam, M. and Fung, A. (1988). Electromagnetic scattering from a layer of finite-length, randomly oriented circular cylinder over a rough interface with application to vegetation. *International Journal of Remote Sensing*, 9:1109–1134.
- Karam, M., Fung, A., and Antar, Y. (1988). Electromagnetic wave scattering from some vegetation samples. *IEEE Trans. Geosci. Remote Sensing*.
- Karam, M., Fung, A., Lang, R., and Chauhan, N. (1992). A microwave scattering model for layered vegetation. *IEEE Trans. Geosci. Remote Sensing*, 30:767–784.
- Karam, M. A. (1997). A physical model for microwave radiometry of vegetation. *IEEE Trans. Geosci. Remote Sensing*.
- Kasischke, E., Christensen, N., and Haney, E. M. (1994). Modeling of geometric properties of loblolly pine tree and characteristics for use in radar backscatter studies. *IEEE Trans. Geosci. Remote Sensing*, 32:800–822.
- Kerr, Y. H., Waldteufel, P., Wigneron, J.P. nad Martinuzzi, J., Font, J., and Berger, M. (2001). Soil moisture retrieval from space: the soil moisture and ocean salinity (SMOS) mission. *IEEE Trans. Geosci. Remote Sensing*, pages 1729–1735.
- Kirdyashev, K., Chukhlantsev, A., and Shutko, A. (1979). Microvawe radiation of the earth's surface in the presence of vegetation cover. *Radiotekhnika*, pages 256–264.
- Kolawole, M. (1992). Scattering from dielectric cylinders having radially layered permittivity. *Journal of Electromagnetic Waves and Applications*, 6:235–259.
- Le Vine, D., Meneghini, R., Lang, R., and Seker, S. (1983). Scattering from arbitrarily oriented dielectric disks in the physical optics regime. *Journal of Optical Soc. America*, 73:1255–1262.
- Lin, Y. and Sarabandi, K. (1995). Electromagnetic scattering model for a tree trunk above a tilted ground plane. *IEEE Trans. Geosci. Remote Sensing*, 33:1063–1070.

- Macelloni, G., Paloscia, S., and Pampaloni (2001a). Airborne multifrequency L- to Ka- band radiometric measurements over forests. *IEEE Trans. Geosci. Remote Sensing*, 39:2507–2513.
- Macelloni, G., Paloscia, S., Pampaloni, P., Marliani, F., and Gai, M. (2001b). The relationship between the backscattering coefficient and the biomass of narrow and broad leaf crops. *IEEE Trans. Geosci. Remote Sensing*, 39:873–884.
- Marliani, F., Paloscia, S., Pampaloni, P., and Kong, J. (2002). Simulating coherent backscattering from crops during the growing cycle. *IEEE Trans. Geosci. Remote Sensing*, 40:162–177.
- Masson, V., Champeaux, J., Chauvin, F., Meriguet, C., and Lacaze, R. (2003). A global database of land surface parameters at 1-km resolution in meteorological and climate models. *Journal of Climate*, 16:1261–1282.
- Mätzler, C. (1994). Microwave (1–100 GHz) dielectric model of leaves. *IEEE Trans. Geosci. Remote Sensing*.
- Mo, T., Choudhury, B., Schmugge, T., Wang, J., and Jackson, T. (1982). A model for microwave emission from vegetation-covered fields. *Journal of Geophysical Research*, 87(11):229–237.
- Monserud, R. and Marshall, J. (1999). Allometric crown equation in three northern idhao conifer species. *Canadian Journal of Forest Research*, 29:521–535.
- Oh, Y., Yang, Y., and Sarabandi, K. (2002). Full-wave analysis of microwave scattering from short vegetation: an investigation on the effect of multiple scattering. *IEEE Trans. Geosci. Remote Sensing*, 40:2522–2526.
- Paloscia, S. (1991). Note riguardanti i singoli campi dell’area di test di montespertoli. Technical report, IROE-CNR Report RT193.
- Pampaloni, P. (2004). Microwave radiometry of forests. *Waves Random Media*, 14:S275–S298.
- Prévoit, L., Dechambre, M., Taconet, O., Vidal-Majar, D., Normand, M., and Galle, S. (1993). Estimating the characteristics of vegetation canopies with airborne radar measurements. *International Journal of Remote Sensing*, 14:2803–2818.

- Putuhena, W. and Cordery, L. (1996). Estimation of interception capacity of the forest flood. *Journal of Hydrology*, 180:283–299,.
- Ranson, K., Sun, G., Weishampel, J., and Knox, R. (1997). Forest biomass from combined ecosystem and radar backscatter modeling. *Remote Sensing of the Environment*, 59:118–133.
- Saleh, K. and Wigneron, J., Calvet, J., Lopez-Baeza, E., Ferrazzoli, P., Berger, M., Wursteisen, P., Simmonds, L., and Miller, J. (2004). The EuroSTARRS airborne campaign in support of the SMOS mission: first results over land surfaces. *International Journal of Remote Sensing*, 25:177–194.
- Saleh, K., Porte, A., Guyon, K., Ferrazzoli, P., and Wigneron, J. (2005). A geometric description of a maritime pine forest suitable for discrete microwave models. *IEEE Trans. Geosci. Remote Sensing*.
- Sarabandi, K., Senior, T., and Ulaby, F. (1988). Effect of curvature on the backscattering from a leaf. *Journal of Electromagnetic Waves and Applications*, 2:653–670.
- Schelkunoff, S. (1936). Some equivalence theorems of electromagnetics and their applications to radiation problems. *B.S.T.J.*, 15:92–112.
- Seker, S. and Schneider, A. (1988). Electromagnetic scattering from a dielectric cylinder of finite length. *IEEE Trans Antennas Propagation*, 36:303–07.
- Senior, T., Sarabandi, K., and Ulaby, F. (1987). Measuring and modeling the backscatter cross section of a leaf. *Radio Science*, 22:1109–1116.
- Stiles, J. and Sarabandi, K. (2000). Electromagnetic scattering from grassland - part I: a fully phase-coherent scattering model. *IEEE Trans. Geosci. Remote Sensing*, 38:339–348.
- Stogryn, A. (1974). Electromagnetic scattering by random dielectric constant fluctuation in a bounded medium. *Radio Science*, 9:509–518.
- Stratton, J. (1941). *Electromagnetic Theory*. McGraw-Hill, New York, I edition.
- Tatarskii, V. (1964). Propagation of electromagnetic wave in a medium with strong dielectric constant fluctuations. *Soviet. Phys. J.E.P.T.*, 19.

- Touré, A., Thompson, K., Edwards, G., Brown, R., and Brisco, B. (1994). Adaptation of MIMICS backscattering model to the agricultural context - wheat and canola at L and C-bands. *IEEE Trans. Geosci. Remote Sensing*, 32:47–61.
- Tsang, L., Ding, K., Zhang, G., Hsu, C., and Kong, J. (1995). Backscattering enhancement and clustering effects of randomly distributed dielectric cylinders overlying a dielectric half space based on Monte-Carlo simulations. *IEEE Trans. Antennas Propagat.*, 43:488–499.
- Tsang, L. and Kong, J. (1981). Application of strong fluctuation random medium theory to scattering from vegetation-like half space. *IEEE Trans. Geosci. Remote Sensing*, 19:62–68.
- Tsang, L., Kong, J., and Shin, R. (1985). *Theory of Microwave Remote Sensing*. John Wiley & Sons.
- Twomey, S., Jacobowitz, H., and Howell, H. (1966). Matrix methods for multiple scattering problems. *Journal of Atmospheric Sciences*, 23:289–295.
- Ulaby, F. and El-Rayes, M. (1987). Microwave dielectric spectrum of vegetation - part II: Dual dispersion model. *IEEE Trans. Geosci. Remote Sensing*, 25:550–556.
- Ulaby, F. and Elachi, C. (1990). *Radar Polarimetry for Geoscience Applications*. Artech Hous.
- Ulaby, F., Moore, R., and Fung, A. (1982). *Microwave Remote Sensing. Active and Passive - Vol. I*, volume I. Addison Wesley, Reading (USA).
- Ulaby, F., Moore, R., and Fung, A. (1986). *Microwave Remote Sensing: Active and Passive*, volume III. Artech House, Dedham (USA).
- Ulaby, F., Sarabandi, K., McDonald, K., Whitt, M., and Dobson, M. (1990). Michigan microwave canopy scattering model. *International Journal of Remote Sensing*, 11:1223–1253.
- Van de Hulst, H. (1957). *Light scattering by small particles*. Wiley, New York.
- Wegmüller, U. (1993). Signature research for crop classification by active and passive microwaves. *International Journal of Remote Sensing*, 14:871–883.

- Wegmüller, U., Strozzi, T., Ferrazzoli, P., Guerriero, L., Della Vecchia, A., Mattia, F., Dente, L., Satalino, G., Blaes, X., Defourny, P., and Verhoest, N. (2005). Development of SAR inversion algorithms for land application. Technical report, Final Report ESA/ESTEC Contract n. 17011/03/NL/JA.
- Wigneron, J., Chanzy, A., Calvet, J., and Bruguier, N. (1995). A simple algorithm to retrieve soil moisture and vegetation biomass using passive microwave measurements over crop fields. *Remote Sensing of the Environment*, 51:331–341.
- Wigneron, J., Ferrazzoli, P., Oliso, A., Bertuzzi, P., and Chanzy, A. (1999). A simple approach to monitor crop biomass from C-band radar data. *Remote Sensing of the Environment*, 69:179–188.

Curriculum Vitae

ANDREA DELLA VECCHIA

Education

- December 2006, Geoscience PhD at Tor Vergata University, Roma
- December 2002, MS degree in Telecommunication Engineer at the Tor Vergata University, Rome with 110/110 cum laude
- October 2001, BS degree in Telecommunication Engineer at the Tor Vergata University, Rome with 110/110 cum laude

Stay abroad

- USDA–ARS Hydrology and Remote Sensing Laboratory, Beltsville (MD), USA, May–August 2006
- EPHYSE, INRA Bordeaux (France), October–December 2004

List of Publications

Papers

- **Della Vecchia, A.**, Saleh, K., Ferrazzoli, P., Guerriero, L., and Wigneron, J.P. (2006). Simulating L-band emission of coniferous forests using a discrete model and a detailed geometrical representation. *IEEE Geoscience and Remote Sensing Letters*, 3:364–368.
- Blaes, X., Defourny, P., Wegmuller, U., **Della Vecchia, A.**, Guerriero, L., and Ferrazzoli, P. (2006). C-band polarimetric indices for maize monitoring based on a validated Radiative Transfer model. *IEEE Transactions on Geoscience and Remote Sensing*, 44:791–800.
- **Della Vecchia, A.**, Ferrazzoli, P., Guerriero, L., Blaes, X., Defourny, P., Dente, L., Mattia, F., Satalino, G., Strozzi, T., and Wegmuller, U. (2006). Influence of geometrical factors on crop backscattering at C-band. *IEEE Trans. Geosci. Remote Sensing*, 44:778–790.
- **Della Vecchia, A.**, Guerriero, L., Bruni, I., and Ferrazzoli, P. (2006). A hollow cylinder microwave model for stems. *Journal of Electromagnetic Waves and Applications*, 20:301–318.
- **Della Vecchia, A.**, Ferrazzoli, P., and Guerriero, L. (2004). Modeling microwave scattering from long curved leaves. *Waves in Random Media*, 14:S333–S343.

Conferences

- **A. Della Vecchia**, P. Ferrazzoli, S. Lisi, G. Schiavon, “Studio sullemissione multifrequenza di foreste boreali”, XIII Riunione Cetem e IV Workshop AIT sul Telerilevamento a Microonde, Milano (ITA), November 2006.

- **A. Della Vecchia**, P. Ferrazzoli, L. Guerriero, E. Santi, F. Ticconi, “Studio modellistico sul telerilevamento di foreste in banda L: sistemi passivi, attivi monostatici e bistatici”, XIII Riunione Cetem e IV Workshop AIT sul Telerilevamento a Microonde, Milano (ITA), November 2006.
- **A. Della Vecchia**, P. Ferrazzoli, L. Guerriero, L. Ninivaggi, “Studio modellistico e sperimentale sul monitoraggio di vegetazione agricola con radar multifrequenza”, XIII Riunione Cetem e IV Workshop AIT sul Telerilevamento a Microonde, Milano (ITA), November 2006.
- M. Guglielmetti, M. Schwank, C. Matzler, **A. Della Vecchia**, P. Ferrazzoli, C. Oberdorster, H. Fluhler, “Microwave radiometry experiments on a deciduous forest site” , 2nd International Symposium on Recent Advances in Quantitative Remote Sensing, Torrent, Valencia, (SPA), 25–29 September 2006.
- **A. Della Vecchia**, P. Ferrazzoli, F. Giorgio, L. Guerriero, “A large scale approach to estimate L-band emission from forest covered surfaces”, 2nd International Symposium on Recent Advances in Quantitative Remote Sensing, Torrent, Valencia, (SPA), 25–29 September 2006.
- **A. Della Vecchia**, P. Ferrazzoli, J. P. Grant, M. Guglielmetti, M. Schwank, J.-P. Wigneron, “Modelling forest emission and comparisons with ground-based radiometric measurements”, 2nd International Symposium on Recent Advances in Quantitative Remote Sensing, Torrent Valencia (SPA), 25–29 September 2006.
- J.P. Grant, J.P. Wigneron, A. Van de Gried, F. Demontoux, G. Ruffi, **A. Della Vecchia**, N. Skou, B. Le Crom, “L-band radiometric behaviour of pine forests for a variety of surface moisture conditions”, 2nd International Symposium on Recent Advances in Quantitative Remote Sensing, Torrent Valencia (SPA), 25–29 September 2006.
- **A. Della Vecchia**, P. Ferrazzoli, L. Guerriero, “Monitoraggio di vegetazione agricola nelle bande di frequenza tra 1 e 11 Ghz”, Riunione Nazionale di Elettromagnetismo, Genova (ITA), 18–21 September 2006.
- **A. Della Vecchia**, P. Ferrazzoli, L. Guerriero, L. Ninivaggi, D. Scalon, T. Strozzi, U. Wegmller, “Modeling multi-frequency scattering of wheat

and maize during the whole growth cycle”, 2006 International Geoscience and Remote Sensing Symposium, Denver (USA), 31 July-04 August 2006.

- **A. Della Vecchia**, P. Ferrazzoli, F. Giorgio, L. Guerriero, M. Guglielmetti, M. Schwank, “A parametric study about soil emission and vegetation effects for forests at L-band”, 2006 International Geoscience and Remote Sensing Symposium, Denver (USA), 31 July-04 August 2006.
- **A. Della Vecchia**, P. Ferrazzoli, L. Guerriero, M. Guglielmetti, M. Schwank, H. Fluhler, C. Matzler, “Modeling microwave emission from forests and comparisons with ground based radiometric measurements”, 2006 International Geoscience and Remote Sensing Symposium, Denver (USA), 31 July-04 August 2006.
- **A. Della Vecchia**, P. Ferrazzoli, L. Guerriero, I. Cacucci, M. Marzano, N. Pierdicca, F. Ticconi, “Optimization of bistatic radar configurations for vegetation monitoring”, 2006 International Geoscience and Remote Sensing Symposium, Denver (USA), 31 July-04 August 2006.
- **A. Della Vecchia**, P. Ferrazzoli, L. Guerriero, J.-P. Wigneron, J. P. Grant, M. Guglielmetti, M. Schwank, “Recent studies of forest emission at L-band, in view of SMOS”, 6th SMOS Workshop, Copenhagen (DK), May 2006.
- M. Guglielmetti, M. Schwank, C. Matzler, **A. Della Vecchia**, P. Ferrazzoli, C. Oberdorster, H. Fluhler, “Microwave radiometry experiments on a deciduous forest site”, European Geosciences Union General Assembly, Wien (AUS) , 24–29 April 2006.
- **A. Della Vecchia**, P. Ferrazzoli, L. Guerriero, M. Guglielmetti, M. Schwank, H. Fluhler, C. Matzler, “Experimental and model investigation about forest emission at L-band”, Progress in Electromagnetic Research Symposium , Cambridge (USA), 26–29 March 2006.
- **A. Della Vecchia**, P. Ferrazzoli, L. Guerriero, “Model approaches for scattering and extinction of thin stems”, Progress in Electromagnetic Research Symposium , Cambridge (USA), 26–29 March 2006.
- J. Grant, A.A. Van de Griend, J.-P. Wigneron, S. Sobjarg, **A. Della Vecchia**, A. Kruszezski, S. Debesa, N. Skou, J. Balling, “L-band multi-angle radiometric properties of pine forest; some preliminary results

of Bray 2004”, 11th SPIE International Symposium on Remote Sensing, Bruges (BEL), 19–22 September 2005.

- J. Ballino, **A. Della Vecchia**, J. Grant, S. Schmidl, N. Skou, A. Van de Griend, J.-P. Wigneron, “Bray 2004 - A long-term experiment on L-band forest radiometry”, European Geosciences Union General Assembly, Wien (AUS) , 24–29 April 2005.
- **A. Della Vecchia**, P. Ferrazzoli, L. Guerriero, K. Saleh, J.-P. Wigneron, “Modeling L-band radiometric sensitivity to soil moisture under forests and comparisons with EUROSTARRS signatures”, European Geosciences Union General Assembly, Wien (AUS), 24–29 April 2005.
- **A. Della Vecchia**, P. Ferrazzoli, L. Guerriero, L. Dente, F. Mattia, G. Satalino, T. Strozzi, U. Wegmuller, “Influence of geometrical factors and permittivity models on crop backscattering at C-band”, 4th International Symposium on Retrieval of Bio- and Geophysical Parameters from SAR Data for Land Applications, Innsbruck (AUS), November 2004.
- X. Blaes, P. Defourny, **A. Della Vecchia**, L. Guerriero, P. Ferrazzoli, “Impact of the agronomical parameters variability on SAR signal”, 4th International Symposium on Retrieval of Bio- and Geophysical Parameters from SAR Data for Land Applications, Innsbruck (AUS), November 2004.
- **A. Della Vecchia**, I. Bruni, P. Ferrazzoli, L. Guerriero, “Recent advances in crop modeling: the curved leaf and the hollow stem”, 2004 International Geoscience and Remote Sensing Symposium, Anchorage (USA), September 2004.
- K. Saleh, L. Guerriero, **A. Della Vecchia**, P. Ferrazzoli, J.-P. Wigneron, A. Port, B. Guyon, “A radiative model to simulate forest emission at L-band: sensitivity of brightness temperature to forest components”, 2004 International Geoscience and Remote Sensing Symposium, Anchorage (USA), September 2004.
- I. Bruni, **A. Della Vecchia**, P. Ferrazzoli, L. Guerriero, “Recenti sviluppi nella modellistica degli elementi della vegetazione”, Quindicesima Riunione Nazionale di Elettromagnetismo, Cagliari (ITA), September 2004

- **A. Della Vecchia**, P. Ferrazzoli, L. Guerriero, K. Saleh, J.P. Wigneron, “Retrieving soil moisture under forests with L-band spaceborne instruments: simulation of perturbing effects”, European Geosciences Union 1st General Assembly, Nice (FRA), April 2004
- **A. Della Vecchia**, P. Ferrazzoli, L. Guerriero, “A Model Study of Leaf Curvature Effect on Microwave Vegetation Scattering”, International Geoscience and Remote Sensing Symposium, Toulouse (FRA), July 2003.

List of Tables

4.1	Main observation parameters and ground data used in model simulation of the corn RASAM scatterometer data at Central Plain.	52
4.2	Main observation parameters and ground data used in model simulation of the wheat ERS-2 SAR data at Matera in the 2001 campaign	54
4.3	Main observation parameters and ground data used in model simulation of the wheat ENVISAR and ERS-2 SAR data at the field 5 of Matera in the 2003 campaign	55
4.4	Main observation parameters and ground data used in model simulation of the wheat ENVISAT and ERS-2 SAR data at the field 6 of Matera in the 2003 campaign	56
4.5	Main observation parameters and ground data used in model simulation of the corn ENVISAT and ERS-2 SAR data at Loamy in the 2003 campaign	58
4.6	Main observation parameters and ground data used in model simulation of the wheat ENVISAT and ERS-2 SAR data at Loamy in the 2003 campaign	59
4.7	RMS errors (dB) in comparisons between simulated and experimental σ^o 's for corn and wheat fields.	68
6.1	Main ground data collected in the deciduous site, * Respectively winter and summer Leaf Area Index (LAI) values. . .	113

List of Figures

2.1	Example of geometric structure adopted for a generic vegetated soil. (a) Agricultural sketch; (b) Forest sketch.	14
2.2	Scatter mechanism in the matrix doubling algorithm	17
2.3	Multiple reflections among sublayers	19
3.1	Scatterer body and involved fields	24
3.2	Generic corn leaves shape	29
3.3	Geometrical and angular dimensions of the curved sheet	30
3.4	Backscattering coefficient of a canopy of corn leaves at L-band	33
3.5	Backscattering coefficient for a canopy at C-band for of: (a) corn leaves; (b) wheat leaves.	34
3.6	Backscattering coefficient for a canopy at X-band for of: (a) corn leaves; (b) wheat leaves.	35
3.7	Extinction efficiency of corn leaves: (a) C-band; (b) X-band.	36
3.8	Cross section of a hollow cylinder with inner radius a_{int} and outer radius a_{ext}	38
3.9	Trend of internal and external radii for a whole wheat growth cycle	41
3.10	Backscattering (a) and forward scattering cross section coefficients (b) at L-band (1.2 GHz)	42
3.11	Backscattering (a) and forward scattering cross section coefficients (b) at C-band (5 GHz)	43
3.12	Backscattering (a) and forward scattering cross section coefficients (b) at X-band (10 GHz)	44
3.13	Attenuation trends at L-band (1.2 GHz): (a) incident angle $\theta_i = 25^\circ$; (b) incident angle $\theta_i = 45^\circ$	45
3.14	Attenuation trends at C-band (5 GHz) (a) incident angle $\theta_i = 25^\circ$; (b) incident angle $\theta_i = 45^\circ$	46

3.15	Attenuation trends at X-band (10 GHz) (a) incident angle $\theta_i = 25^\circ$; (b) incident angle $\theta_i = 45^\circ$	47
4.1	Fresh biomass measured on the fields: (a) 2 corn fields: Central Plain (Dots), Loamy (Diamonds) (b) 4 wheat fields: Matera 2001 campaign (Triangles), Field 5 at Matera 2003 campaign (Diamonds), Field 6 at Matera 2003 (Stars), Loamy (Squares)	50
4.2	Comparison between corn Central Plain multitemporal σ^o 's and values simulated using disc and sheet models, at C-band and incident angle $\theta_i = 30^\circ$. (a) VV polarization; (b) HH polarization. Triangles: experimental data. Continuous line: disc model. Dashed line: sheet model.	61
4.3	Comparison between corn Central Plain multitemporal σ^o 's and values simulated using disc and sheet models, at C-band and incident angle $\theta_i = 30^\circ$, at HV polarization. Triangles: experimental data, continuous line: disc model and dashed line: sheet model.	62
4.4	Comparison between maize multitemporal σ^o 's at Loamy site and values simulated using disc and sheet models. C-band, VV polarization - notice that backscatter values at different incidence angles are included (see Table 4.5). Triangles: experimental data. Continuous line: disc model. Dashed line: sheet model	63
4.5	Comparison between multitemporal σ^o 's measured over a wheat field at Matera in 2001 at C-band, VV polarization. (a) SAR data (Triangles) and values simulated using full (continuous line) and hollow cylinder (dashed line) models. (b) Total backscattering (solid line), volume backscattering (dashed line), double bounce effect (dotted line), soil backscattering (dot-dashed line).	65
4.6	Comparison between multitemporal σ^o 's measured over wheat fields at Matera in 2003 (Triangles) and values simulated using full (Continuous line) and hollow cylinder (Dashed line) models. C-band, VV polarization. (a) Field 5; (b) Field 6. . .	66

4.7	Comparison between σ_{VV}^o 's at C-band measured by ENVISAT ASAR on the wheat field at Loamy and model simulations. (a) Triangles: experimental data. Continuous line: model simulations; (b) Total backscattering (solid line), volume backscattering (dashed line), Double bounce effect (dotted line), soil backscattering (dot-dashed line).	67
5.1	Sketch of forest model representation	71
5.2	Sketch of litter model representation	72
5.3	Simulated reflectivity of soil/litter as a function of litter biomass. Volumetric soil moisture = 20%; (a): Vertical polarization; (b) Horizontal polarization.	74
5.4	Real parts (a) and imaginary parts (b) of the dielectric constants, as a function of soil moisture: soil (ε_{rs}), dielectric material (ε_{rd}), litter mixture (ε_{rl}) and equivalent half-space (ε_{re})	76
5.5	Total biomass for several kind of Softwood and Hardwood species	78
5.6	Component biomass percentages for Hardwood and Softwood species	79
5.7	Distribution function for three coniferous species	80
5.8	Relation between <i>LAI</i> values and dry leaves for Hardwood and Softwood species	81
5.9	Dry biomass components as a function of <i>LAI</i> for Douglas-fir and Pine forests	83
5.10	Douglas - fir and Pine numbers of trees per hectar, for different values of <i>LAI</i>	83
5.11	Trunks seight versus <i>Dbh</i> values	85
5.12	Diameter Branches distribution for Pine and Douglas-fir	86
5.13	Emissivity vs observation angle for a SMC=10%; (a) : V polarization; (b) : H polarization.	88
5.14	Emissivity vs observation angle for a SMC=20%; (a) : V polarization; (b) : H polarization.	89
5.15	Transmissivity vs observation angle; (a) : V polarization; (b) : H polarization.	90
5.16	Emissivity vs SMC for $\theta = 25^\circ$; (a) : without litter; (b) : with litter.	92
5.17	Emissivity vs SMC for $\theta = 45^\circ$; (a) : without litter; (b) : with litter.	93

5.18	Emissivity vs observation angle for a SMC=10%; (a) : V polarization; (b) : H polarization.	94
5.19	Emissivity vs observation angle for a SMC=20%; (a) : V polarization; (b) : H polarization.	95
5.20	Transmissivity vs observation angle; (a) : V polarization; (b) : H polarization.	96
5.21	Emissivity vs SMC for $\theta = 25^\circ$; (a) : without litter; (b) : with litter.	97
5.22	Emissivity vs SMC for $\theta = 45^\circ$; (a) : without litter; (b) : with litter.	98
6.1	Modeled (lines) and observed ($\pm 1.5 \sigma$ error bars) emissivity as a function of angle. L-band, V polarization. Understory-litter optical depths = 0, 0.1, 0.2. (a) 2 years; (b) 5 years. . .	101
6.2	Modeled (lines) and observed ($\pm 1.5 \sigma$ error bars) emissivity as a function of angle. L-band, V polarization. Understory-litter optical depths = 0, 0.1, 0.2. (a) 26 years; (b) 32 years. .	102
6.3	Multitemporal trends at Bray site. (a) Brightness temperature (measured, simulated including litter, simulated without litter) at 45° , H polarization; (b) Soil moisture, soil and canopy temperature.	105
6.4	Sketch of radiometer configuration: (a) Upward configuration; (b) Downward configuration.	106
6.5	Data ground collected during the experiment. From bottom to up, precipitation rate [mm/ha], environmental temperature $^\circ\text{C}$ and leaves fallen.	107
6.6	Comparison between simulated (continuous lines) and measured (dots) brightness temperatures vs. Day of Year, 40° (blue) and 60° (red): (a) V polarization; (b) H polarization.	108
6.7	Downward looking configuration with foil: (a) sketch of the configuration; (b) picture of the foil from the tower.	109
6.8	Data collected from both the radiometer configurations: (a) observation angle of 40° ; (b) observation angle of 60°	110
6.9	Comparison between simulated data and radiometric values collected during the campaign, over the sites specified in the Table 6.4	112